NORTHWESTERN UNIVERSITY

Nonequilibrium and Quantum Transport Phenomena in Mesoscopic Ferromagnet/Superconductor Heterostructures

A DISSERTATION
SUBMITTED TO THE GRADUATE SCHOOL
IN PARTIAL FULFILLMENT OF THE REQUIREMENTS
for the degree
DOCTOR OF PHILOSOPHY

Field of Physics

By

José Aumentado

EVANSTON, ILLINOIS

December 2000

ABSTRACT

Nonequilibrium and Quantum Transport Phenomena in Mesoscopic Ferromagnet/Superconductor Heterostructures

José Aumentado

Although the past twenty years have seen much progress in the understanding of mesoscopic electronic transport, many novel devices remain unexplored. In contrast to nonmagnetic, normal mesoscopic structures, our understanding of similarly scaled ferromagnetic devices is minimal. This is in part due to the experimental difficulties of analyzing transport in the presence of nonhomogeneous magnetic fields since ferromagnetic structures may support magnetic structure on length scales comparable to the submicron dimension of many proposed devices. Such difficulties must be eliminated when assembling devices in which such ferromagnetic elements may be important elements in more complicated heterostructures (*e.g.*, ferromagnet/normal, ferromagnet/superconductor, *etc.*). In this sense it is important to understand the electronic transport properties of the single submicron ferromagnetic elements that may comprise these more complicated heterostructures.

In this dissertation we examine the electronic transport properties of single submicron ferromagnets and demonstrate how macroscopic ferromagnetic transport issues translate to submicron dimension devices. Our measurements indicate that many of the considerations taken in understanding mesoscopic nonmagnetic normal metals (*e.g.*, quantum interference and probe switching symmetries) are also applicable to submicron ferromagnetic metals with additional complications due to the inherent magnetic structure. These complications manifest themselves through anisotropic contributions to the resistivity tensor which are a function of magnetization direction within a ferromagnetic structure and are much more pronounced when the dimensions of the element are reduced to the micrometer scale.

Finally, we apply this knowledge of single submicron ferromagnetic transport to investigate the possibility of a superconducting proximity effect in ferromagnet/superconductor heterostructures. It is found that such an effect is minimal in our systems yet the resistance of the interface between the ferromagnet and superconductor can display strong dependences on the temperature, magnetic field and energy bias. These results are discussed within the framework of the Blonder-Tinkham-Klapwijk model of transport in a normal/superconductor interface with modifications for the spin-polarized current of the ferromagnetic metal.

ACKNOWLEDGMENTS

There are, of course, about a billion people I can thank for their support, but years of experimental work have whittled away much of my capacity for memorizing details and circumstances not documented in a Physical Review Letter or some other auspicious journal. Nonetheless, a number of people and memories stand out which I'll never forget and will probably provide good fodder for future barroom ramblings.

First, there is my advisor, Prof. Venkat Chandrasekhar, who's done much to initiate me into the arcane world of mesoscopic physics, educated me in the fine art of electronic/thermal transport measurement and taught me that, when in doubt, the proverbial "It" is always trivial. Additionally, Chien-Jung Chien and Jonghwa Eom schooled me in the ways of the Mesolab back in the days when it was still largely being built. It was sort of fun, in a ridiculous way, to see all of us bleary-eyed at four in the morning doing science and talking about kung-fu movies with me hopped up on a sixer of Jolt$^{\mathrm{TM}}$ and the others on a pot of Sumatra from our rancid coffee maker.

In a similar manner, Jan Kycia and Tom Haard were also always available for the inevitable procrastination session and were incredible sources of even more incredible Tech horror stories. Both made working late fun, in those wee hours of questionable productivity, "experimenting" with liquid nitrogen and 60 Hz "noise guns".

Mike Black was a later addition to our lab and, for a physics post-doc, seemed to have a bottomless knowledge of the Spice Girls and was always ready to deliver an anecdote about nutty Norwegians or stomach-turning mishaps with hydrofluoric acid in esteemed British laboratories.

Recently, our lab has exploded (figuratively!) into a plethora of post-docs and students (I still remember when it was only Venkat, Mike and me), and all of our recent additions, graduate students Zhengfan Zhang and Zhigang Jiang and Drs. Dima Dikin, Sergey Rozhok and Sukkoo Jung have made the lab a much more exciting place to work in.

In terms of actual physics, I've been lucky to have Profs. Anupam Garg and John Ketterson to pester with my trivial (and sometimes not-so-trivial) questions, with both of them always demonstrating patience and sometimes even some answers. It was always inspiring seeing their enthusiasm for physics in general, and moreso their desire to communicate it.

It would be incredibly negligent of me to not acknowledge the Physics Department staff, especially Ves Brumfield, Chris Lopes and Marsha Coffey. Their bureaucratic acrobatics have gotten me out of many ridiculous situations and for that I'm grateful.

Outside of physics, I've had the fortune to have friends who forced me to take a break every once in a while. Aaron Shuman, Shannon Leonard and Jen Striegel have all been sources for nonphysics culture, support, Thanksgiving dinners, road trips and crass humor. Additionally, Eileen O'Brien has been a great housemate, friend and fellow Californian with whom to commiserate whenever the weather decided to wreak havoc on our mild weather sensibilities. Andrea Wells, while also being a good lab assistant, ended up being a good friend and gave me a place to write this thing when my lease ran out.

Lastly, I'd like to thank my parents, Alberto and Yolanda for being patient and supportive with their recalcitrant son, and my little brothers Albert and Dave, for reminding me to play more.

TABLE OF CONTENTS

LIST OF FIGURES

LIST OF TABLES

Chapter 1

INTRODUCTION

The field of mesoscopic physics has matured a great deal since the earliest confirmation of electronic phase coherence at experimentally accessible length scales. In semiconductors, the phase coherence length l_φ may exceed many tens of microns at low temperatures while nonmagnetic normal metals generally show phase coherence at lengths of only a few microns to a few tens of microns at similar temperatures [1]. In this sense, in metallic structures it can be more difficult to look for signatures of phase coherent transport such as weak localization, conductance fluctuations, and Aharanov-Bohm oscillations since the necessary size regime is restricted to submicron structures. Despite these difficulties, the aforementioned effects are well-studied experimental realities [2] and the focus has shifted to nonequilibrium phenomena in recent years, necessitating the fabrication and measurement of relatively more complicated heterostructures.

While normal-superconductor (NS) heterostructures have been used to investigate the problem of nonequilibrium superconductivity, ferromagnetic heterostructures remain a largely unexplored topic. This is in part due to the lack of a consistent picture of ferromagnetic electronic transport at small scales. Additionally, although quantum transport has been verified at micron length scales in nonmagnetic normal metals, the same is not true for mesoscale ferromagnetic devices and is a motivating question for many mesoscopic experimentalists. Currently a number of groups around the world are beginning studies in submicron ferromagnet-superconductor (FS) structures, focusing on possible superconducting proximity effects on the ferromagnetic (F) side. Since such structures include F components of various geometries, it is a necessary first step to understand the constituent transport phenomena prior to understanding more complicated heterostructures.

1.1 Mesoscopic Ferromagnets?

1.1.1 Phase coherence and quantum interference

The primary length scale of interest in many mesoscopic devices is the phase coherence length l_φ. l_φ is the average distance an electron may diffuse before losing memory of its phase, and therefore provides a scale within which one may observe the wave nature of these electrons. As one may suspect, this wave nature manifests itself in "quantum interference" phenomena and may be seen unambiguously in experimental observables such as the resistance/conductance. Such phenomena (*e.g.*, weak localization (WL) [3] and conductance fluctuations (CF) [2,4]) are more easily observed when a sample's dimensions are reduced to those comparable to l_φ, and subsequently samples may be labeled "quasi-1D" or "quasi-2D." Conventionally, devices which are fabricated with any dimension smaller than l_φ are also labeled "mesoscopic." However, in practice the term has been used to describe any structure of submicron dimension, regardless of the electronic length scales involved. This is important because, for practical purposes, l_φ has never been experimentally determined in a ferromagnetic device. While weak localization has proved a reliable method of determining l_φ in nonmagnetic materials (*i.e.*, Au, Al, Ag, Cu, *etc.*), it is generally restricted to low applied magnetic fields ($<$ 1 kG). Therefore it is difficult to perform such standard measurements in common elemental ferromagnetic metals (Fe, Ni, Co), since the intrinsic magnetic field due to the magnetization may exceed many kilogauss. However, WL is not the only signature of phase coherence and, as we shall see, a more appropriate indication of quantum transport in ferromagnets may be the presence of CF. In any case, the current lack of experimental confirmation of an appreciable level of phase coherence in a ferromagnetic metal is a tantalizing aspect of any study of mesoscale ferromagnetic elements and one to which we will draw our attention in our own experiments.

1.1.2 Contributions to the magnetoresistance

In principle, it should be possible to establish the existence of phase coherent transport (such as CF and even WL) in ferromagnetic devices if l_φ is on the order of 10^2 nm[1] since conventional e-beam lithography techniques can define features $<$100

[1] In most of the commonly studied metals l_φ is only appreciably long (with respect to the device size) at temperatures below $\sim$10 K. For this thesis it will always be assumed that l_φ is discussed in the context of experimentally accessible low temperatures, *e.g.*, l_φ is "short" if it is smaller than what we can define with e-beam lithography, at a base temperature 20–300 mK.

nm in lateral dimension. However, unlike nonmagnetic metals, ferromagnetic metals bear two other contributions to the resistance— anisotropic magnetoresistance and the anomalous Hall effect. These two effects are bulk phenomena, yet manifest themselves in unique ways at the submicron scale and must be accounted for separately from the quantum transport effects.

It will be shown that each of the above contributions to the magnetoresistance may be separated and understood independently. Such considerations will eventually be important in defining what is meant when one discusses "mesoscopic ferromagnets" and will contribute to methods for engineering possible "spintronic" devices which may incorporate these elements.

1.2 Normal/Superconductor and ferromagnet/superconductor heterostructures

In the past five years interest in nonequilibrium phenomena has motivated the fabrication of novel mesoscopic heterostructures. NS devices have been measured by many groups in an effort to understand mesoscopic nonequilibrium superconductivity (*e.g.*, charge imbalance and the superconducting proximity effect). Recently, many workers have shifted their focus and have begun to study similar phenomena in FS heterostructures both experimentally [5–9] and theoretically [10–13].

There has been much debate about the origins of the effects seen by the few groups who have studied this problem so far [14], yet a common aspect of all of the published FS experiments to date is the utilization of device geometries which, while appropriate for NS devices, suffer from ill-characterized magnetization distributions due to the micromagnetic nature of the constituent ferromagnetic elements. Despite these complications, the results are intriguing. Strong temperature dependences in the resistance of the ferromagnetic elements seem to indicate that electron pair correlations may decay over a few hundred nanometers from the FS interface into the ferromagnet [6, 9], while theorists object to such a large length scale on the grounds that the presence of a strong exchange field should depair these correlations within a few nanometers [11].

1.3 Overview of this thesis

In Chapters 2 and 3, I outline the theoretical and experimental background necessary for both single ferromagnetic particle and NS/FS transport in order to establish a context for our experiments. Specifically, in Chapter 2, we examine the theoretical bases for the various resistance contributions relevant to mesoscale ferromagnetic metals as well as an overview of some of the recent transport experiments in this field. Chapter 3 gives an overview of the Blonder-Tinkham-Klapwijk model of NS transport, with the necessary extensions for FS structures, as well as a survey of recent FS experiments. Chapter 4 details the experimental techniques (fabrication and measurement) necessary to complete our studies. Chapters 5 and 6 describe our experiments in single ferromagnetic elements and FS heterostructures, respectively. Finally, Chapter 7 provides a summary of our results and conclusions.

Chapter 2

SINGLE FERROMAGNETIC PARTICLE TRANSPORT: EXPERIMENTAL BACKGROUND AND THEORY

2.1 Mesoscale ferromagnetic transport

In principle it is not difficult to deposit a ferromagnetic metal instead of a non-magnetic one, and so it is interesting to note that despite a fairly established literature in mesoscopic nonmagnetic experiments, there is no corresponding body of experiments in ferromagnetic metals. As mentioned previously, this lack of experiment in mesoscale ferromagnetic transport may be largely due to difficulties in interpretation. Besides well-known transport phenomena such as weak localization (WL) [3], conductance fluctuations (CF) [4, 15], electron-electron interactions (EEI) [16], Hall effect (HE) [17], Lorentz-type magnetoresistance (LMR) [18], which are seen in nonmagnetic metal samples, there are additional contributions such as an anisotropic magnetoresistance (AMR) [19] and an anomalous Hall effect (AHE) [18] which are specific to ferromagnetic metals. Complicating all of these effects is the presence of domain structure which may provide a very disordered local magnetic field distribution which is hysteretic and possibly nonreproducible.

Despite these difficulties there are a few experiments which attempt to tackle the question of quantum transport specifically while there are also a number of recent experiments which demonstrate the importance of AMR in analyzing micromagnetic distributions of mesoscale ferromagnets. In the discussion that follows, we shall examine some of these experiments as we consider the various contributions to the magnetoresistance (MR) as listed above.

2.1.1 Anisotropic magnetoresistance

In ferromagnetic metals it was found early on that the magnetization direction played an important role in the resistance. In fact, Thomson (a.k.a. Lord Kelvin) noted this phenomenon in 1857 [20], yet it would take almost a century for the problem to be tackled experimentally and theoretically [21]. In that and subsequent work (see Ref. [19] for a review) it was found that the resistivity could be broken up into three contributions: $\rho_{\|}$, $\rho_{\perp}$ and ρ_H, with the subscripts "$\|/\perp$" denoting the direction of the magnetization with respect to the current path and "H" the Hall contribution. This anisotropic behavior has proven to be a useful element in the data recording industry since it provides yet another electronic probe of the magnetization [19]. For this reason, AMR has been studied quite extensively over the past thirty years, often in thin film devices. However, the advent of more advanced lithographic techniques has opened up the possibility of smaller ferromagnetic electronic elements and the need to understand how AMR scales at ever-decreasing dimensions.

We begin by examining the AMR from the resistivity tensor. From symmetry arguments [22, 23] the resistivity tensor for a polycrystalline magnetic medium saturated in the $\hat{z}$ direction is of the form:

$$[\rho_{ij}] = \begin{bmatrix} \rho_{\perp}(B) & -\rho_H(B) & 0 \\ \rho_H(B) & \rho_{\perp}(B) & 0 \\ 0 & 0 & \rho_{\|}(B) \end{bmatrix}. \tag{2.1}$$

In terms of the electric field $\boldsymbol{E}$, the current density $\boldsymbol{j}$ and the magnetization direction unit vector $\boldsymbol{\alpha}$, we can rewrite Eqn. 2.1 as [18],

$$\boldsymbol{E} = \rho_{\perp}\boldsymbol{j} + [\rho_{\|} - \rho_{\perp}][\boldsymbol{\alpha}\cdot\boldsymbol{j}]\boldsymbol{\alpha} + \rho_H\boldsymbol{\alpha}\times\boldsymbol{j}. \tag{2.2}$$

The resistivity can be expressed as $\rho = \boldsymbol{E}\cdot\boldsymbol{j}/j^2$, which can be used to reduce Eqn. 2.2 to a simple relation between the resistivity ρ and the relative angle θ between the magnetization and the current,

$$\rho(\theta) = \rho_{\perp} + \Delta\rho_{AMR}\cos^2\theta, \tag{2.3}$$

where $\Delta\rho_{AMR} \equiv \rho_{\|} - \rho_{\perp}$. Since AMR is a microscopic effect, it should be realized (especially in mesoscale devices) that the resistivity has a local anisotropic character, *i.e.*, $\rho(\theta(\boldsymbol{x}))$. The result of this consideration is that all resistance measurements are really integrations along current paths and must include the magnetization distribution through a term $\propto \cos^2\theta(\boldsymbol{x})$ or more explicitly,

$$\rho(\boldsymbol{x}) \propto \left(\frac{\boldsymbol{j}(\boldsymbol{x})\cdot\boldsymbol{M}(\boldsymbol{x})}{|\boldsymbol{j}||\boldsymbol{M}|}\right)^2. \tag{2.4}$$

In this sense, the AMR effect becomes a useful tool for analysis if the magnetization of a device is very uniform. Likewise, it becomes an unwieldy quantitative tool

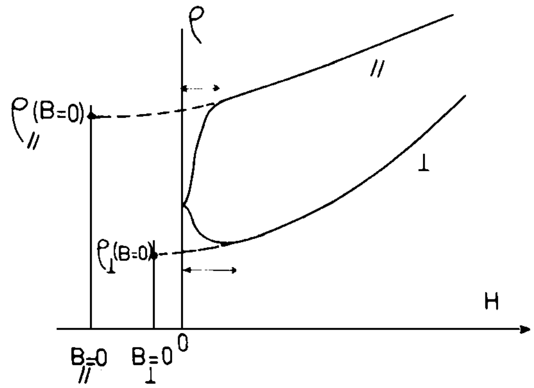

Figure 2.1: Schematic view of AMR effect in magnetoresistance with extrapolation to $B = 0$ values. *(Figure taken from Ref. [18])*

when a magnetization distribution has broken up into domains since the resistance will only be a spatial average if the voltage probe spacing is larger than the domain size.

It is important to note that the values for $\rho_{\|,\perp}$ are extrapolated to their zero-magnetic induction values. This is done to subtract out other magnetoresistance contributions, yielding values intrinsic to the magnetization direction and not the magnitude of the total internal field. Even at zero applied magnetic field, there exists an internal field due to the magnetic dipole moments ($4\pi\boldsymbol{M}$) as well as a "demagnetization" field ($-4\pi D\boldsymbol{M}$) which is dictated by the magnetostatics (read: geometry) of the specimen [24]. The relationship between the magnetic induction and the various field contributions is compactly expressed:

$$\boldsymbol{B} = \boldsymbol{H}_{app} + 4\pi(1 - D)\boldsymbol{M}. \tag{2.5}$$

To see how this extrapolation procedure is performed it is useful to first examine how the AMR manifests itself in MR measurements. Figure 2.1 illustrates the magnetoresistivity for magnetization both parallel ($\|$, top trace) and perpendicular ($\perp$, bottom trace) to the current path. In this example we assume that in zero applied field the magnetization breaks into many domains and that the net magnetic moment is zero. With this assumption, both the parallel and perpendicular resistance traces begin at the same value. An initial state such as this is usually termed the "demagnetized" state. Averaging Eqn. 2.3 over all relative angles [19] yields the value of this resistance to be,

$$\overline{\rho} = \frac{\rho_{\|} + 2\rho_{\perp}}{3}. \tag{2.6}$$

As the applied field is increased, the magnet is saturated and the curvature stabilizes into a Lorentz-type MR. It is this field dependence that is extrapolated to $B = 0$, ignoring the low-field curvature which is due to gradual alignment of domains, and accounting for the additional internal magnetic field due to the magnetization as noted above. With the values $\rho_{\|}$ and $\rho_{\perp}$, one may then define the AMR ratio,

$$\Gamma_{AMR} \equiv \frac{\Delta\rho_{AMR}}{\overline{\rho}}. \tag{2.7}$$

For transition metal ferromagnets this ratio is typically <5 %, but can be as large as 20–30% in particular transition metal alloys [18, 19]. This ratio is usually positive ($\rho_{\|} > \rho_{\perp}$) although exceptions have been noted in domain wall (DW) scattering experiments in epitaxial Fe films on GaAs [25–28] below ∼65 K, which may be more a function of competing temperature dependent scattering mechanisms in such high quality samples.

Now that we have a phenomenological picture of the AMR effect, we briefly review the microscopic nature of the anisotropy. As pointed out by Mott and Wills [29] in 1936, the current in $3d$ metals is mostly carried by s electrons since the d electron effective mass m_d^* is large. Since the density of d states $N_d(\epsilon_F)$ is much larger than that of the s states, the dominant contribution to the resistance is $s \to d$ interband scattering. Originally this model was used to explain the increase in resistivity as a transition metal was cooled through its Curie temperature, as ferromagnetic ordering exchange splits $N_d(\epsilon_F)$ into separate spin states, effectively decreasing the available majority spin states to zero.

Having established that sd scattering is the dominant contribution to the resistance, we must now ask where the anisotropy arises. The Mott picture assumes isotropic bands and, thus, isotropic scattering. The generally accepted picture [19, 21] singles out the spin-orbit interaction between electrons and lattice atoms as the source of the anisotropy. This was first proposed by Smit [21] who treated the spin-orbit interaction, $H_{so} = \lambda L \cdot S$, as a perturbation and calculated the d wavefunctions assuming cubic-symmetric unperturbed wavefunctions, ψ_d^0.

Recognizing that the spin-orbit interaction term decomposes into $L_{\pm}S_{\mp}$ contributions (which have the effect of mixing opposite spin states), Smit found that the resulting ψ_d^1 indeed exhibited a lower than cubic symmetry.[1] In short, the effect of the spin-orbit interaction was to contribute an anisotropy to the *sd* scattering mechanism. Smit's calculations also show that the probability of *sd* scattering in the direction of $\boldsymbol{M}$ is increased, resulting in $\rho_{\|} > \rho_{\perp}$ and $\Gamma_{AMR} > 0$ — a result confirmed by most experimental evidence [18, 19], with some exceptions as noted above [25–28].

Corrections in reduced geometries

While the mechanism behind AMR can explain the anisotropic resistive response to the magnetization direction, the situation poses additional complications when the dimensions of the sample become comparable to the elastic mean free path since collisions with the boundaries then become more probable for conduction electrons. Starting from the Boltzmann equation, one usually assumes an isotropic distribution of electron velocities in the bulk. This distribution is considerably modified near surfaces, and this is reflected in a general increase of the resistivity over the bulk value in thin films. This correction to the conductivity was first pointed out by Fuchs [30] and Sondheimer [31] in nonmagnetic thin films over fifty years ago, showing a monotonic increase in the resistivity over the bulk value as the film thickness was decreased. Rijks *et al.* [32] were the first to recognize the importance of these effects in ferromagnetic thin-film and wire geometries by introducing an anisotropic elastic mean free path $l(\theta)$, showing that the AMR ratio in thin films is actually divided into two distinct values which are correlated to magnetizations directed perpendicular to the current path but in the sample plane [perpendicular-in-plane (PIP)], and magnetizations directed perpendicular to the current path but normal to the sample plane [perpendicular-out-of-plane (POP)]. Rijks *et al.* [33] later confirmed these predictions experimentally, showing a reduction in the PIP AMR ratios as the dimensions were decreased [33].

The splitting of the in-plane and out-of-plane resistivities can be incorporated into the resistivity tensor ρ_{ij} (Eqn. 2.1), by allowing the ρ_{xx} and ρ_{yy} components to differ. Following the definition of the resistivity as before ($\rho = \boldsymbol{E} \cdot \boldsymbol{j}/j^2$), we

[1] Details of this calculation are beyond the scope of this thesis, but may be found in Ref. [19] and references therein.

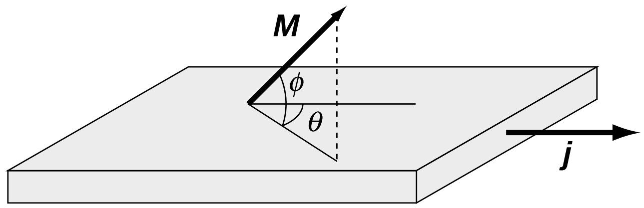

Figure 2.2: [Schematic representation of in-plane and out-of-plane angles for low-dimensional AMR corrections. θ is the angle of the magnetization relative to the current direction $\boldsymbol{j}$ in the sample plane. ϕ is the angle corresponding out-of-plane angle.

arrive at a relation to replace Eqn. 2.3,

$$\rho(\theta, \phi) = (\rho_{PIP} \cos^2 \phi + \rho_{POP} \sin^2 \phi) \sin^2 \theta + \rho_{\|} \cos^2 \theta, \tag{2.8}$$

with ρ_{PIP} and ρ_{POP} the resistivities with the magnetization pointed perpendicularly in-plane and out-of-plane, θ the relative angle (in-plane) between the magnetization and current direction and ϕ the angle of magnetic deviation from the plane (see Fig. 2.2).

2.1.2 Lorentz magnetoresistance

Another "classical" contribution to consider when analyzing the electronic magnetotransport is the Lorentz magnetoresistance (LMR), *i.e.*, the resistance due to trajectories curved by the Lorentz force on individual electrons. For our purposes, we will simply estimate the order of magnitude and field dependence. The magnetoresistance from this mechanism should arise in a change in the electron elastic mean free path, l, as the magnetic field is applied, increasing the length of an electron's arc-like trajectory between scattering centers. For a cyclotron orbit of radius r_L, the difference between the arc length and its corresponding chord can be written as

$$\Delta l = r_L \varphi - 2 r_L sin \frac{\varphi}{2} \tag{2.9}$$

or,

$$\Delta l \approx \frac{1}{3} r_L (\frac{\varphi}{2})^3 \tag{2.10}$$

if one assumes small fields, restricting the difference to small angles. Since this mechanism is only appreciable for arclengths on the order of l we can approximate $r_L\varphi \sim l$, giving $\Delta l \propto l^3/R_l$. For small Δl, the correction to the resistance is then,

$$\frac{\Delta\rho}{\rho} \propto \left(\frac{l}{r_L}\right)^2 \tag{2.11}$$

and finally,

$$\begin{aligned} \frac{\Delta\rho}{\rho} &\propto (\omega_c\tau)^2 \\ &\propto B^2, \end{aligned} \tag{2.12}$$

recognizing that the Larmor radius $r_L = v/\omega_c$ and that the Larmor frequency $\omega_c = eB/m^*c$. We must remember, though, that this result was derived under the assumption of isotropic bulk scattering, and is subject to Fuchs-Sondheimer effects when the dimensions are reduced as noted above. This "galvanomagnetomorphic" effect [34] may then have the opposite effect of reducing the B^2 dependence. In practice, an almost linear dependence is found in most thin film magnetoresistances above saturation [19, 21, 25–28, 35].

2.1.3 Quantum transport: weak localization and conductance fluctuations

Prior to discussing the mechanisms of quantum interference, we should pause to reflect how it is possible to observe the wave nature at all in what should be a nominally macroscopic quantity (*i.e.*, the resistance). Ultimately this reduces to the question of how a conduction electron can retain memory of its phase over micron length scales.

We know from experience that the mean free path in the metallic thin films deposited in our lab is only of the order of a few tens of nanometers and so it is surprising that an electron can diffuse over much longer lengths, scattering many times before its phase is completely uncorrelated to its starting phase. The key to understanding this is the realization that these *elastic* scattering events do not randomize the phase and, thus, do not decohere a diffusing electron. Rather, decoherence occurs either through inelastic scattering processes (*e.g.*, electron-phonon and electron-electron) or scattering with isolated fluctuating magnetic moments (spin-scattering). The electron-phonon and electron-electron scattering lengths may exceed many tens (or hundreds) of microns at low temperatures [36] and, for this reason, most mesoscopic quantum transport experiments are performed at $T < 10$ K. To eliminate the spin-scattering contribution, experimentalists are careful to minimize the magnetic impurities present in their metal deposition systems. When these conditions are observed, the phase coherence length l_φ may exceed many tens of microns [37].

Having noted the sensitivity of l_φ to spin-scattering via magnetic impurities, it is natural to wonder whether this precludes the possibility of a similarly long l_φ in ferromagnetic materials. To answer this it is necessary to realize that spin-scattering processes randomize the electron phase when the magnetic impurity itself experiences time dependent fluctuations in its magnetic moment [38]. Additionally, if enough magnetic impurities are present and a system is cold enough, a spin glass state may be created, giving a highly inhomogeneous magnetic field distribution which would suppress weak localization corrections to the conductivity. However, ferromagnets are, by nature, assemblies of long-range correlated magnetic moments and paramagnetic fluctuations are almost completely suppressed at low temperatures. Inhomogeneous field distributions may still be present in the form of domain structure; however, this can be eliminated by saturation in a strong magnetic field or by careful micromagnetic design. In principle, the decoherence issues raised by magnetic impurities in nonmagnetic normal metals are mostly irrelevant in ferromagnetic metals since fluctuations are likely to be suppressed by the long range magnetic order. It is curious, then, that there has been no definitive confirmation of mesoscale phase coherence in ferromagnetic metals. In what follows, we will discuss the basics of two particular phase coherent (or quantum transport) phenomena as well as the few relevant experiments in ferromagnetic metals.

Weak localization

The theory of weak localization (WL) was developed in the late seventies using a diagrammatic perturbation theory [39, 40]. In essence, it predicts a correction to the usual Boltzmann conductance ($\sigma_0 = ne^2\tau/m$) of order e^2/h which is due solely to the wave nature of the electron wavefunction. These corrections were originally considered negligible since they were of order $1/k_F l$ in the perturbation series which described the conductivity [41]. An intuitive physical picture was later suggested by Bergmann [42] who pointed out that WL could be understood as a coherent backscattering mechanism which enhances the probability of remaining (or being "localized") at the origin. Quantum mechanically this can be understood in the Feynman path integral formalism [43]. We know that the probability of propagating from $\boldsymbol{r}$ to $\boldsymbol{r}'$ over a time t can be expressed as

$$\begin{aligned} P(\boldsymbol{r}, \boldsymbol{r}', t) &= |\sum_i A_i|^2 \\ &= \sum_i |A_i|^2 + \sum_{i \neq j} A_i^* A_j \end{aligned} \tag{2.13}$$

where the A_i are probability amplitudes for all possible trajectories between $\boldsymbol{r}$ and $\boldsymbol{r}'$ (see Figure 2.3(a)). The first term describes the classical diffusion probability, summing the probabilities of all trajectories separately, while the second term contains the interference terms between trajectories since the phase is not conjugated out. If we allow $\boldsymbol{r}' \rightarrow \boldsymbol{r}$, $P(\boldsymbol{r}, \boldsymbol{r}, t)$ will describe all closed loop trajectories (*i.e.*, all backscattering paths; see Figure 2.3(b)). Since each of these loops can be decomposed into clockwise and counterclockwise trajectories one can define $A_{cw} = \sum_i A_{i,cw}$ and $A_{ccw} = \sum_i A_{i,ccw}$. In the absence of a magnetic field these two contributions are essentially time reversed versions of each other and $A_{cw} = A_{ccw}$. If we rewrite Eqn. 2.13 for these closed loop trajectories we have

$$\begin{aligned} P(\boldsymbol{r}, \boldsymbol{r}, t) &= |A_{cw} + A_{ccw}|^2 \\ &= 4|A_{cw}|^2. \end{aligned} \tag{2.14}$$

This is exactly twice the classical return probability. One can return to Eqn. 2.13 and see that this can only be accounted for if the interference terms $A_i^* A_j$ are constructive— a direct consequence of the time-reversal symmetry of the clockwise and counterclockwise paths. It is this enhanced probability for return that provides the localization and this, in turn, enhances the resistance. The time-reversal symmetry itself may be broken by application of a small magnetic field and, indeed, this effect can be seen in a reduction of the resistance. This is only the case for metals where the spin-orbit scattering is weak. In metals such as Au, the spin-orbit scattering is strong and the characteristic localization peak in the magnetoresistance is replaced by a dip, and the effect is often called "anti-localization." This is beyond the scope of this thesis, but an excellent review of the theoretical and experimental work appears in Ref. [42].

Additional notes on the observability of weak localization in ferromagnets

Since small fields seem to suppress WL in the nonmagnetic metal devices most experimentalists are familiar with, it seems obvious that ferromagnetic metals would

(a)

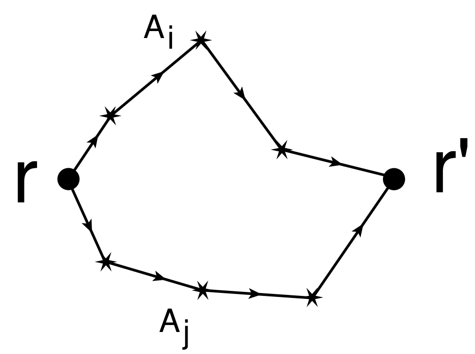

(b)

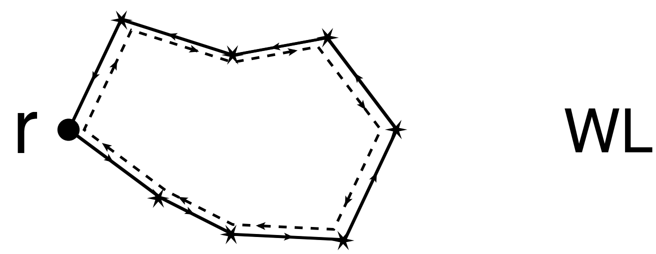

Figure 2.3: Physical picture of the weak localization/coherent backscattering mechanism. (a) Trajectories between $\boldsymbol{r}$ and $\boldsymbol{r}'$. (b) Closed loop trajectories ($\boldsymbol{r}' \rightarrow \boldsymbol{r}$) responsible for coherent backscattering.

make poor specimens for WL studies due to the large internal fields present (*e.g.*, for Ni, $4\pi M$ ~6.3 kG). We can explore this issue further by examining the critical field $B_{c,WL}$ beyond which WL is suppressed. $B_{c,WL}$ can be estimated by determining the field necessary to shift the phase by 2π along a maximal phase coherent loop area A_φ, *i.e.*,

$$B_{c,WL} \sim \frac{\Phi_0}{A_\varphi}, \tag{2.15}$$

where $\Phi_0 = hc/2e$ (=20.7 Gμm^2 in practical units), the superconducting flux quantum. This area takes on different forms depending on whether the dimensions are less than l_φ or not. In one dimensional samples (*i.e.*, with width and thickness less than l_φ), with micron scale l_φ, the critical field is typically less than a few hundred Gauss, much less than typical ferromagnet internal fields. However, $B_{c,WL}$ can be raised considerably by reducing the perpendicular area exposed to the magnetic field as would be done if the field were directed lengthwise along a narrow wire sample. If the width and thickness are less than the phase coherence length ($w, t < l_\varphi$), then the relevant $A_\varphi = wt$. With typical dimensions, w =100 nm and t =30 nm this yields $B_{c,WL}$ = 6.9 kG, which is slightly greater than the internal magnetic field in Ni! For this reason, a longitudinal MR measurement may provide a feasible method of observing a ferromagnetic WL effect as long as these size restrictions are considered. Since the main obstacle in the problem is nonuniform magnetization at small fields, another much simpler method may be to simply saturate the magnetization along an easy axis, and apply small fields perpendicular to this axis. This has its own complications however, since the magnetization will rotate somewhat with the vector sum of the applied fields and again AMR must be considered.

Conductance fluctuations

Besides WL, there is an additional correction to the conductance which is also due to quantum interference of electron wavefunctions. Perhaps the easiest way to visualize this contribution is to extend the wave analogy to standing waves in a shallow pool filled with a number of obtrusions. The obtrusion distribution drives the formation of a complicated standing wave interference pattern which can be drastically altered by even minute obtrusion rearrangements. In a metallic sample, this would correspond to a change in the conductance with a minute change in the impurity distribution. In metals, the impurity mobility may be thermally activated and one be able to rearrange the impurity distribution simply by heating the sample. Repeating this many times, one would find the conductance to fluctuate by $\sim e^2/h$ about the average. In practice, temperature cycling can be tedious, and the conductance fluctuations (CF) may be observed in a more dramatic way by ramping a magnetic field. The magnetic field has the effect of shifting the phase of the electron trajectories, but since there are many scatterers and many trajectories, the phase shifts at any point in a sample are never uniform with respect to the magnetic field. Alternatively, one can forego the pool analogy entirely and examine the interference term from Eqn. 2.13 directly. Since we are interested in the rms conductance fluctuation magnitude δG, we can alternately examine the variance of the diffusion probability from $\boldsymbol{r}$ to $\boldsymbol{r}'$, $P(\boldsymbol{r}, \boldsymbol{r}', t)$ (Eqn. 2.13), or more specifically its interference term $\sum_{i \neq j} A_i^* A_j$. In general, each amplitude A_i will have an associated phase $\phi_i \propto \int \boldsymbol{A} \cdot dl_i$ where $\boldsymbol{A}$ is the vector potential incorporating the magnetic field dependence. The interference term will then be $\propto \cos \Delta\phi_{ij}$ (where $\Delta\phi_{ij} \equiv \phi_i - \phi j$). The variance will then have $<\cos \Delta\phi_{ij}>^2$ terms which average to zero over the phase, while $<\cos^2 \Delta\phi_{ij}>= 1/2$. It is this nonzero variance that manifests itself in CF in the magnetic field dependence (see Fig. 2.4). These CF are reproducible in subsequent field sweeps as long as the sample has not been warmed and the impurity configuration has not been shifted. However, because the path integrals which determine the phase are necessarily limited to trajectories $l_i < l_\varphi$, the CF magnitude is reduced for voltage probe separations much greater than l_φ [15].

Although WL is destroyed relatively easily by a magnetic field, CF can persist to very high fields since it is due to differences in phase rather than time-reversal symmetry. Because of this, it is a very good candidate for verifying mesoscale phase coherence in ferromagnetic metals. Just as in WL, it may be necessary to constrain the dimensions to less than l_φ and to apply the magnetic field longitudinally. We have performed these measurements in submicron Ni ellipses [35] and will present that work in Chapter 5 as additional tentative evidence for ferromagnetic quantum transport. Keeping this in mind we present the equations which follow for later use.

We characterize the CF by a correlation field $B_{c,CF}$ which describes the mean field spacing between fluctuations. Describing the correlation function for the normalized conductivity g,

$$F(\Delta E, \Delta B) =< g(E, B) g(E + \Delta E, B + \Delta B) > - < g(E, B) >^2, \tag{2.16}$$

we define $B_{c,CF}$ at the full width at half maximum, $F(B_{c,CF}) = F(0)/2$. This correlation field has a similar dependence on the area enclosed by a maximal phase

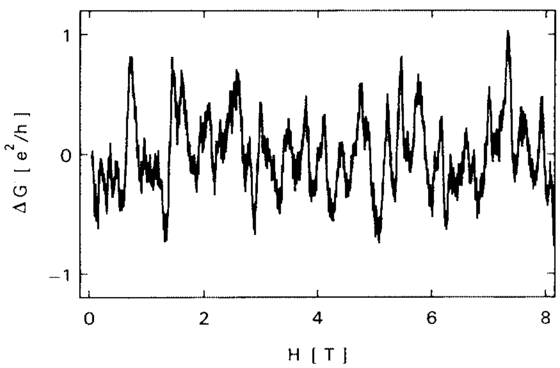

Figure 2.4: Typical magnetoconductance fluctuations in a 1D Au wire (310 nm long, 25 nm wide) at T =10 mK. *(Figure taken from Ref. [2])*

coherent area (Eqn. 2.15), with the exception that relevant enclosed flux is the single electron flux quantum $2\Phi_0$ since the condition of time reversal invariance has been relaxed and the mechanism relies on 2π phase shifts between trajectories connecting $\boldsymbol{r}'$ and $\boldsymbol{r}$.

Experimental evidence?

To date there has been no clear evidence for phase coherent transport in a ferromagnet at length scales comparable to those attainable by conventional e-beam lithography techniques and there are a precious few experiments which do attempt to attack this problem directly [44, 45]. Aprili *et al.* [45] attempt to fit the $\ln T$ temperature dependence of the conductance of very thin Ni films in the percolative regime to a WL theory, while Kobayashi *et al.* [46] attempt a similar fit in homogeneous Ni films. Since both the WL and electron-electron interactions (EEI) have a $\ln T$ dependence in 2D [3,16], it is possible that the low temperature dependence of the conductance is really due to EEI effects rather than WL. This is the most likely explanation since the internal magnetic field in bulk Ni should already suppress the WL contribution.

Hong and Giordano [44] take a different approach and assert that the strong magnetoresistance (MR) of long narrow Ni wires is a novel mesoscopic transport effect (electron-magnon scattering), reminiscent of weak localization but orders of

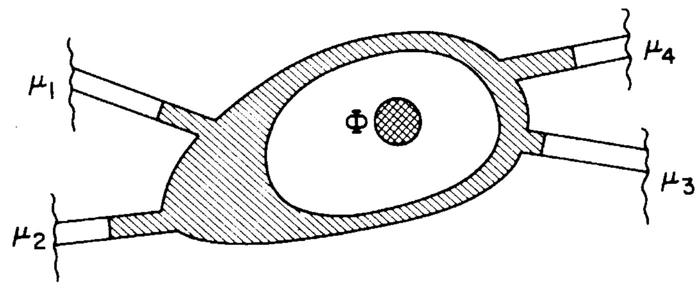

Figure 2.5: Disordered normal conductor connected to four reservoirs (μ_{1-4}) via perfect leads. A flux Φ is applied through the sample.

magnitude larger. However, this strong MR persisted at much higher temperatures, demonstrating that the effect had little to do with phase coherent transport. In fact, subsequent measurements by many groups [47–49] indicate that the MR seen in Ref. [44] may be due to the well-understood AMR mechanism, assuming that the magnetization distribution changes somewhat upon application of a field. This simple assumption is an important one which will be of use in our own single particle measurements (see Chapter 5) and has been utilized in measurements of arrays of ferromagnetic wires [49] as well as in sub-100 nm electrodeposited Ni wires [50, 51].

2.2 Electrical probe symmetries

In four terminal mesoscopic devices the measurement probes can be an integral part of a device contributing asymmetric components to the MR [52] and affecting the magnitude of the WL and CF contributions [53]. The asymmetric contributions are essentially Hall-type contributions which can arise since it is very difficult to sample only the diagonal components of the resistivity tensor when the probe widths are on the order of the sample size [52]— a situation which is particularly common in very short mesoscopic samples.

The question of whether quantum transport effects such as Aharonov-Bohm (AB) oscillations in rings and CF was of particular interest in mesoscopic physics and it was not until 1988 that Büttiker outlined the basic reciprocity relations for

4-terminal measurements in a magnetic field [54]. Starting from a simple Landauer-like picture of electronic transmission between reservoirs μ_{1-4} (see Figure 2.5), Büttiker derived a reciprocity relation between different probe configurations as a function of field,

$$R_{ij,kl}(H) = R_{kl,ij}(-H). \tag{2.17}$$

Here, the notation $R_{ij,kl}$ denotes a four-terminal resistance where i and j denote the I_+ and I_- current leads while k and l denote the V_+ and V_- leads.

Since we will be dealing with ferromagnetic devices we will primarily be interested in a further generalization of Eqn. 2.17 to conductors with a magnetization $\boldsymbol{M}$,

$$R_{ij,kl}(H, M) = R_{kl,ij}(-H, -M). \tag{2.18}$$

These relations are completely general (in the linear response regime) and were found to be valid even for CF and AB oscillations in a dramatic experiment by Benoit *et al.* [52] in Au and Ag rings, stressing the validity of these symmetries in phase-coherent phenomena.

In practice, these reciprocity relations allow us to identify spurious Hall-type contributions in our single ferromagnetic particle measurements by simply switching probe current and voltage probes [35]. We will return to this point in Chapter 5.

2.3 Summary

As we can see, the sources for magnetic field dependence in the resistivity are numerous, and the above review can by no means encompass them all. Instead, it informs us of the need to be vigilant in our physical interpretation, especially when it comes to verifying quantum transport phenomena which have notoriously weak contributions with respect to less exotic mechanisms such as AMR. The importance of this cannot be stressed enough and many recent experiments in domain wall scattering in mesoscale devices [25–28, 55–59] may alternately be understood in terms of AMR contributions with modifications in the analysis of current and magnetization distributions at the submicron scale. As an example of these considerations we have worked out an alternate explanation for one of these experiments (Taniyama, *et al.* [58]) which is included as Appendix A.

Chapter 3

FERROMAGNETIC/SUPERCONDUCTOR TRANSPORT: EXPERIMENTAL BACKGROUND AND THEORY

When a nonmagnetic normal metal (N) is in good contact with a superconductor (S), the resulting resistivity in N can be greatly modified due to the "leakage" of Cooper pair correlations from S. This is most simply understood in the Ginsburg-Landau (GL) theory [60] as a finite amplitude of the order parameter in N which decays over a length scale ξ_N, the normal metal coherence length.[1] In terms of the microscopic theory, this leakage of pair correlations was first described by Andreev [62] as the ability of electrons with sub-gap energies to penetrate into S by generating a retroreflected hole of opposite momentum. In this manner, two electrons could be transmitted into S to form a Cooper pair. This process is termed Andreev reflection and is the basic mechanism behind the so-called "proximity effect."

The energy scale governing the extent of this effect in a diffusive metal is the simply the thermal energy k_BT through the normal (dirty) metal coherence length $\xi_{N,dirty} = l_T = (\hbar D/k_BT)^{\frac{1}{2}}$ [61]. Intuitively we understand the conduction electrons to be confined to a bandwidth $\sim k_BT$ of the Fermi energy, so this length would correspond to the maximum length over which an electron can diffuse while keeping its energy correlated to within this bandwidth. It turns out that this length can be on the order of a micron at low temperatures ($T < 1$ K), which makes the study of NS devices relevant to the mesoscopic regime.

In the past ten years, many groups have studied hybrid mesoscopic NS heterostructures and found a variety of surprising effects. Of these, the two most well-known are the reentrant proximity effect and Andreev interference. The reentrant proximity effect is named after the nonmonotonic temperature dependent behavior seen in the resistance of normal metal wires in contact with a superconductor. Such devices show a supression of the resistance as the temperature drops

[1]The GL interpretation of the proximity effect was first pointed out by de Gennes [61].

below the superconducting transition, but below a characteristic temperature this resistance begins to rise towards (or "re-enter") its normal state value [63]. The temperature at which the conductance maximum occurs is $5\varepsilon_c/k_B$ where ε_c is the "Thouless energy" or correlation energy $\hbar D/L^2$ for a sample of length L. Similar reentrance behavior is also seen in the differential resistance at similar energies, although Joule heating at the necessary current bias sometimes makes these measurements difficult to interpret. Coexisting with the reentrance is a coupling of the phase of the N electrons to the macroscopic superconducting phase, through the Andreev reflection process. This phase sensitivity has been observed in a variety of NS loop structures (or so-called Andreev interferometers) [63–67] which show oscillations as a function of applied magnetic field.

We could continue to discuss the enormous body of work that has been done in studying proximity NS devices, but for this thesis we are more concerned with the possibility of a similar proximity effect in ferromagnet/superconductor (FS) devices. Recently, Petrashov *et al.* [6] have reported "giant mutual" proximity effects in Al/Ni structures, while Giroud *et al.* [9] observed reentrance in the resistance of a Al/Co system. Measurements by Lawrence and Giordano [8] in (In/Pb)/Ni systems also showed a large temperature and field dependence. All of these observations run counter to expectations of a very short length scale based on the decoherence of the pair correlations by the strong exchange field present[2] in ferromagnetic metals (estimates for this length range from ∼2 nm in Co to ∼20 nm in Ni). Petrashov *et al.* estimate a proximity effect extending a length of almost a micron into their Ni structures [6] while Giroud *et al.* estimate a length scale of ∼200 nm [9]. The discrepancy with the theory is currently unresolved, although a recent publication by Belzig *et al.* [11] suggest that the effects seen in the Petrashov and Giroud experiments can be explained by spin-accumulation at the FS interfaces without invoking any proximity effect. With the exception of the Giroud experiment,[3] all of the measurements mentioned above included the FS interface

[2] Although this expectation is usually glossed over, it is not necessarily obvious that the relevant field is the internal field $B_{int} = (1-D)4\pi M$. A general way to consider the problem is to notice that the spin-splitting of the electron populations as they are transported from the superconductor to the ferromagnet must increase (and decrease) the spin-up (spin-down) electron energies by the exchange energy, *i.e.* the exchange field [68]. One can then define an energy correlation length $l_{ex} = (\hbar D/\varepsilon_{ex})^{\frac{1}{2}}$ over which electrons will diverge in energies; this splitting of spin-up/down electron energies has the effect of destroying superconducting correlations, hence its relevance for a proximity effect in ferromagnetic metals.

[3] The Giroud experiment [9] measured the resistance of a 50 nm thick Co ring with a 100 nm

in series. This aspect will be central to the interpretation of our own experiments (Chapter 6) and for this reason we will focus on the transport properties of NS and FS interfaces in this chapter.

3.1 The Blonder-Tinkham-Klapwijk model for normal/superconductor transport

Blonder, Tinkham and Klapwijk (BTK) [69] treated the one dimensional problem of transport at a NS point contact by solving the Bogoliubov-de Gennes equations [61] connecting quasiparticle currents between the N and S metals. While their method allowed one to calculate many transport dependences in a straightforward manner, it also cast the problem in an intuitive form which accounted for Andreev reflection processes which enhance the NS interface conductance. In what follows, we shall only outline the general results, developing a qualitative feel for the theory of NS transport which we can translate to the FS case.

In the BTK theory the NS barrier is characterized by a delta function potential $V(x) = H\delta(x)$, with the barrier height usually referred to by its dimensionless form $Z = H/\hbar v_F$. Following a quasiparticle description for the charge carriers, BTK derived transmission and reflection coefficients for all possible charge transfer processes at this interface for energies both above and below the gap. These processes are pictured schematically in Figure 3.1 and the resulting coefficients are listed in Table 3.1.

The processes shown in Fig. 3.1 give the probabilities of Andreev reflection (A), normal reflection (B) and transmission as a quasiparticle with and without branch crossing (C,D).[4] Physically, we can break up the transport into energies above and below the gap energy Δ and examine the transmission properties as a function of the barrier height. Figure 3.2 shows a plot of the coefficients, A and B

---

thick Al strip across one (or both) of the probes leading to the ring. While they found a strong temperature dependence in the FS junction by itself, a measurement of the ring showed reentrant behavior similar to the NS case. Unlike the Petrashov experiment [6], the FS interface is included in parallel in that (Giroud) measurement.

[4] The "branch crossing" referred to in the text (and in the original BTK paper [69]) corresponds to the four-fold degeneracy in possible momenta for quasiparticle energies $E_k > \Delta$. However, when transmitting into a quasiparticle state (from N to S), the quasiparticle group velocity dE_k/dk should remain directed into S, *i.e.*, positive. The only two points which correspond with such a principle are C and D as shown in Fig. 3.1.

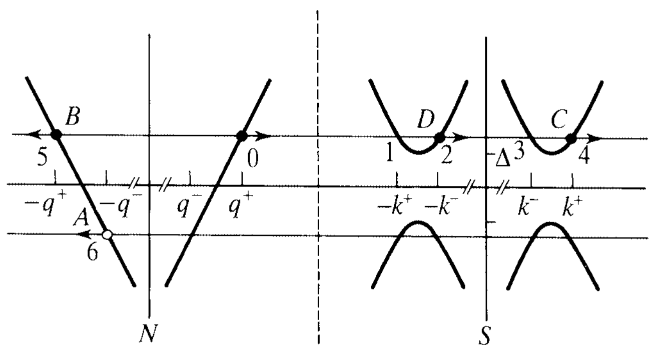

Figure 3.1: Charge transfer processes considered in the Blonder-Tinkham-Klapwijk model for NS transport. The schematic shows the energy vs. momentum plots on both sides of the NS interface. A normal electron incident at (0) will have four possible interactions with the interface. It may be (A) Andreev reflected as a hole (with branch crossing) (transmitted), (B) reflected, (C) transmitted without branch crossing and (D) transmitted with branch crossing. *(Figure taken from Ref. [70].)*

BTK coefficients	A	B	C	D
Normal state	0	$\frac{Z^2}{1+Z^2}$	$\frac{1}{1+Z^2}$	0
General form				
$E < \Delta$	$\frac{\Delta^2}{E^2+(\Delta^2-E^2)(1+2Z^2)^2}$	1-A	0	0
$E > \Delta$	$\frac{1}{4\gamma^2}\left(1-\frac{1}{N_s^2}\right)$	$\frac{Z^2(1+Z^2)}{N_s^2\gamma^2}$	$\left(\frac{N_s+1}{N_s^2}\right)\left(\frac{1+Z^2}{2\gamma^2}\right)$	$\left(\frac{N_s-1}{N_s^2}\right)\left(\frac{Z^2}{2\gamma^2}\right)$

Table 3.1: BTK transport coefficients. The coefficients A–D correspond to the probabilities of the processes shown schematically in Fig. 3.1. In the original BTK paper [69] these coefficients were expressed in terms of the BCS coherence factors, u_0 and v_0, which gives a slightly more compact form. Here we prefer to express the coefficients in terms of the quasiparticle density of states N_s, the superconducting gap energy Δ and the dimensionless barrier height Z since these can be incorporated into our numerical simulations in a more transparent manner. ($\gamma^2 = (N_s + 1 + 2Z^2)^2/4N_s^2$.)

as a function of energy (normalized to the gap energy).[5] When there is a perfect interface ($Z = 0$), the current has a unit probability of transmitting from N to S at $E < \Delta$. However, this mode of transmission is quickly attenuated at $E > \Delta$ as the probability of transmission as a quasiparticle (without branch crossing) begins to increase with the energy. As the barrier is raised slightly ($Z = 0.3$), a fraction of the electrons incident on S begin to be normally reflected. Intuitively, this reflected fraction B gets larger as the barrier is raised, until $Z\rightarrow\infty$ (the tunnel limit) and 100% of the incident electrons are reflected. In this limit, A then approaches a delta function-like behavior in E, reflecting the underlying quasiparticle density of states.

3.1.1 The BTK differential conductance

From the BTK coefficients we can now calculate the total transmission coefficients, giving an expression for the current. BTK did this, yielding the expression for the

[5] For clarity we restrict the schematic to the coefficients A and B since current conservation demands $A + B + C + D = 1$ and we are not necessarily concerned with the specifics of the transmitted probabilities C and D at the moment.

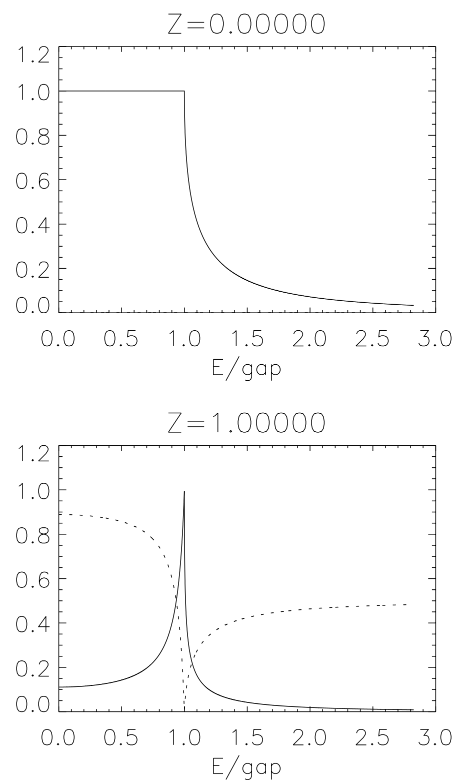

Figure 3.2: Numerical calculations (by the author) of the energy dependence of the BTK coefficients A (solid) and B (dashed).

total current through the NS interface under an applied voltage V,

$$I_{NS} \propto \int_{-\infty}^{+\infty} [f_0(\beta, E - eV) - f_0(\beta, E)][1 + A(E) - B(E)]dE, \tag{3.1}$$

where $f_0(\beta, E)$ is the Fermi function at a temperature $T = 1/k_B\beta$.

In the lab, all of our measurements will be either differential resistance or conductance, so it is practical at this point to introduce the differential conductance $g(E) = (dI/dV)R_{normal}$ (*i.e.*, normalized to the normal state value) by differentiating Eqn. 3.1 by the voltage V,

$$g_{NS}(V) = (1 + Z^2) \int_{-\infty}^{+\infty} \kappa(\beta, E - eV)[1 + A(E) - B(E)]dE. \tag{3.2}$$

Here we have denoted the derivative of the Fermi function by

$$\kappa(\beta, E) = \frac{\beta \exp[\beta E]}{(1 + \exp[\beta E])^2}. \tag{3.3}$$

This is a function peaked about $E = 0$ with a width of $\sim 3.5 k_B T$, incorporating the temperature dependence into the integral. It is trivial to derive the zero temperature conductance at this point since $\kappa(E)$ reduces to a delta function at $T = 0$ and

$$g_{NS}(V)|_{T=0} = (1 + Z^2)[1 + A(E) - B(E)]. \tag{3.4}$$

One can now see that the case of a perfect barrier ($Z = 0$) corresponds to a doubling of the normal state conductance $g_{ns}(E < \Delta) = 2$ at $T = 0$ (since $A = 1$ and $B = 0$) reflecting the double-charge transfer of the Andreev process. This conductance then decreases to zero in the tunnel limit ($Z \rightarrow \infty$) as all incident electrons are reflected and Andreev transmission is suppressed. In Fig. 3.3 we demonstrate this by numerically integrating Eqn. 3.2 for a model (normal metal)/Al system ($T = 0.3$ K, $T_c = 1.4$ K). Already, at $Z = 10$, $g_{NS}(V)$ approaches that of the tunnelling case [71] which is what we expect.

3.1.2 The temperature dependence $g_{NS}(V = 0, T)$

While the above derivation outlines the voltage dependence of the differential conductance, it is also useful to write down the expression for the conductance itself. This quantity is simply the zero-bias value of Eqn. 3.2, $g_{NS}(V = 0)$. Sensitivity

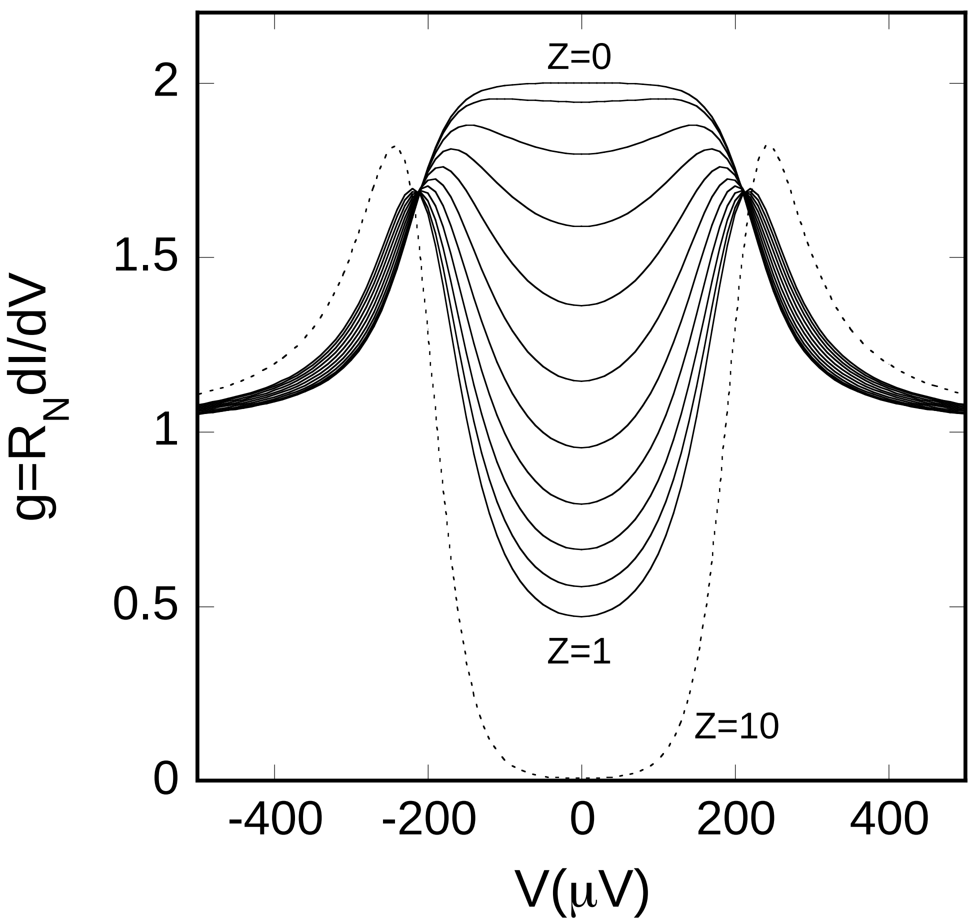

Figure 3.3: Numerical calculations of the normalized differential conductance g_{NS} at $T = 0.3$ K for various Z values. We assume a model (normal metal)/Al system ($T = 0.3$ K, $T_c = 1.4$ K) with Z stepped in increments of 0.1 (solid traces). The dotted trace shows the BTK model approaching the tunnel limit at a $Z = 10$.

to other parameters such as the magnetic field or the temperature are then incorporated into this quantity through the BTK coefficients which are functionally dependent on the gap $\Delta(H, T)$. Additionally, there is a contribution to the temperature dependence from the Fermi function derivative $\kappa(\beta, E)$ which has a width that is approximately linear in T.

The barrier parameter and reentrant behavior

As we noted previously, reentrant behavior in the temperature or energy bias is often seen in mesoscopic NS devices and is considered a particular hallmark of the proximity effect at that scale. While measurements which showed this behavior did so without measuring the NS interface as part of the sample (see for example, Ref. [63]), it should be realized that the BTK theory can reproduce this reentrant behavior as well. In Figure 3.4 we show the temperature depence of the zero bias conductance/resistance for $Z = 0$–1. In short, if one is measuring a NS (or FS) interface in series with a device, the presence of reentrant behavior is not always an indication of the proximity effect and should be verified independently of the behavior of the interface.

3.1.3 Applicability of the BTK theory to diffusive systems

As satisfying as it is to be able to numerically calculate the BTK conductances and still maintain a direct physical interpretation of the phenomenon at hand, it must be realized that the theory was originally derived for NS point contacts where the interfacial area is defined to be smaller than the mean free path. The implications are that one can ignore scattering near the interface and that the electrons may accelerate ballistically from the interface from a reservoir at equilbrium, *i.e.*, all of the potential drop occurs within a mean free path of the NS interface [69]. Later, it was learned that disorder in N could have dramatic effects since multiple coherent scattering near the interface could enhance the Andreev probability of transmission at subgap energies.[6] In addition, for interfacial areas wider than the mean free path, some sort of weighted average appropriate to the diffusive regime must be performed over the available transmission eigenvalues [13], resulting in a zero temperature conductance $g_{NS} = 1$, half the point-contact result. In short, the above complications can result in a messy analysis for many practical problems.

---

[6]For examples, see the original work of Klapwijk [72, 73] in semiconductor/superconductor structures.

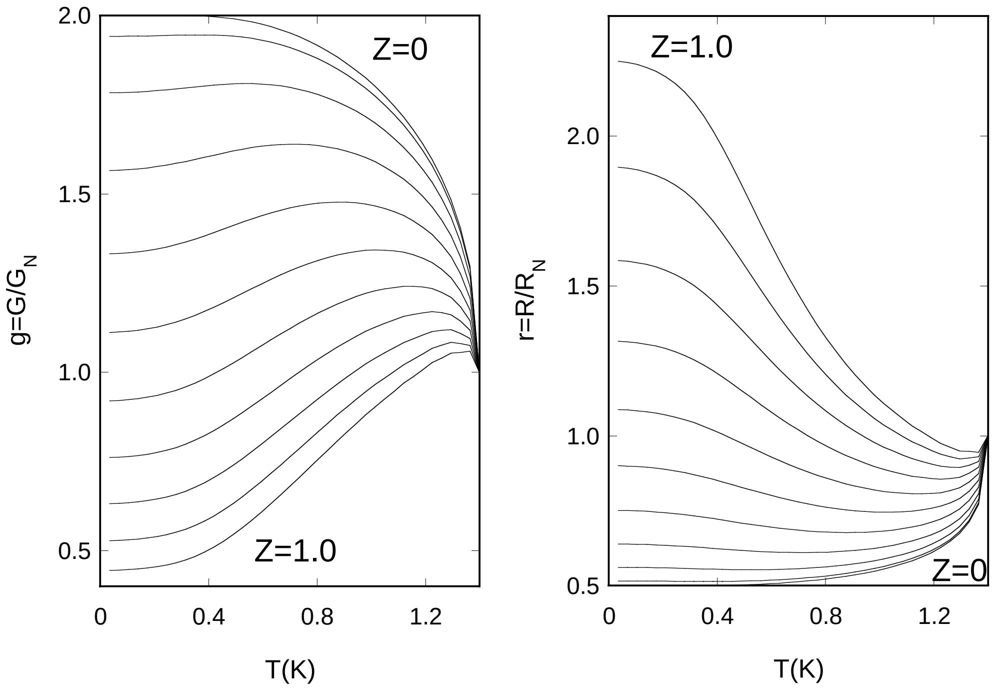

Figure 3.4: Numerically calculated reentrant temperature dependences of a NS interface. (a) Normalized conductance vs. temperature for $Z = 0$–1.0 in increments of 0.1. (b) Corresponding normalized resistance.

However, this has not stopped many experimentalists from incorporating the BTK theory as a qualitative tool [74, 75] in understanding the physics. It is in this spirit that we will approach our own data in Chapter 6.

3.2 Ferromagnet/Superconductor transport

In our experimental study of FS structures we will want to determine what aspects of spin-polarized transport will be important in our measurements. The main difference we will find between NS and FS transport is the existence of a finite spin-polarization of the ferromagnetic conduction electrons which can have a considerable effect on the BTK picture outlined above. Before we touch on this, it is useful to discuss some of the first thin-film FS experiments and what we can learn from them about spin-polarized transport.

3.2.1 FS tunnel barriers and the polarization

In the early 1970s, Tedrow and Meservey [76–78] demonstrated that the tunneling spectrum between ferromagnetic and a superconducting thin films showed an asymmetric split-peak structure upon application of a strong magnetic field (see Figure 3.5). They realized that this was a direct consequence of the imbalance between majority and minority spin populations and subsequently were able to derive the spin-polarization from the differential conductance. The following key facts made this observation possible:

- In some thin superconducting films, with a parallel applied field, the quasiparticle density of states

$$N_s(E) = \left[\frac{E^2}{(E^2 - \Delta^2)}\right]^{\frac{1}{2}}, \tag{3.5}$$

  Zeeman splits evenly into spin-up and spin-down contributions upon application of a magnetic field, $N_{s,\uparrow\downarrow}(E, H) = N_s(E \pm \mu_B H)/2$ (see Figure 3.6(a)). Experimentally, this was first observed by Meservey *et al.* [79] in thin Al films.

- The majority and minority spin bands (defined as parallel and antiparallel to the internal magnetization M) are unevenly populated such that the separate

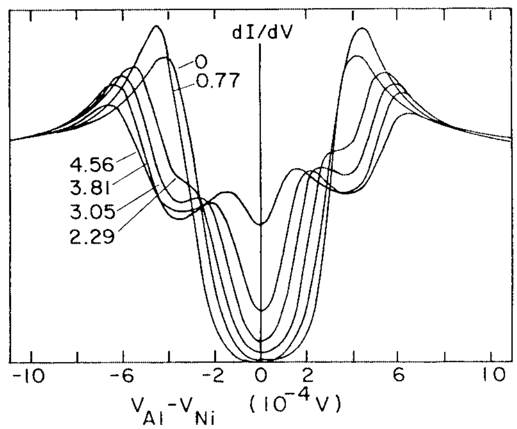

Figure 3.5: Tunnelling spectrum for an $Al/Al_2O_3/Ni$ junction for several magnetic fields (in Tesla). *(Figure taken from Ref. [78].)*

spin populations can be represented as fractions of the total electron number, $N_{f,\uparrow} = aN_f$ and $N_{f,\downarrow} = (1-a)N_f$, with a net polarization

$$P = \frac{N_{f,\uparrow} - N_{f,\downarrow}}{N_{f,\uparrow} + N_{f,\downarrow}} = (2a-1). \tag{3.6}$$

It is known that the differential tunnel conductance between a normal metal and a superconductor essentially maps the (thermally smeared) quasiparticle density of states [71] through a conductance equation very similar to Eqn. 3.2,[7]

$$g_{NS,tunnel} = \int_{-\infty}^{+\infty} N_s(E+eV)\kappa(\beta, E-eV)dE. \tag{3.7}$$

To derive the Tedrow and Meservey result, we split this differential conductance into its constituent spin up and spin down components, weighting the transmission

[7]In fact, Eqn. 3.2 reduces to Eqn. 3.7 in the high Z limit as verified by the limiting forms of the BTK coefficients A and B.

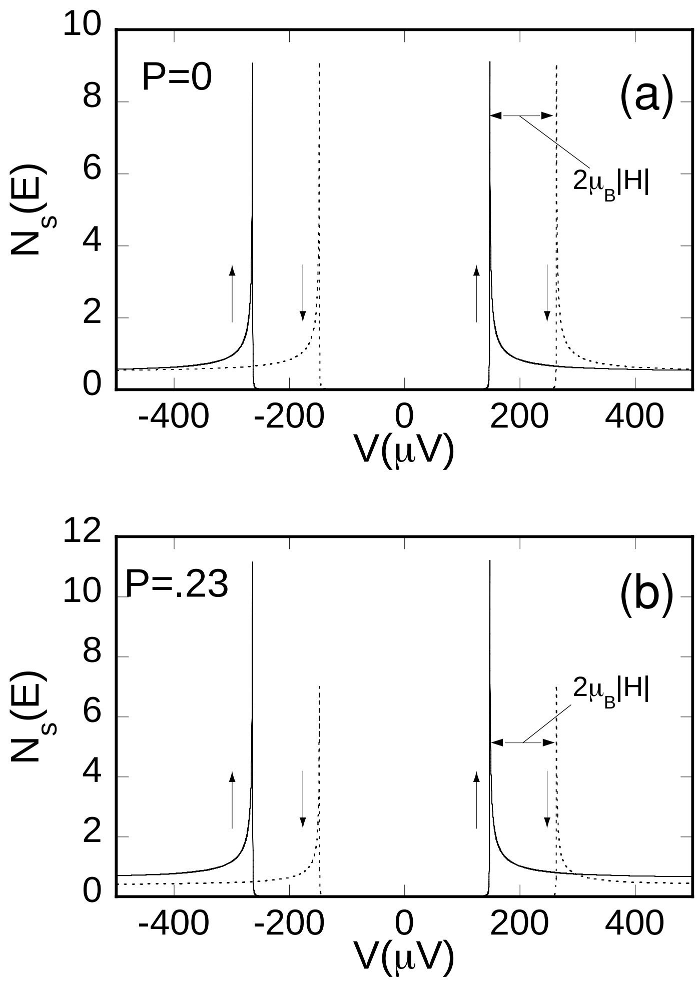

Figure 3.6: Numerically calculated Zeeman splitting of the quasiparticle density of states $N_s(E)$ with H =1 T and T_c =1.4 K. (a) N_s splits into two equal spin contributions, but (b) the effective density of states will be weighted by the polarization factors a and $(1 - a)$ (as described in the text) in the integrals determining the tunnel conductance (Eqn. 3.8).

into each of the $N_{s,\uparrow\downarrow}$ by their respective population fractions a and $(1-a)$,

$$\begin{aligned} g_{FS,TM} &= \int_{-\infty}^{+\infty} [aN_{s,\uparrow}(E,H) + (1-a)N_{s,\downarrow}(E,H)]\kappa(\beta, E-eV)dE \\ &= \int_{-\infty}^{+\infty} [aN_s(E+\mu_B H) + (1-a)N_s(E-\mu_B H)]\kappa(\beta, E-eV)dE \end{aligned} \tag{3.8}$$

These equations are easily numerically integrated and the results of such a procedure are shown in Figure 3.7(a). The calculation is performed assuming $T = 0.3$ K, a spin polarization $P = 0.23$ (corresponding to Ni [78]) and an applied magnetic field $H = 1$ T, with the other critical parameters as noted in the figure. Although the field is quite high, splitting the peaks by over 100 μV, thermal fluctuations at this temperature smooth out these features considerably, making the peaks difficult to discern. The original scheme that Tedrow and Meservey used to deduce the polarization involved the determination of all four of the individual peak heights [78] which required extremely large fields. In addition, the field requirements forced the use of very thin Al films to maximize the in-plane critical field, which further necessitated painstaking alignment in setting up the measurement, the critical point being that the Zeeman splitting should exceed the thermal energy by as large a factor as possible. It is apparent from the numerical example shown that at more reasonable fields and temperatures, it is difficult to discern these peaks precisely. The corresponding peaks in N_s (coplotted with this figure) underline the effect of thermal smearing on the apparent heights and positions of the differential conductance peaks. In this sense, the determination of the polarization can be somewhat difficult. However, a possible method for discerning the polarization may be to simply seek out the more distinct antisymmetric component. As an example, we have plotted the antisymmetric components of both g_{FN} and its corresponding $N_s(E)$ for comparison in Fig. 3.7(b). To accentuate the potential for discerning the polarization in less stringent conditions, we repeat the example for a much smaller field of $H = 0.1$ T in Figure 3.8. Even though the Zeeman splitting is minimal here ($\sim$10.6 μV), the antisymmetric component (Fig. 3.8(b)) still reveals structure that could otherwise have been ignored.

Qualitatively, the importance of the antisymmetric component is quite clear—first, its existence signifies the existence of spin-polarized transport from F into S, second, its shape determines the sign of the polarization, and third, it offers a potential method of studying spin transport in low-fields where the spin splitting may not be distinct to within the thermal bandwidth. However, one should be careful, in such an analysis, to distinguish other antisymmetric contributions such

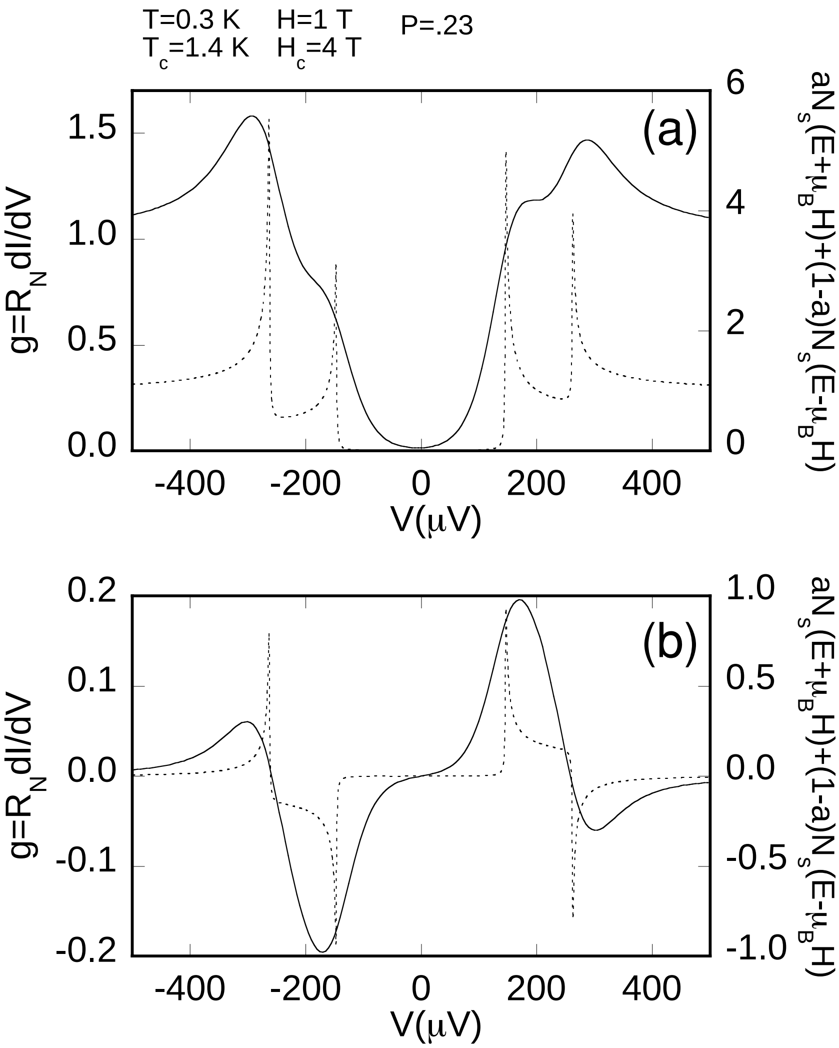

Figure 3.7: Finite temperature numerical caation of the FS tunneling conductance in a 1 T field (solid trace, left axis). The corresponding N_s has been plotted for comparison (dotted trace, right axis). (a) Full conductance trace. (b) Antisymmetric components only. Polarization is set at 23% (the value for Ni [78]). Other critical parameters are noted in figure.

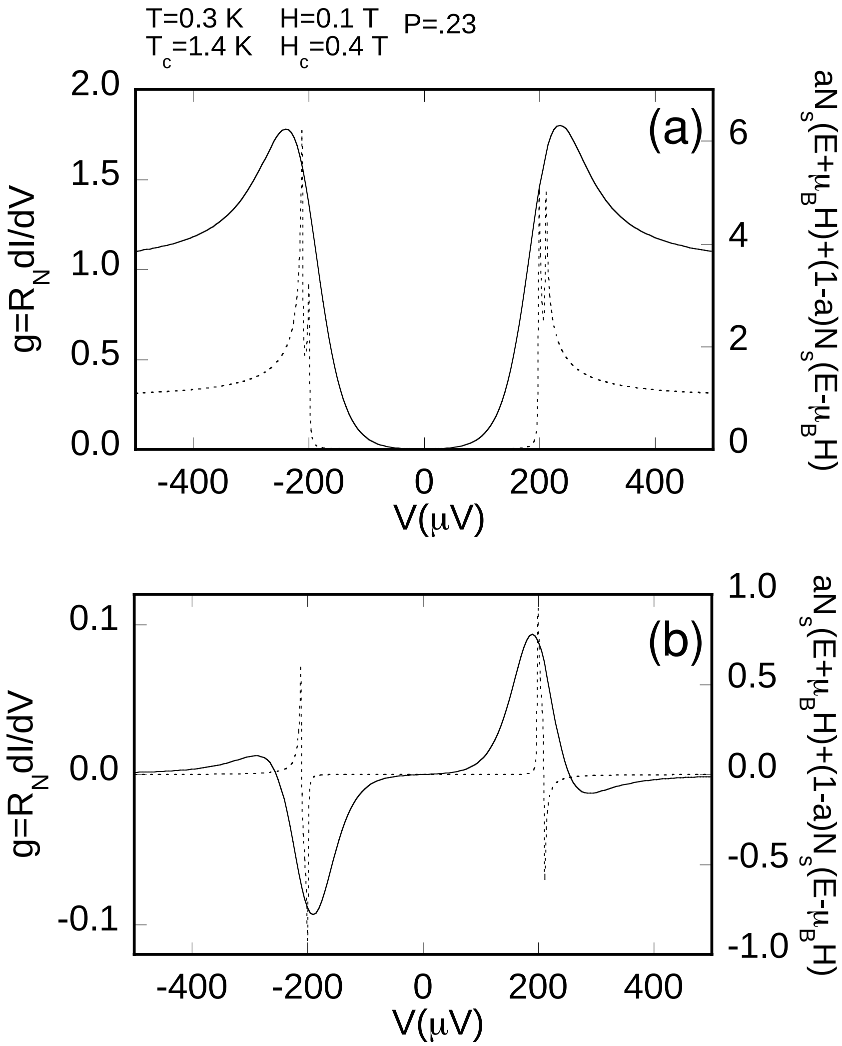

Figure 3.8: Finite temperature numerical calculation of the FS tunneling conductance in a 0.1 T field (solid trace, left axis). The corresponding N_s has been plotted for comparison (dotted trace, right axis). (a) Full conductance trace. (b) Antisymmetric components only. Polarization is set at 23% (the value for Ni [78]). Other critical parameters are noted in figure. Although peaks are indistinct in (a), they are easily discernible in the antisymmetric component (b).

as the thermopower which can be considerable in NS structures with nonuniform heating.[8]

In our work, we will be interested not only in how the superconductivity restricts conduction channels through a FS junction, but also how local magnetic fields may affect the measurement. Here, we suggest that the presence of an antisymmetry in the differential resistance/conductance, even with no applied field, may be indicative not only of spin-polarized current, but also of a Zeeman splitting in N_s which can be due to fields generated by F.

3.2.2 Adapting the BTK theory for FS systems

Some authors have already noted that Andreev reflection should limit the conduction in FS structures since the unbalanced fraction P of the total electron number cannot combine to form Cooper pairs [82–85]. Experimentalists have taken advantage of this, measuring the spin-polarization using point contact geometries in zero applied magnetic field [83–85], assuming nearly perfect contacts, and fitting the differential conductance for cases when these assumptions are relaxed. In a perfect FS contact ($Z = 0$) then the current will only be conducted by a fraction $(1 - P)$ which can Andreev reflect. This gives the zero bias conductance, $g_{FS}|_{Z=0} = 2(1 - P)$ (normalized to the normal state conductance). This gives the understandable result that the conductance should vanish at 100% polarization since there will be no paired spins available to Andreev reflect. However, the polarization estimates based on this reasoning always seem to be a bit higher than the accepted numbers found by tunneling, and these discrepancies are not yet completely understood [85]. In addition, the two techniques used so far, mechanical point contacts [83, 84] and thin film nanocontacts [85], disagree greatly for some ferromagnet polarizations. In any case, this prescription is physically transparent and may be adapted to other measurements such as the temperature dependence of the zero-bias conductance/resistance in a straightforward manner.

For later comparison with our data, we have adapted the BTK model, accounting for the attenuation of the Andreev coefficient with the substitution $A \rightarrow (1 - P)A$, and weighting the different spin-subchannels by the spin fractions a and $1 - a$ as in the tunneling case shown previously.[9] Results of such a calculation

---

[8] An example of NS thermopower (and its phase dependence) can be found in earlier work by our group by J. Eom *et al.* [80, 81].

[9] A more detailed calculation along these lines has recently been published by Mélin [12].

are shown in Figure 3.9 for the same parameters as Figs. 3.7 and 3.8 except that we have varied the Z values slightly to show the evolution of the antisymmetric component. It comes as no surprise that the antisymmetry of the spin-channel transmission is also revealed in the case of an arbitrary barrier height, but in the metallic contact limit ($Z = 0$), the component seems to switch sign. This occurs because the weighted peaks in N_S at $eV = -\Delta + \mu_B H$ and $+\Delta - \mu_B H$ can not be distinguished from the flat region between the peaks where the transport is dominated by Andreev reflection. Therefore the only peaks in N_S available to give antisymmetric components are the "outside" peaks at $eV = -\Delta - \mu_B H$ and $\Delta + \mu_B H$, hence the apparent sign switch is really a lack of weighted peak structure from the "inside" peaks.

3.2.3 Other theories

Our approach to FS transport has been limited to only BTK-type transmission here. We have ignored nonequilibrium spin and charge imbalance effects far from the interface largely because they have only marginal relevance to the experimental results discussed in this thesis (Chapter 6). However, even dismissing the possibility of a mesoscale proximity effect in typical transition metal ferromagnets, spin-accumulation and charge-imbalance may both play significant roles as nonequilibrium transport phenomena. Spin-accumulation has recently been discussed by Belzig *et al.* [11] as a possible candidate for many of curious results presented in the experiments so far [6,9]. The central concept is that a spin-accumulation must occur at the interface in F due to a theorized short quasiparticle spin-diffusion length in S. This buildup of nonequilibrium spin should result in an increase in resistance below the superconducting transtion [10]. The results of Belzig's theory seem to account for almost all of the qualitative features of the results in Refs. [6,9], taking into consideration the geometries of their interfaces. We note that the theoretical approach in Ref. [11] is contained in a more appropriate general framework, with the ability to analyze ballistic, diffusive and dirty FS interfaces, yet it is certainly an order of magnititude more difficult than the BTK approach shown here. We should also remember that although the BTK approach reveals much of the qualitative physics behind NS and FS interfaces, it is still presented here as a model restricted by point-contact assumptions [69] and should always be regarded under this caveat.

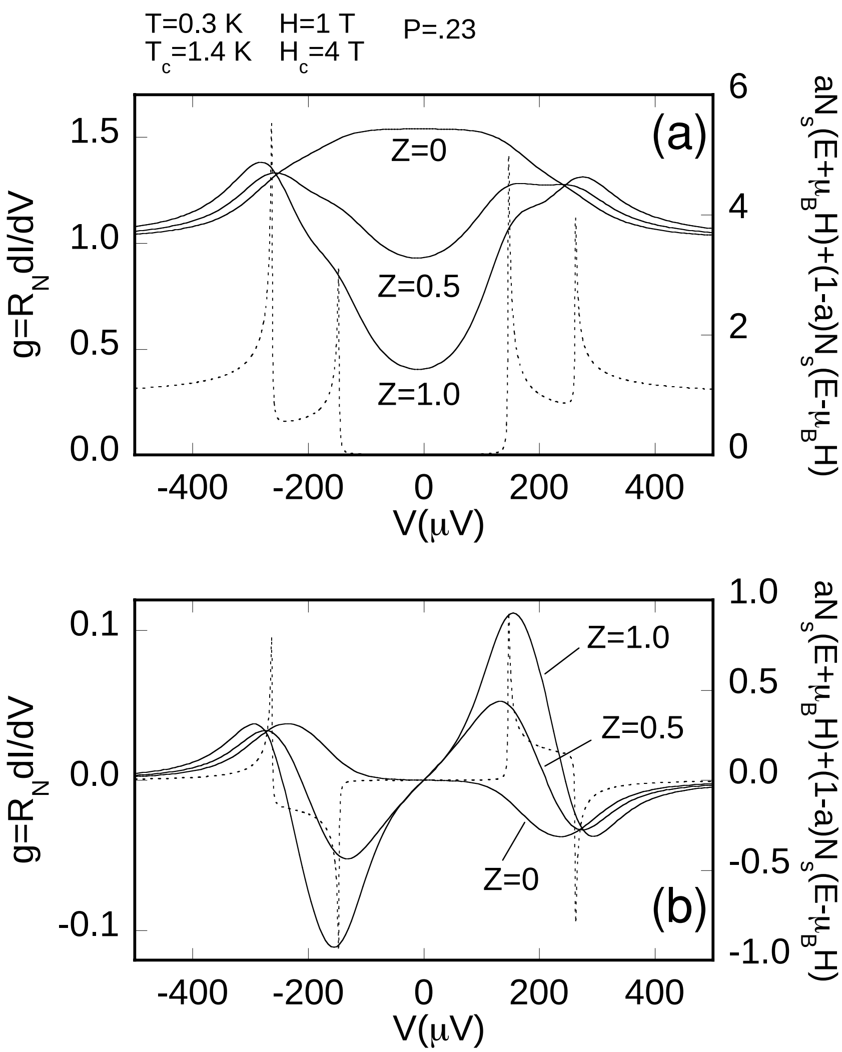

Figure 3.9: Finite temperature numerical calculation of the FS BTK tunneling conductance in a 1 T field for various Z values (solid traces, left axis). The corresponding N_s has been plotted for comparison (dotted trace, right axis). (a) Full conductance trace. (b) Antisymmetric components only. Polarization is set at 23% (the value for Ni [78]). Other critical parameters are noted in figure.

Chapter 4

EXPERIMENTAL TECHNIQUES

To complete the experiments described in this thesis it was necessary to employ a number of established lithographic, cryogenic and measurement techniques. In this chapter, we will discuss general methods, ranging from nanolithography to cryogenics, as well the specific considerations made for micromagnetic transport.

Much of the equipment and many of the techniques that were used to complete the experiments described in this thesis were built and perfected by two previous graduate students in our group, Chen-Jung Chien and Jonghwa Eom and are described in their respective theses [81, 86]. When possible, we will refer to these works for specific details since much of the methodology is identical and, instead, concentrate on this author's contributions and improvements/modifications to our existing technical base.

4.1 Device fabrication

The devices described in this thesis are patterned by standard bilayer e-beam lithography techniques onto an oxidized Si wafer. Contact to the devices is made via large area photolithographically patterned Ti/Au pads. The devices themselves are comprised of metal (Ni, Au, Al) thin films evaporated using an e-gun evaporator of the author's construction. Since all of our devices are comprised of multiple metal layers, it is not uncommon for a device to be subjected to five lithography cycles (including photolithography). For this reason, it is important that all processes are optimized for yield and many of the processes outlined below are the result of much trial and error. All wafer and resist processing takes place in a class 1000 clean room to help eliminate lithography problems due to airborne particulate matter.

4.1.1 Wafer preparation

The substrates utilized in this study are 0.020″ thick Si (100) wafers oxidized by the supplier.[1] Prior to any lithography, a new batch of wafers is analyzed by atomic force microscopy to ensure a roughness of less than 50 Å. This is important since our films are on the order of only a few hundred Å.

We clean the surface prior to the coating of any resists since any particulate matter or unwanted chemical contaminants can render our lithography efforts pointless. After dicing the substrates to suitable dimensions, we clean the substrates successively in methanol, acetone and isopropyl ultrasonic baths. The ultrasonic baths eliminate residual Si particles from the dicing process, dissolve any salt contaminants, and degrease the surface. The samples are then blown dry with N_2 gas immediately upon withdrawal from the isopropyl bath and placed in a covered container until resist coating.

4.1.2 Photolithography

The measurement of submicron metal structures necessitates the presence of large metal pads to which we can wirebond, connecting the devices to the outside world. While e-beam lithography is suitable for patterning both the fine structures and the larger contact pads, it is often preferable to pattern the large contact pads using photolithography since one can fabricate many of these large area patterns simultaneously.

For the patterning of the large area contact pads we use the following steps (*see* Figure 4.1):

1. *Coat.* Spincoat wafer with S1813 photoresist[2] at 6000 RPM for 90 s to yield a $\sim$1.1 μm thick coating. Resist is dropped onto substrate prior to starting spinner.

2. *Bake.* Bake substrate in a convection oven at 90°C for 30 min, driving out the solvent. This is usually called the "soft bake."

3. *Exposure.* Expose the substrate in a Quintel Q-20001CT mask aligner[3] using

---

[1] Polishing Corporation of America, Santa Clara, CA

[2] produced by Shipley, Marlborough, MA, but distributed by MicroChem Corp., Newton, MA

[3] Quintel Corp., San Jose, CA

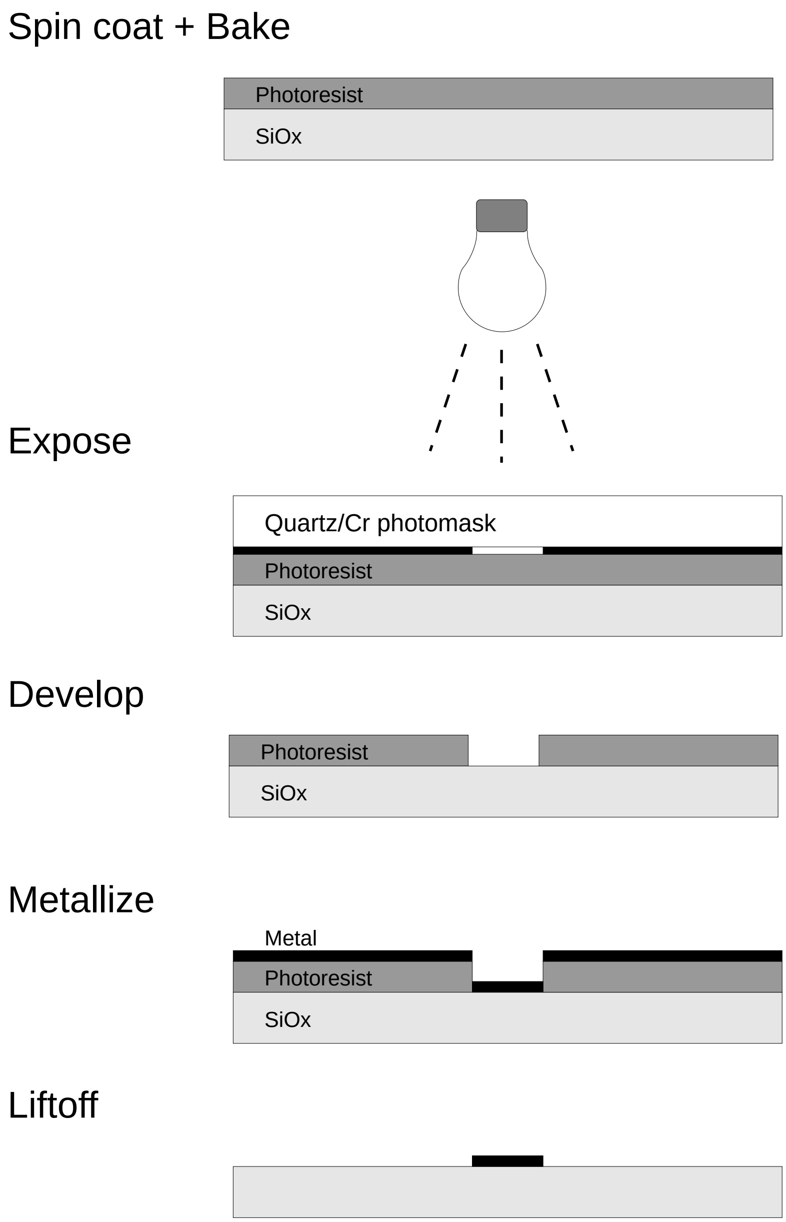

Figure 4.1: Schematic view of photolithography process *(see text)*.

a Cr on quartz photomask[4] with a UV exposure time of 10-20 s (dependent upon the condition of the lamp).

4. *Development.* Develop the patterns by immersing the substrate in Microposit MF-319 developer solution[5] for 30 s at room temperature. The substrate is withdrawn from the solution while rinsing the surface with deionized water and blown dry with N_2 gas.

5. *Metallization.* Deposit 25 Å Ti (4N5) (for adhesion) and 225 Å Au (3N5) by e-gun deposition at 1–5$\times 10^{-7}$ Torr.

6. *Liftoff.* Soak in room temperature acetone for at least 10 min to dissolve photoresist and remove unpatterned metal coating.

Usually, it is customary to harden the top surface of the photoresist using a chlorobenzene soak [81], giving an undercut profile which improves liftoff [81]. However, this yields inconsistent results with our devices. More often than not, the Ti/Au metal layers creep onto the sidewalls, giving a ragged edge (or crown) upon liftoff which can be detrimental when trying to deposit connecting probes (*see* Figure 4.2). We circumvent this problem by soaking the large area patterns in an ultrasonic acetone bath for 1–2 hrs at room temperature. Since the Ti adheres so well to the substrate the patterns always remain stuck to the substrate while the ragged edges are broken off, providing clean 300 Å step edges (*see* Figure 4.3).

4.1.3 E-Beam lithography

After suitable large area contact pads have been prepared by photolithography and metal deposition, we follow a similar series of steps to write our submicron patterns with e-beam lithography. We use a resist bilayer which provides an excellent undercut profile and has been found to improve liftoff properties in many mesoscale devices [87].

---

[4]The photomask was designed by the author and produced by Align-Rite Corp., Burbank, CA.

[5]produced by Shipley, Marlborough, MA, but distributed by MicroChem Corp., Newton, MA

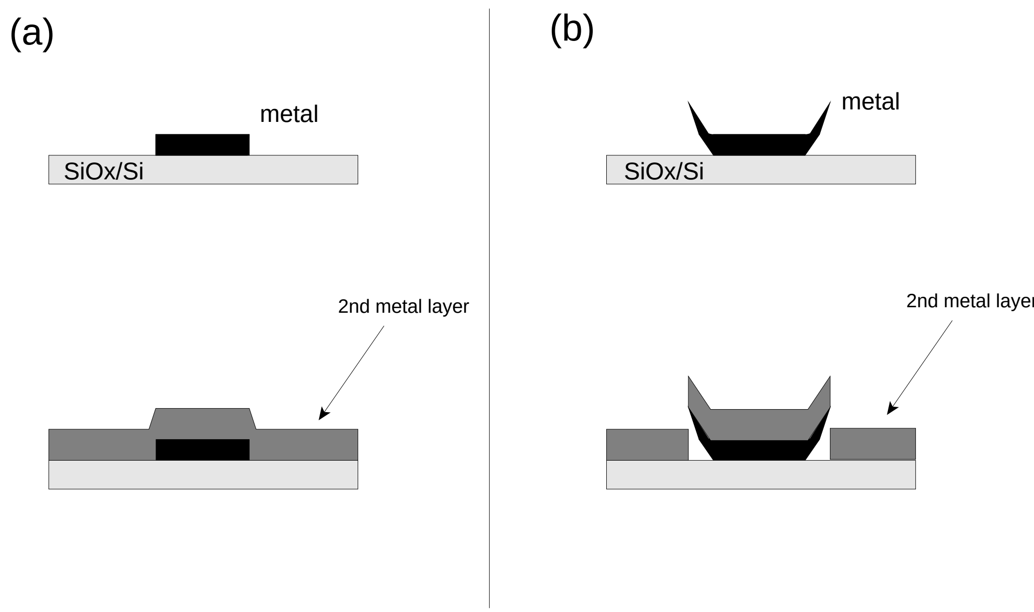

Figure 4.2: Schematic view of contact between a second metal layer and (a) clean edges of a photolithographed Ti/Au layer and noncontact to (b) ragged edges left by inadequate undercut.

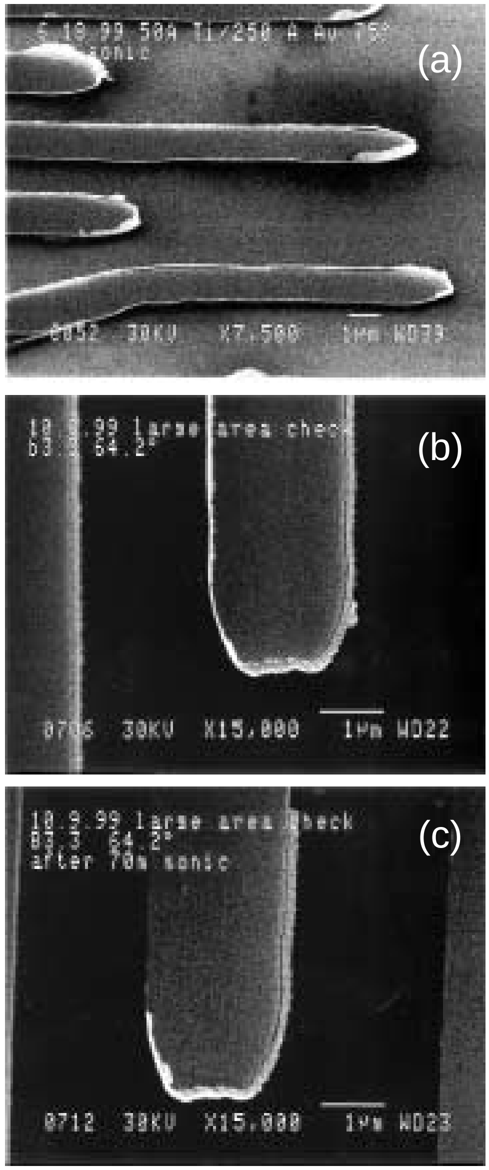

Figure 4.3: Scanning electron micrographs of (a) ragged Ti/Au large area pattern, (b) closeup of ragged Ti/Au probe before ultrasonic treatment and (c) after 70 min in ultrasonic acetone bath. In (c) we see a large part of the ragged flap on the left hand side has been shaken off, leaving a clean Ti/Au step which can easily be contacted to in subsequent depositions.

1. *Coat.* Spincoat wafer with NANO™100 PMMA A4 resist[6] at 3000 RPM for 45 s, yielding a ∼100 nm layer thickness. Resist is dropped onto the substrate within a second of starting the spinner to ensure an even coating.

2. *Bake.* Bake in a convection oven at 180°C for 1 hr. Allow to cool at room temperature for at least 15 min, then ...

3. *Coat again.* Spincoat NANO™495 PMMA A4 resist[7] at 8000 RPM for 45 s, yielding a ∼100 nm layer thickness. The resist is dropped onto the substrate while spinning (as in Step 1), minimizing the dissolution of the first PMMA layer by the solvent in the second.

4. *Bake.* Bake in a convection oven at 180°C for 1 hr. Allow to cool to room temperature.

5. *Exposure.* Expose fine patterns in JEOL JXA-840[8] scanning electron microscope using an electron beam.

6. *Development.* Develop patterns by immersing wafer in a 1:3 methyl isobutyl ketone (MIBK)/isopropyl alcohol(IPA) solution at 23° for 45 s. The surface is rinsed with isopropyl alcohol as the wafer is withdrawn from the solution and then blown dry with N_2 gas.

E-beam notes (and the art of fine alignment)

The actual patterning is performed using a JEOL JXA-840 scanning electron microscope, with the beam directed by a Windows program developed by Prof. V. Chandrasekhar. The PC is connected via a D/A card[9] and an external x-y beam control module supplied by JEOL [86]. A typical exposure is performed with a charge dosage of 400 μC/cm^2, at magnifications of 1000–8500×. In practice the dosage

[6] 100K molecular weight polymethyl methacrylate dissolved in anisole, MicroChem Corp., Newton, MA

[7] 495K molecular weight polymethyl methacrylate dissolved in anisole, MicroChem Corp., Newton, MA

[8] JEOL, Boston, MA

[9] Microstar Laboratories, Inc., Bellevue, WA

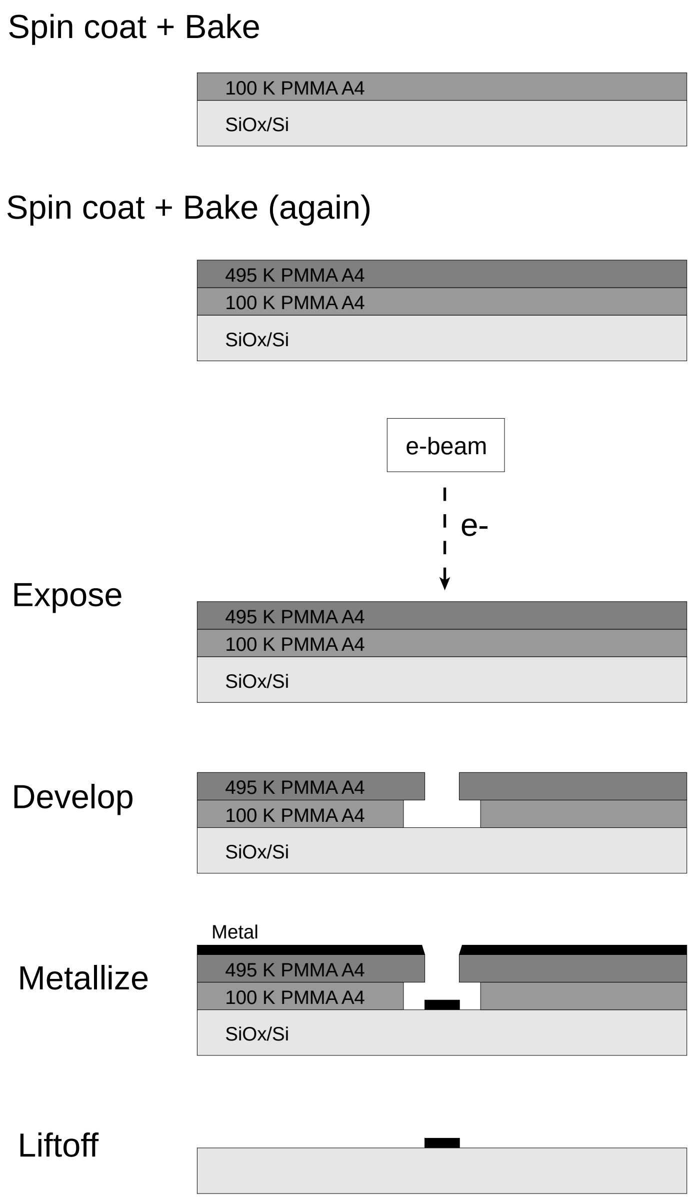

Figure 4.4: Schematic view of e-beam lithography process *(see text)*.

must be tuned for various patterns due to proximity exposure effects, while the magnification is chosen to minimize the total possible exposure field with respect to the device dimensions. In addition, the sample is brought as close to the beam aperture as possible. This increases the resolution by bringing the sample closer to the objective lens and also minimizes the beam path length (thereby reducing the effects of external vibration and electrical noise which can shift the beam).

In fabricating these devices, the most difficult part of the process is the alignment. All of the devices presented are comprised of two or more metallic layers which must be aligned to within 50-100 nm. This can be tricky since there are a number of ways the sample alignment may shift due to many sources of image shift in the JXA-840 SEM. If a sample is fabricated from three different layers requiring fine alignment (as in our normal/ferromagnet/superconductor devices), mistakes in alignment can reduce the final yield by a substantial amount which can make the entire process very frustrating. Over the years we have developed an alignment system appropriate to our SEM and patterning program. This procedure is somewhat detailed and specific to our setup and for this reason, we do not include it here.

4.1.4 E-Gun deposition

All metal deposition took place in a diffusion-pumped e-gun evaporator of the author's design (see Figure 4.5).

The main chamber (or "service well") was designed in AutoCAD[10] and submitted to an outside manufacturer[11] for construction. The chamber is constructed from nonmagnetic 304 stainless steel with a number of ports that can be outfitted with an assortment of mechanical, cooling line and electrical feedthroughs, while a large surface is provided at the top to seal with an 18″ quartz bell jar.

The chamber is pumped by a six-inch (ASA 6) diffusion pump[12] backed by a strong mechanical pump.[13] To stop diffusion pump oil from backstreaming into the chamber, we use a liquid nitrogen cold trap[14] with a holding time of 10–17 hrs.

---

[10]Autodesk, Sausalito, CA

[11]HPS Division, MKS, Inc., Boulder, CO

[12]Varian VHS-6 diffusion pump, Varian, Lexington, MA. The pump used in our system is actually refurbished by the author.

[13]Welch 1397, W. M. Welch Scientific Company, Chicago, IL

[14]Varian 362-6 cryotrap, Varian, Lexington, MA.

The combined pumping stack is capable of pumping at 1100 ℓ/s, providing a rapid turnaround time for many of our depositions.

Substrates are mounted $\sim$ 380 mm from an five-pocket 3 kW e-gun source[15] which is powered by a 4 kV power supply.[16] The deposition itself takes place once the system pressure has fallen to $\sim$1–3$\times10^{-7}$ Torr. We mount the samples directly over the source such that the source evaporant impinges the sample surface at normal incidence. The sources are held in a water-cooled copper hearth which is lined with a variety of crucible liners depending on the source material.[17] Finally, the film thickness is monitored using an quartz oscillator bridge.[18]

4.1.5 Plasma etching

dc O_2 etching

Many metals have difficulty adhering to Si/SiOx surfaces and this condition is sometimes exacerbated by the presence of PMMA residue. To avoid this difficulty we perform a dc O_2 plasma etch[19] in a simple stainless steel chamber assembled by the author from 2-3/4″ UHV and KF-40 HV components[20]. The samples are mounted on a grounded stainless steel plate, with a mirror electrode $\sim$3/4″ away. O_2 glass is flowed through a needle valve/mechanical pump combination giving a chamber pressure of $\sim$110 mTorr. The plasma is generated by an external power supply generating a -700 V potential between the electrodes with a quartz tube surrounding the electrodes to confine the plasma. The oxygen plasma has the effect of reacting with organic residues on the substrate (such as PMMA residue) and ionizing them such that they can be pumped away. In this configuration, we find that a plasma etch time of 25 s etches away $\sim$200 Å of PMMA, which is suitable for etching any PMMA residue without destroying the undercut profile. Using this method, we find that Au adheres quite well to our Si/SiOx substrate in comparison

---

[15] Model 528-5 e-gun, TFI Telemark, Fremont, CA

[16] DEG 744, Denton Vacuum, Cherry Hill, NJ

[17] Ni (4N5) is deposited straight from the Cu hearth (or from a Cu liner), while Au (5N) is deposited from W crucible liners and Al (5N) is deposited from intermetallic liners (TiB_2-BN). Crucible liners are obtained from Kamis, Inc., Mahopac Falls, NY.

[18] Model XTM/2 deposition monitor, Leybold Inficon, Inc., East Syracuse, NY

[19] This is sometimes called "plasma ashing" in the literature [88]

[20] Kurt J. Lesker Co., Clairton, PA

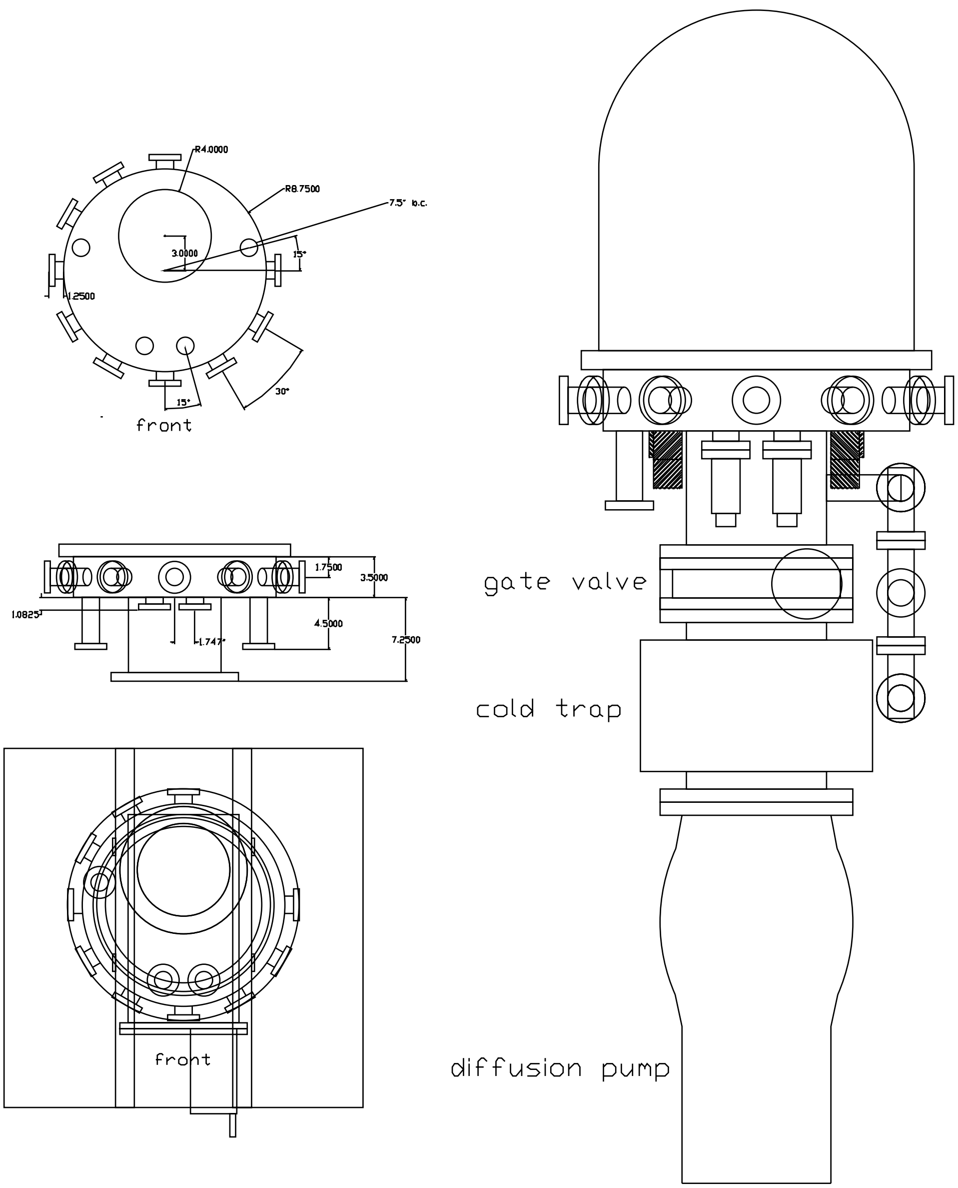

Figure 4.5: Some of the original AutoCAD designs used to construct the e-gun evaporation system.

to nonetched substrates. We use this method whenever possible as it is the most reliable way to eliminate residue and improve adhesion.

ac Ar$^+$ etching

To measure our Ni particles, we require good electrical contact with the subsequently deposited Au and Al layers since these will serve as our transport probes. To achieve this, it is necessary to clean the surface of the already deposited Ni, improving contact to Au or Al layers deposited on top. We cannot use the oxygen plasma procedure detailed above since the Ni is susceptible to oxidation. Instead, we perform a very similar procedure, using Ar in an ac field, essentially sputtering material off of the substrate. This has the advantage that it does not oxidize the underlying Ni, although it may damage the surface somewhat if one is not cautious. The etch parameters are very similar to the oxygen process, with the pressure and time being identical, but with an applied 1 kHz ac field of ~380–400 V rms.

4.2 Electrical transport measurements

4.2.1 Cryogenics

Many of the transport properties of interest to us are seen only at low temperatures (*e.g.*, quantum interference and superconductivity) so it is necessary to perform our measurements using a low temperature cryostat. Most of the measurements in this thesis are performed using a closed cycle ^{3}He cryostat[21] [89] capable of a minimum temperature of 260 mK, although early measurements in single-particle ferromagnetic transport were taken using a fixed impedance pumped ^{4}He cryostat (built by J. Eom) capable of a minimum temperature of ~1.1 K. These cryostats are loaded into a liquid He bath that provides ambient cooling through thermal contact as well as a source of ^{4}He for their respective 1K pots. Associated pumping lines were constructed from PVC pipe by the author, with the corresponding pumps located in a separate room on the floor below, which helped isolate the cryostat from mechanical pump vibrations. The ^{4}He dewar and cryostat system are situated on a platform which is isolated from the surrounding floor, providing most of our vibration isolation.

The samples are mounted on the end of a Cu cold finger which is weakly coupled to either a 1K pot (pumped ^{4}He system) or a ^{3}He pot (closed cycle ^{3}He system)

[21] Janis Research Company, Inc., Wilmington, MA

with the entire assembly residing inside a cone-sealed brass vacuum can isolating the sample from exchange gas heat leaks to the external ^{4}He bath.

4.2.2 Temperature measurement and control

Temperature is measured using a calibrated RuO_2 thin film surface mount resistor potted in a small amount of epoxy[22] which, in turn, is potted in thermal heat sink compound[23] in the Cu cold finger. The measurement itself is a four-probe ac lock-in measurement which is performed by a custom bridge circuit designed and built by J. Eom [81]. RuO_2 is a Mott insulator and has a strong temperature dependence at low temperatures, rising as it is cooled. Below 10 K, this resistance is generally in the 1–10 kΩ range and care must be taken to avoid self-heating. To this end, we use low excitation currents of 2–200 nA.

Temperature biasing is accomplished using a homemade proportional-integral-differential (PID) feedback circuit [81, 86] which takes an error signal from the thermometer bridge circuit and outputs to a heater situated opposite the resistance thermometer on the cold finger. The PID parameters are sensitive to the setpoint value and are determined by trial and error.

In temperature dependence studies we bypass the PID entirely and ramp the voltage on the heater directly through a low-pass filter (to eliminate digital output spikes) using a computer-controlled voltage source.[24]

4.2.3 Magnetic field control

Magnetic fields can be applied to our samples using conventional superconducting magnet technology. However many of our magnetotransport measurements are dependent upon the direction of the field and so it is desirable to have some system for rotating this field. Since our samples are mounted with the surface normal parallel to the cryostat, it is impossible to rotate the field in the substrate plane with conventional superconducting solenoid designs. In our early single particle measurements, we needed to apply the field in the substrate plane, so we mounted the sample on a socket adapter (machined from Stycast 1266 epoxy) which brought

[22]Stycast 1266, Emerson and Cuming, Canton, MA

[23]DC 340, Dow Corning Corp., Midland, MI

[24]Keithley 230, Keithley Instruments, Inc., Cleveland, OH

the substrate plane in-line with the solenoid axis.[25] This solved only half the problem since it was still impossible to rotate this field in the substrate plane very easily. To remedy the situation, we purchased a two-axis superconducting magnet system[26] which had a 1.8 T split coil (which directs a field perpendicular to the cryostat axis) and a 3 T solenoid (parallel to the cryostat axis). With the substrate mounted conventionally, the split coil can apply a field in the substrate plane, while the solenoid applies a field out-of-plane. Using this two-axis combination, we are able to measure magnetotransport with the magnetic field applied in-plane as well as out-of-plane. In order to rotate the field in-plane, we simply rotate the cryostat about its axis, effectively rotating the sample with respect to the split-coil axis.

The magnets are powered using off-the-shelf high current power supplies (PS). In practice, we have utilized three different PS systems: a 20 A bipolar supply,[27] a 120 A bipolar superconducting magnet supply,[28] and a pair of unipolar supplies coupled together to give bipolar output.[29]

The unipolar supplies were operated using a circuit design due to A. Benoit (then at IBM Watson Research Laboratory) for the HP 6260 series PS and was constructed by the author (see Figure 4.6). The circuit shown in Fig. 4.6, operates the magnets in voltage control mode, applying a constant voltage to the magnet leads (using an computer controlled voltage source), giving a constant charging rate. To get bipolar operation, a second unipolar supply is coupled to the first with opposite polarity, with the control circuit attached solely to the first supply.

Each of these systems has their distinct advantages. The coupled unipolar PS system is best suited for high current/high field voltage-biased magnet control, while Kepco bipolar PS is suitable for low/medium field current bias control.

4.2.4 Data acquisition

The data acquisition is performed by a DOS-based Pascal program written by Prof. V. Chandrasekhar and J. Eom. The program is GPIB-capable and was used to

[25] For early measurements we used a 6 T solenoid supplied by Kadel Engineering (Danville, IN)

[26] Cryomagnetics, Inc., Oak Ridge, TN

[27] Kepco BOP 20-20M, Kepco, Inc., Flushing, NY.

[28] Lakeshore 622, Lake Shore Cryotronics, Inc., Westerville, OH

[29] HP 6260B and HP 6388, Hewlett Packard, Cupertino, CA

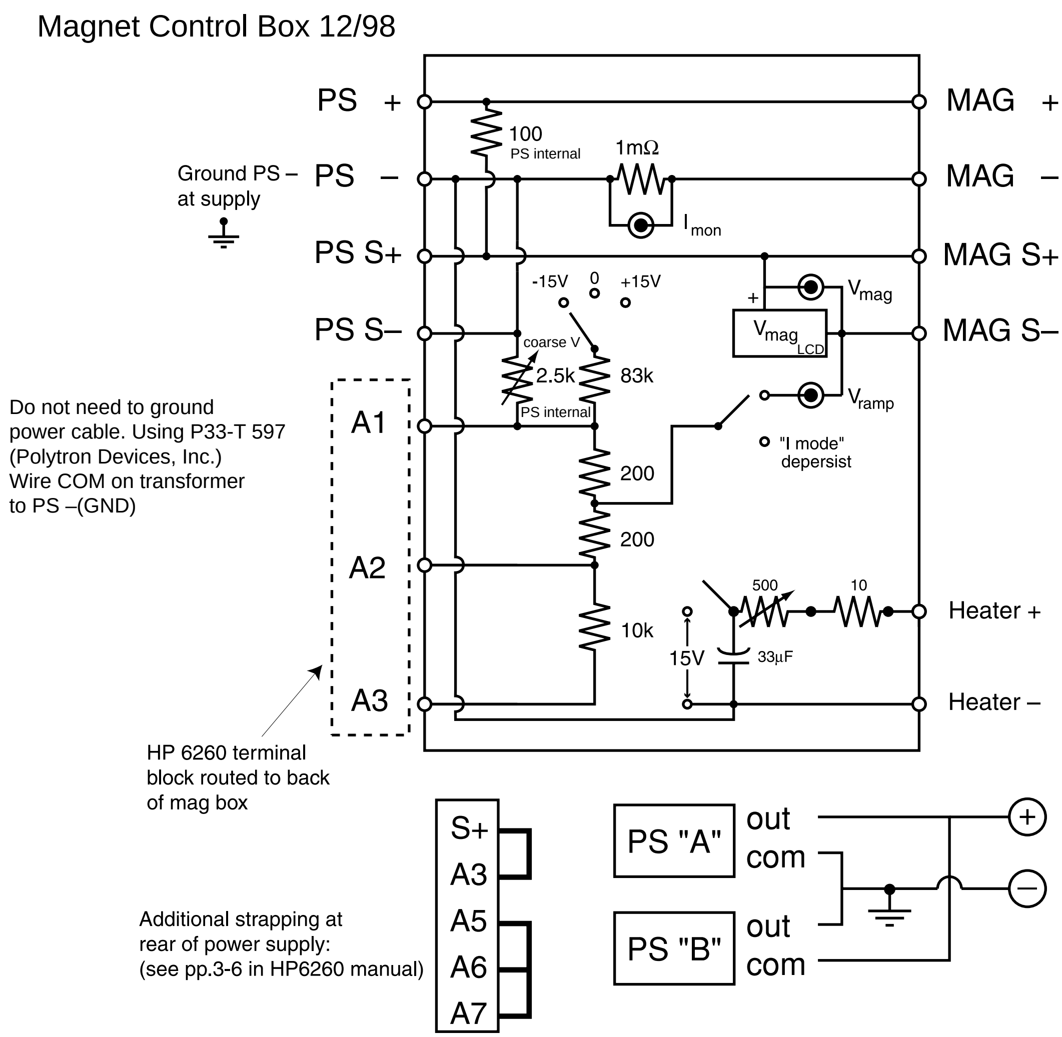

Figure 4.6: Magnet control circuit for use with HP 6260 series power supplies (design due to A. Benoit). For bipolar operation, a second supply is coupled the first with opposite polarity.

both monitor our multimeters[30] and ramp temperature, magnet and bias voltage with a programmable voltage source (Keithley 230).

4.2.5 Data lines

When extending the data lines from room temperature to low temperature the primary concerns are thermal and RF noise isolation. The thermal isolation is achieved using superconducting twisted pairs (NbTi in a CuNi matrix) which, at low temperature, connect to Cu twisted pairs wound around the Cu cold finger. The RF isolation is performed by a set of π-section filters at room temperature and eliminates heating at the sample due to high frequency noise currents [81].

4.2.6 Wirebonding and device verification

Prior to wirebonding, we examine the devices using our SEM. This is to verify that the sample is visually continuous and that there are no unwanted shorts. The sample is then mounted on a custom thirty-two pin header using silver paint and wirebonded using 0.001″ Al wire (1% Si) in a wedge bonder.[31] After the device is bonded and the probes are annotated for future reference, we check the electrical continuity by plugging the header into its corresponding socket on the cryostat itself. This check is performed at room temperature with a battery-powered multimeter.[32] If the sample is okay, we proceed to seal up the vacuum can and prepare for cooldown. At this point, we can also perform room-temperature diagnostic four-probe measurements to begin characterizing our devices.

4.2.7 ac lock-in techniques: R, dV/dI and dI/dV

To study electronic transport, we employed three basic ac measurements in this study: zero- and finite-bias differential resistance (R, dV/dI) and differential conductance (dI/dV). The first two are four-probe measurements and are suitable for low-resistance samples while the last is most useful for high resistance samples which require a high dynamic range.

[30] HP 34401A, Hewlett Packard (now Agilent Technologies), Cupertino, CA

[31] Kulicke and Soffa 4123, Kulicke and Soffa, Inc., Willow Grove, PA

[32] Fluke 79, Fluke Corp., Everett, WA

Resistance

The resistance is measured using a differential ac technique [38] with an Adler-Jackson type bridge [90]. The bridges are decade resistors[33] which we have modified according to the circuit shown in Figure 4.7. The excitation current is generated by an external voltage which is taken from our lock-in amplifier. This voltage is isolated from the oscillator ground by an 1:1 isolation transformer and applied across a set of extremely stable 1 MΩ resistors,[34] providing a near-ideal current source at the sample. The points "A" and "B" are attached to the differential input of a PAR 116/116A which in turn sends the signal into a PAR 124/124A lock-in amplifier[35]. The voltage $V_{AB}(\equiv V_A - V_B)$ measured by the lock-in amplifer must be phased with respect to the excitation current, since various inductances and capacitances in the leads may generate an out-of-phase component. We can adjust the phase to the resistive part of the signal by toggling decades in the balancing bridge resistor and checking that the lock-in signal does not shift. This phase angle is then the pure imaginary component and lies $\pm 90°$ from the real (resistive) component.

In general the excitation currents are chosen such that the voltage drop across the sample is a fraction of $k_B T$ and there is minimal self-heating. Even with this restriction, small signals can be well-resolved in this setup, with the main source of noise arising from Johnson noise in the bridge's decade resistor. For extremely small signal changes (*e.g.*, a few nanovolts) and small source impedances, it is preferable to operate the PAR 116/116A in "transformer mode" which couples the A-B inputs to the preamplifier using a 1:100 audio transformer. In practice, our small resistance samples (a few Ohms) and our lead lines provide a source impedance of less than 100 Ω and the resulting gain is less than ten at 11.7 Hz. Although this is not quite the ideal gain of one hundred, it is a considerable improvement over "direct mode" and we have been able to achieve a signal resolution $\sim$0.5 nV rms with reasonable time averaging intervals. We try to use the lowest excitation frequencies possible in these measurements (especially transformer mode) since there can be quite a lot of common mode drift in our longer runs (*e.g.*, typically 8–12 hours for our high field single ferromagnetic magnetoresistances) and the common mode rejection ratio of the PAR 116/116A tends to drop substantially at higher

---

[33]General Radio 1433-X and 1433F, General Radio Co., Concord, MA

[34]Vishay Resistive Systems Group, Malvern, PA

[35]Princeton Applied Research, Princeton, NJ

frequencies. For this reason we use only excitation currents below 100 Hz and all of the small signal measurements (*i.e.*, conductance fluctuations) are measured at 11.7 Hz.

In samples where the lead line resistance may change substantially (such as the superconducting leads in our ferromagnetic/superconductor devices), it is important to *not* use transformer mode in the PAR 116/116A since the gain can be a strong function of the source impedance in our frequency regime. Ignoring this aspect, one may observe spurious changes in the off-balance voltage V_{AB} at the superconducting transition as the gain shifts, even though there may be no real change in the sample itself. For this reason, it is often advisable to the check the gain and phase both above and below any superconducting transitions in the system.

Differential resistance: dV/dI

The measurement described above is a differential measurement, except that it essentially determines the resistance only at zero current bias. Therefore, all that is necessary to measure the finite-bias differential resistance is to insert a current bias at I_+. We do this using a homemade voltage-to-current converter [81, 86], routing the current through a 10 kΩ resistor so that it can be monitored (see Fig. 4.7). We use a GPIB-compatible voltage synthesizer[36] to source the converter so that the current bias can be controlled by our data acquisition program as well as by front panel controls. Using this setup we can ramp the current over ranges of microamps to hundreds of microamps at frequencies as low as a microhertz. It should be pointed out, however, that even a bias of a few microamps can heat mesoscopic devices appreciably at low temperatures [91] and must always be considered when analyzing these measurements.

Differential conductance: dI/dV

Conductance can be more practical to measure than the resistance in high-resistance junction devices. As an example, tunnel junction interfaces between normal metals and superconductors may show a finite resistance above the superconducting transition, yet approach infinity as the temperature approaches zero, making a temperature dependence impossible to measure due to insufficient dynamic range in the lock-in. Conversely, the conductance may be some finite value above the

[36] HP 3325A, Hewlett Packard, Cupertino, CA

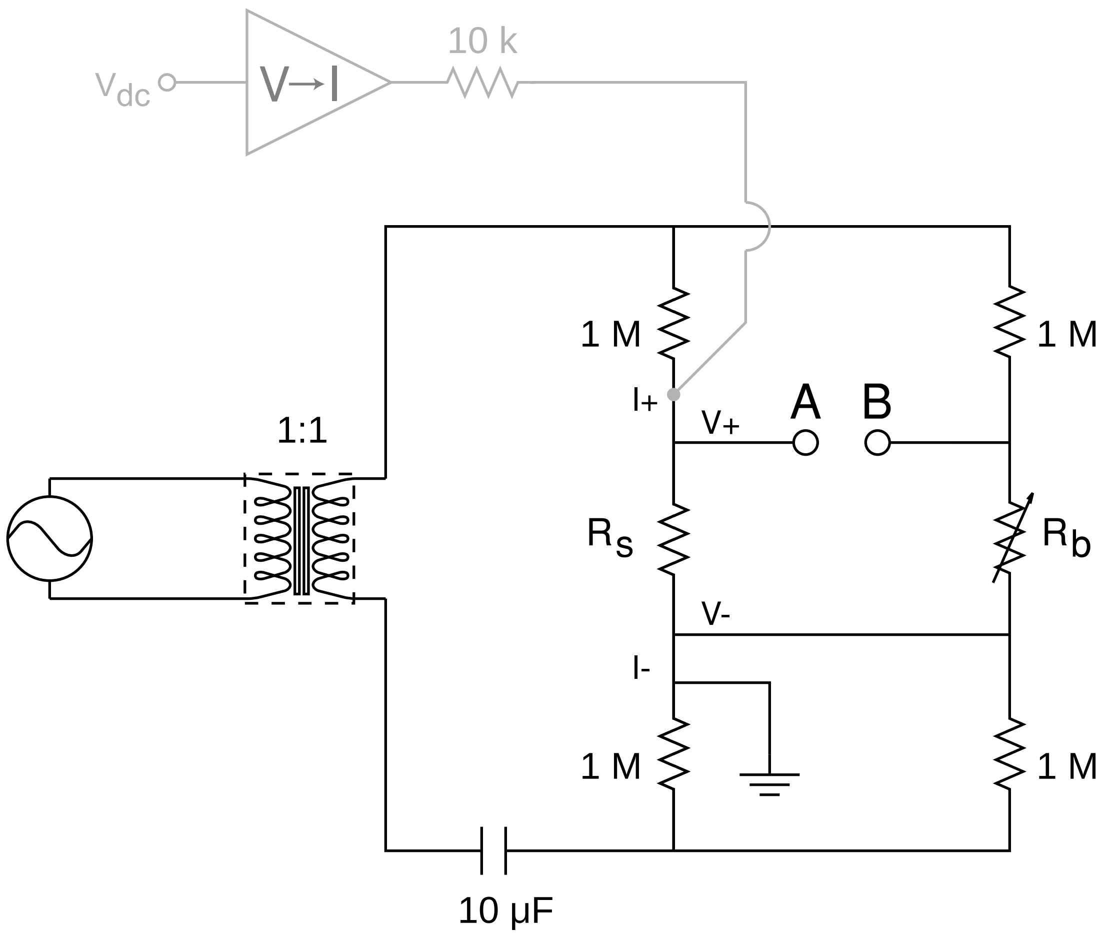

Figure 4.7: General ac resistance bridge measurement schematic. The input oscillator voltage taken from the lock-in amplifier is fine-tuned with a voltage divider inside the bridge box (not shown). The sample is represented by R_s and the decade resistor by R_b. dV/dI measurements are easily configured by adding a dc current at the I_+ probe *(shown in grey).* The sample grounding may be placed at any of the $V_\pm$, $I_\pm$ probes for resistance measurements, but must be placed at I_- for dV/dI measurements.

material	ρl [$10^{-6}\mu\Omega\cdot$cm^2]	$v_F[10^8$ cm/s]
Ni	15.0 [92]	~1.37 [93]
Au	8.45 [17]	1.40 [17]
Al	3.20 [94]	2.0 [17]

Table 4.1: Parameters used for calculating the diffusion constant D. The Fermi velocity listed for Ni should only be considered an estimate since it is based on the free electron model. Since Ni is a transition metal with hybridized *sd* bands a more accurate value for v_F is difficult to obtain. References for all numbers are denoted in brackets.

transition and approach zero at low temperatures. The technique described below is used only to measure our highest resistance FS samples (~1 MΩ).

We measure the differential conductance (dI/dV) by voltage-biasing the sample (with both dc and ac voltages) using a 100 kΩ:10 Ω voltage divider and measuring the resulting ac current response with an Ithaco 1211 current preamplifier[37] (see Figure 4.8). The dc and ac voltages are supplied by the voltage synthesizer (described above) and the lock-in amplifier's oscillator and are summed prior to biasing the divider. The current preamp signal is directed to a PAR 116/PAR 124 preamp/lock-in amplifier and is phased with respect to the excitation voltage at the top of R_s. The differential conductance is then determined by the current response divided by the excitation voltage. As in the dV/dI measurements, the voltage bias may be ramped using the voltage synthesizer and, similarly, it is important to gauge the level of heating due to the applied voltage, especially since the conductance may change by orders of magnitude in many measurements.

4.3 Sample characterization

4.3.1 Physical parameters

The devices in this study are all fabricated from films 300–600 Å thick with lateral dimensions not smaller than 600 Å. Since the elastic mean free path l is much smaller, we can consider electronic diffusion to be three dimensional in these systems, with a diffusion constant $D = \frac{1}{3}v_F l$ (where v_F is the Fermi velocity of the

[37] Ithaco 1211, Ithaco, Inc., Ithaca, NY

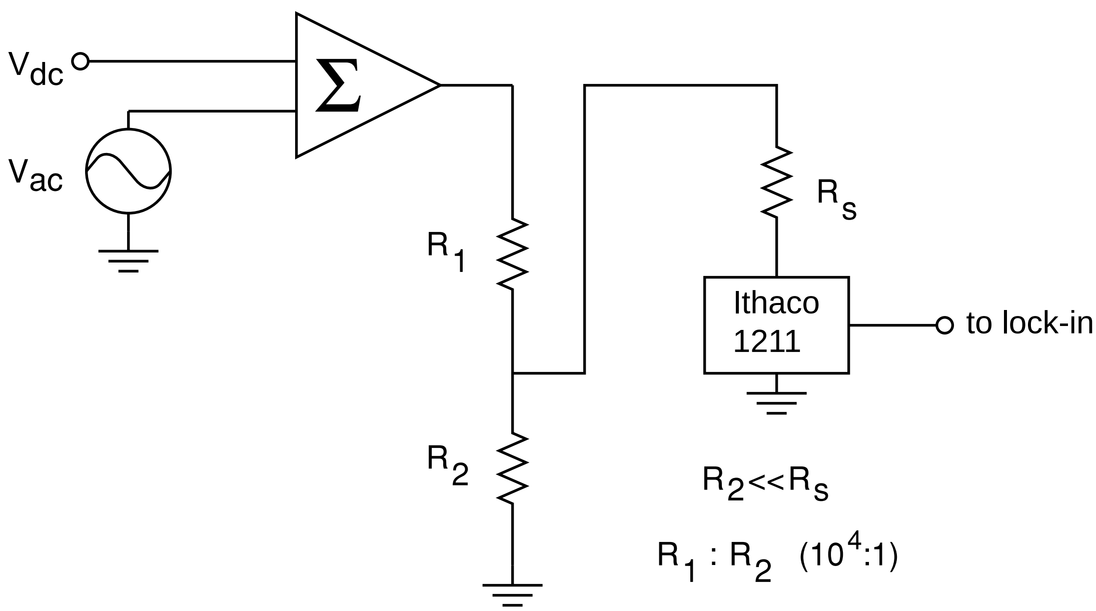

Figure 4.8: Differential conductance measurement (dI/dV). The sample R_s is voltage biased with a 10^4:1 voltage divider, while the current through R_s is sent through an Ithaco 1211 preamplifier which is connected to a lock-in amplifier.

conduction electrons). D is a useful parameter in estimating various mesoscopic lengths ($l_\varphi, l_T,$ *etc.*) since these all vary as $\sim \sqrt{D}$. In this work, we calculate D using known values of ρl from the literature (see Table 4.1) with resistivity ρ determined by the experimental sheet resistance ($R_\Box \equiv R(w/L)$) and the relation $\rho[\mu\Omega{\cdot}\text{cm}] = R_\Box[\Omega]\times\text{thickness[nm]}/10$.

Chapter 5

EXPERIMENT: SINGLE FERROMAGNETIC ELEMENTS

When we first considered studying ferromagnetic heterostructures and spin transport phenomena, it was clear that there was still much to be understood even in homogeneous ferromagnetic transport alone. As noted in Section 2.1.3, there was scant evidence for phase-coherent transport on conventional submicron length scales in ferromagnetic devices, and magnetoresistance in narrow Ni [95] wires suggested novel scattering mechanisms that had not been investigated seriously since its initial observation. In addition to this, intrinsic domain wall resistivity and its possible relationship to giant magnetoresistance mechanisms [55, 56] was beginning to gain considerable theoretical and experimental interest [96,97]. Ultimately, though, our initial motivation was simple: we needed to understand the transport in single ferromagnetic elements completely *prior* to attempting to understand transport in heterostructures which may be comprised of many of these elements.

In this chapter, we will examine our experimental studies of electronic transport in single ferromagnetic elements, paying particular attention to unusual properties and difficulties particular to mesoscale ferromagnetic devices. We will proceed in roughly chronological order, first studying the effect of AMR in single submicron ferromagnetic particles. Following this, we discuss antisymmetries due to our probe geometry, then proceed to the novel observation of conductance fluctuations in ferromagnets at low temperatures.

5.1 Sample design

5.1.1 The ellipse geometry

Our ferromagnetic elements are comprised of 30 nm thick submicron polycrystalline Ni ellipses on oxidized Si substrates patterned by e-beam lithography and deposited by e-gun deposition (see Section 4.1 for fabrication details). Rather than co-fabricate electrical probes in the same lithography step (which would then also be made of Ni), we choose to pattern a separate 60 nm thick Au layer for the probes (see Figure 5.1). The nonmagnetic Au probes are essential to this work since they simplify the magnetic structure near the Ni ellipses considerably, ensuring that magnetotransport measurements are not affected by possible domain structure that would be present at low fields. This need for isolating the magnetic structure had been ignored in previous experiments by another group affecting the magnetization distribution considerably [98]. Unfortunately, the Au layer not only represents an additional step in the fabrication, but also a difficult fine alignment step requiring sub-100 nm alignment methods not detailed in this work.

The choice of elliptical shape is not arbitrary since a central consideration in designing ferromagnetic heterostructures is the desire for a controllable magnetic structure. In most cases, this means a monodomain structure with clean magnetization switching properties. Unfortunately, to accomplish this requires a reduction in dimension so that the shape anisotropy energy dominates the magnetization direction [24]. Earlier microbridge SQUID magnetization measurements by Wernsdorfer *et al.* [99] showed that such properties were exhibited by 30 nm thick submicron-scale elliptical particles (see Figure 5.2). As we shall show, our transport measurements reflect this same behavior, and this geometry has proven to be a robust design for many of our ferromagnetic heterostructure devices.

5.1.2 "Quasi" four probe geometry

The Au leads have been patterned such that they extend across the ellipse along the minor axis direction. A four probe measurement performed as indicated in Fig. 5.1(c) would then measure the Au/Ni contacts in series with the Ni particle. In this sense, it is only a "quasi" four probe measurement, however, co-fabricated Au/Ni junctions indicate that this contribution is small and there is no magnetoresistance associated with these interfaces.

5.2 Anisotropic magnetoresistance in low fields

Figure 5.3(a) shows a typical low-field parallel magnetoresistance (MR) trace taken at $T = 1.5$ K in a 120 nm$\times$240 nm elliptical particle. Although we show only the MR for ± 1000 G in this figure, the magnetic field is really swept between ± 3000 G at a constant rate of less than 2 G/s.[1] Following the sweep from positive-to-negative magnetic field (dotted trace), one can see a gradual reduction in the resistance

[1]The high fields are to verify saturation of the particle magnetization, while the slow rate is for purposes of signal averaging in the resistance measurement.

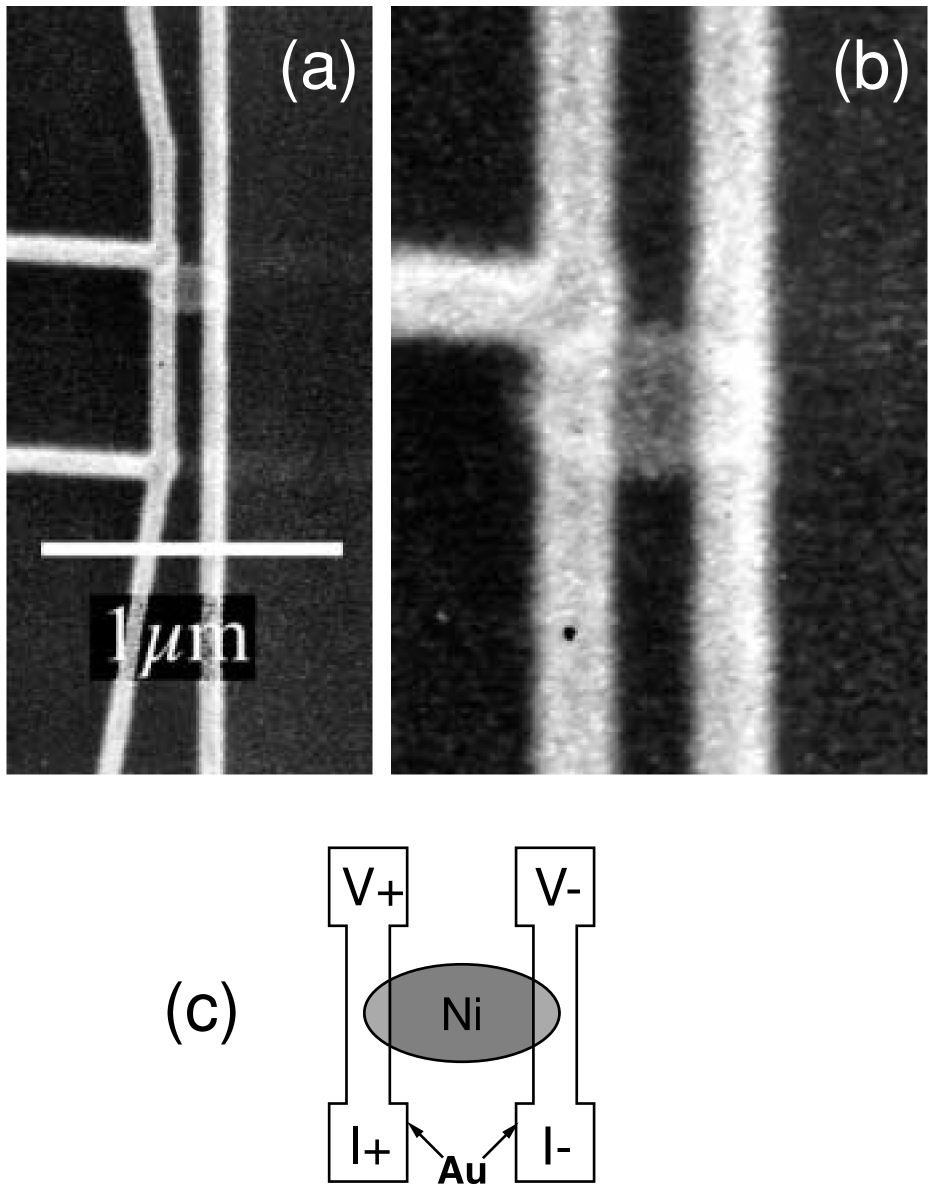

Figure 5.1: Single Ni ellipse measurement setup. (a) SEM image of 120 nm×240 nm Ni ellipse contacted by Au probe wires. (b) Enlarged view of ellipse geometry and contacts. (c) Schematic of four probe measurement.

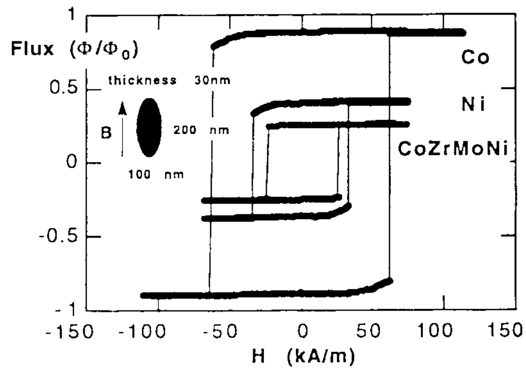

Figure 5.2: Microbridge SQUID magnetization measurements for submicron elliptical ferromagnets. *(Figure taken from Ref. [99].)*

which is terminated by a single discrete jump, while the negative-to-positive sweep (solid trace) shows similar behavior in the opposite direction. Before the jumps, the magnetoresistance is completely reversible while after the jumps, the traces then become reversible on a second curve which is nearly mirror symmetric with the original curve. In other samples, the magnetization reversal may occur in multiple steps. Figure 5.3(b) shows similar traces for a 220 nm$\times$640 nm elliptical particle in which this step-like transition occurs. The negative-to-positive field sweep (solid line) shows a single jump as before, but two distinct jumps are observed in the opposite sweep direction (dotted line). The single large jump in the negative-to-positive sweep indicates a complete switch in the magnetization direction occuring in one step, while the two distinct steps in the reverse direction may be due to an intermediate magnetization state that would be found in the presence of domain structure or magnetization pinning. Similar positive jumps in the magnetoresistance have also been seen in long wires by Hong and Giordano in studies of domain wall scattering [57], although, in that work there were a relatively large number of jumps, indicating the nucleation of many domain walls and giving a more continuous appearance to the dip structure. The relative scarcity of these multiple steps in our Ni ellipses is an indication of the strength of the shape anisotropy in dominating the magnetization and excluding multiple domain states at remanence.

These results above demonstrate that is possible to infer the magnetic state

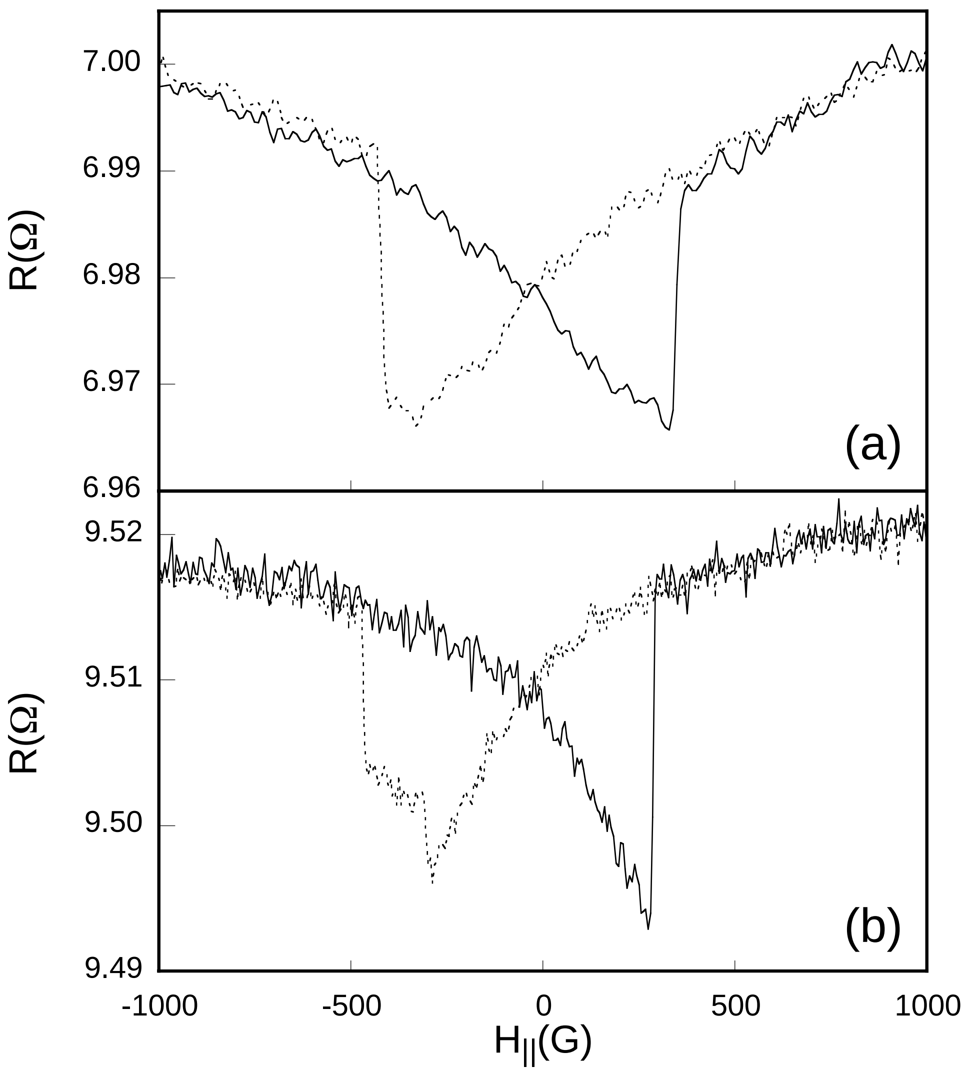

Figure 5.3: Parallel field magnetoresistance traces of Ni ellipses at $T = 1.5$ K. (a) 120 nm×240 nm Ni ellipse. (b) 220 nm×640 nm ellipse. The solid traces indicate a positive sweep direction, while dotted traces indicate the reverse.

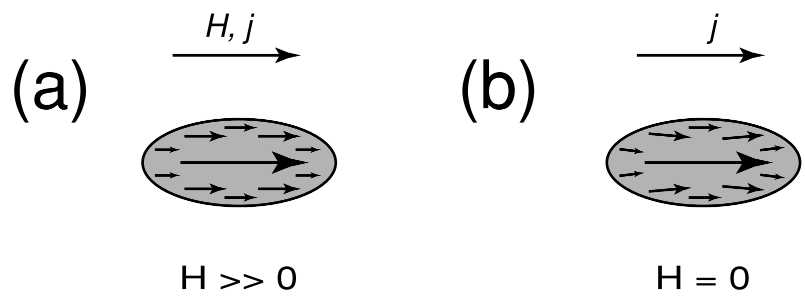

Figure 5.4: Schematic representation of the magnetic relaxation process

of a single-domain particle by measuring its MR. In order to do this, one needs to understand the mechanism which gives rise to the magnetoresistance. While Hong and Giordano [95] attributed similar positive magnetoresistances in long, narrow Ni wires to electron-magnon scattering, we find that our MR traces are more easily explained by a simple anisotropic magnetoresistance (AMR) [19] model (see Section 2.1.1). In our devices the majority of the current is directed along the major axis, which coincides with the easy axis of magnetization. Therefore, application of a strong magnetic field parallel to this axis saturates the resistance to its $R_{\parallel}$ value. As the external field is reduced to zero, this magnetization has a tendency to "relax" into a state with a smaller net magnetic moment along the easy axis due to demagnetization fields which arise from the shape of the element.[2]. In order to relax, the magnetization must begin to deviate from parallel alignment, away from the current path, providing a $R_{\perp}$ contribution to the resistance. This is depicted in depicted in Figure 5.4. As we have noted in Chapter 2, $R_{\perp} < R_{\parallel}$, so this magnetic relaxation will always be accompanied by a reduction in the resistance. With this picture, it then becomes possible to estimate the relative magnetization of these micromagnetic particles using the transport.

In Figure 5.5(a) we plot the MR for both parallel and perpendicular (in-plane)

---

[2]Although ellipsoids of revolution are known to have a theoretical uniform demagnetization field, $-4\pi DM$ [24], our elements are really "elliptical platelets," with a uniform thickness. This nonideal geometry should manifest itself in deviations in the demagnetization field from uniformity. We note in passing that an infinite cylinder is a limiting form of the ellipsoid of revolution, but the long wires studied in Ref. [95] were not ideal cylinders, hence the magnetic relaxation mechanism we propose would be valid in that experiment as well

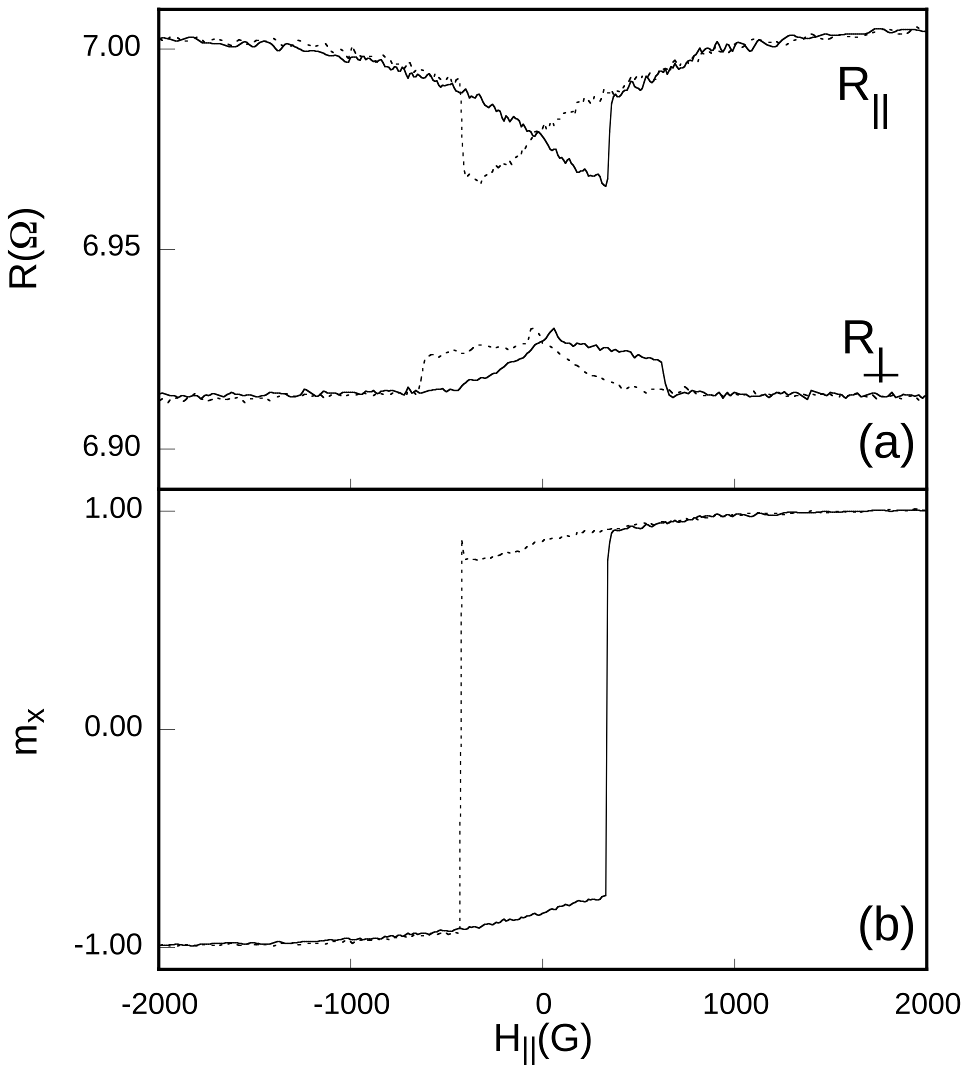

Figure 5.5: (a) Parallel and perpendicular magnetoresistances of a single Ni ellipse and (b) the inferred longitudinal magnetization from the parallel field MR. The solid traces indicate a positive sweep direction, while dotted traces indicate the reverse.

applied fields for the particle of Fig. 5.3. It is clear from the perpendicular MR that the resistance $R_\perp$ is smaller than $R_\parallel$ and already, we can see that the deviations from these two values always point to an intermediate value. This is in strong support of the picture outlined in the previous paragraph, since our essential argument is that the MR is dominated by changes in the magnetization through the AMR effect and all resistance values must correspondingly fall within the range, $R_\perp < R(H) < R_\parallel$.

Since the overall Lorentz MR slope is very low, we can estimate the in-plane AMR ratio using the saturated resistance values from the perpendicular and parallel MRs, arriving at $\Gamma_{AMR} = 1.4\%$ (see Eqn. 2.7 for definition).[3] More importantly, knowledge of $R_\perp$ and $R_\parallel$ allow us to determine the dependence of the resistance as a function of the magnetization direction (characterized by an angle θ referenced to the major axis). If we approximate a uniformly rotating magnetization (in-plane) as pictured in Figure 5.6, we can rewrite the $\cos^2\theta$ term of Eqn. 2.8 in terms of the normalized magnetization component m_x along the current path/major axis, *i.e.*,

$$R(\theta) = R_\perp + (R_\parallel - R_\perp)cos^2\theta, \tag{5.1}$$

becomes

$$R(H) = R_\perp + (R_\parallel - R_\perp)m_x^2(H). \tag{5.2}$$

We can now compactly express the rotated magnetization in terms of the magnetoresistance,

$$|m_x(H)| = \left(\frac{R(H) - R_\perp}{\Delta R_{AMR}}\right)^{\frac{1}{2}}, \tag{5.3}$$

with $\Delta R_{AMR} \equiv R_\parallel - R_\perp$ as usual.

Using this equation, hysteresis loops of the normalized magnetization projection may be reconstructed from the resistance, inserting appropriate signs at the coercive fields. The result is plotted in Fig. 5.5(b). Immediately we notice that the loop is nominally square, agreeing qualitatively with the observations of Wernsdorfer *et al.* (see Fig. 5.2), although our loop shows a stronger relaxation of the magnetization in low fields with $m_x \sim 0.85$ at zero applied field. In the spirit of the coherent rotation approximation such remanent values would imply that the

[3]This value is smaller than bulk values reported in the literature [19], but in agreement with expectations based on the size-dependence of the AMR [32, 33].

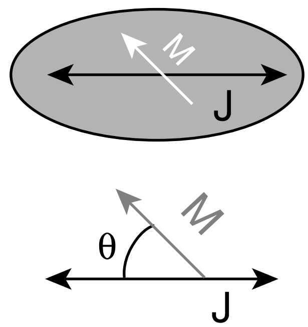

Figure 5.6: Simplified uniform rotation approximation used in determining $m_x(H_\parallel)$. The schematic shows a uniform magnetization distribution rotating with respect to the current path/major axis.

magnetization rotates 20–30° for the majority of our single domain particles. This value is certainly much larger than any possible misalignment in the applied field, and physically such a remanent rotation is unlikely. However, as we have noted, a more accurate model would show that the remanent magnetization distribution *should not* be uniform since demagnetization fields from the constrained geometry are likely to cant the magnetization near the edges and surfaces. In devices of this scale, the surface/volume ratio is much higher and the surface can contribute substantially to the resistance. For instance, to arrive at the remanent magnetization above, it is necessary to rotate only a few surface monolayers perpendicular to the major axis. Additionally, if the grain size is comparable to the dimensions of the magnet, the polycrystalline approximation begins to fail and crystal anisotropy plays a larger role in deviating the magnetization from the major axis toward the crystal axes of the separate grains. At present, it is difficult to distinguish between these relaxation mechanisms, but the nonuniform demagnetizing field appears to be the simplest explanation. Since the magnetization deviations we are concerned with occur on length scales much smaller than current magnetic imaging technology can resolve, the least expensive route to verifying this would be to solve the micromagnetic problem analytically or numerically.

What is clear from the above results is that the correlation between magnetization direction and resistance is a promising tool for investigating micromagnetic problems. Previously, the methods for studying micromagnetic structures involved either SQUID or Hall magnetometry on large arrays of particles. While the microbridge SQUID magnetometry of Ref. [99] allows the measurement of single submicron ferromagnetic particles, it is limited to temperatures below the superconducting transition of the SQUID materials (typically Nb or Al). Alternatively, magnetoforce microscopy (MFM) may be used to study single submicron ferromagnets but it becomes technically very challenging at low temperatures, and the resolution is still insufficient to characterize the minor magnetization shifts that AMR is sensitive to. In comparison, AMR may be used as a robust magnetization probe over large temperature ranges with relative ease.

5.3 Probe switching symmetries

5.3.1 The symmetric component

What is not apparent from the low-field MRs presented so far, is the high-field saturation into a linear field dependence as well as the presence of an overall antisymmetric component. These aspects are more obvious in the high field MR shown in Figure 5.7, taken at $T = 10$ K. In Section 2.2 we found that the MR should support a symmetry in the switching of voltage and current probes, $R_{ij,kl}(H, M) = R_{kl,ij}(-H, -M)$ (Eqn. 2.18), where the first two indices represent the current probes and the last two the voltage probes. It follows then, that switching the current and voltage probes as prescribed should yield the reverse field dependence and, indeed, this is what we find. In Figure 5.8(a) we plot the negative-to-positive MR sweeps for the probe configurations $R_{12,43}$, $R_{43,21}$ and the extracted symmetric component $R_S = (R_{12,43} + R_{43,21})/2$ for the Ni particle of Fig. 5.7. In Fig. 5.8(b) we check the quality of this symmetry by taking the true antisymmetric component of R_S, *i.e.*, the residual asymmetry[4] $R_{res} = (R_S(H) - R_S(-H))/2$. R_{res} shows the strong agreement with Büttiker formula (Eqn. 2.18) for the regions where the field H and magnetization M have the same sign while also showing the invalidity of this symmetry for H and M of opposite sign, *i.e.*, below the coercive fields of the ferromagnet.[5] Returning to R_S, we observe a roughly linear

[4] In general, when checking the symmetry in some variable, it is advisable to check for offsets in the zero value by shifting the data in both directions and performing the antisymmetrization procedure repeatedly. This is especially important when there are sharp features in the data which can easily create spurious antisymmetries when the data is shifted.

[5] This symmetry is not so surprising considering that all of the (anti)symmetric components are extracted with respect to the applied field H and not the internal field $B = H + 4\pi(1 - D)M$.

dependence due to the Lorentz MR contribution, while the AMR dip is still intact.

5.3.2 The antisymmetric Hall contribution

In Figure 5.9(a) we plot the corresponding antisymmetric component $R_A = (R_{12,43} - R_{43,21})/2$. This component has a slope $|dR_A/dH_\parallel| = 1.17$ mΩ/T and should correspond with a Hall-type contribution to the resistance. At first glance, this seems unlikely since the current and the magnetization are primarily collinear in this geometry. However, as shown in Fig. 5.9(b), the current must enter the particle at some angle due to the geometry of the Au/Ni contacts, creating a Lorentz force which acts upon the charge carriers. As shown in the figure, the force acts in opposite directions at either end of the particle, which should yield twice the Hall contribution one would measure in an ordinary Hall bar. Recognizing this field dependence, one may attempt to estimate the internal magnetic field $B_{int} = 4\pi(1-D)M$ since the jump in the antisymmetric component corresponds to a full reversal of the magnetization. By this logic, the change in internal field should be $\Delta B = 2|B_{int}|$, and the jump in resistance should correspond with this field,

$$\Delta R_A = 2|B_{int}| \left| \frac{dR_A}{dH} \right| . \tag{5.4}$$

Alternatively, one can simply extrapolate the slopes of the antisymmetric slopes to $R_A = 0$ and take the difference in field values at those points as shown in Fig. 5.9(a). By either method, we arrive at a value B_{int} ~11.5 kG which is clearly much larger than the saturation magnetization field ~6.3 kG for Ni. So what is the cause of this discrepancy?

In addition to the ordinary Hall effect, in ferromagnets there is an additional antisymmetric component which is associated with the magnetization, such that the sum of contributions should read [18],

$$R_A \propto \rho_H B + \rho_M 4\pi M, \tag{5.5}$$

with the factor ρ_M denoting a new contribution which is often called the *anomalous*

This is the essential reason for modifying Eqn. 2.17 to include M (Eqn. 2.18). Here, it is then assumed that the saturated magnetizations are symmetric in field direction.

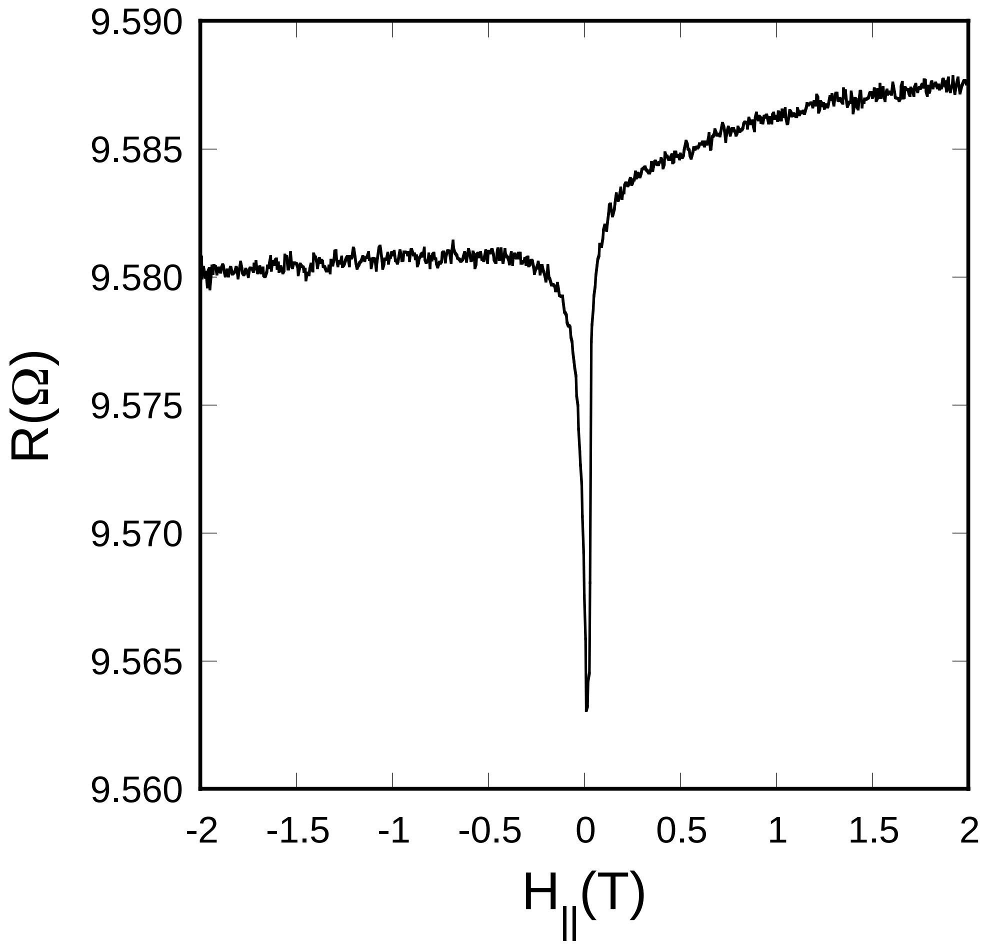

Figure 5.7: Single Ni particle parallel high field magnetoresistance with an overall antisymmetric component at T = 10 K. The Ni particle is 220 nm×640 nm in lateral dimension.

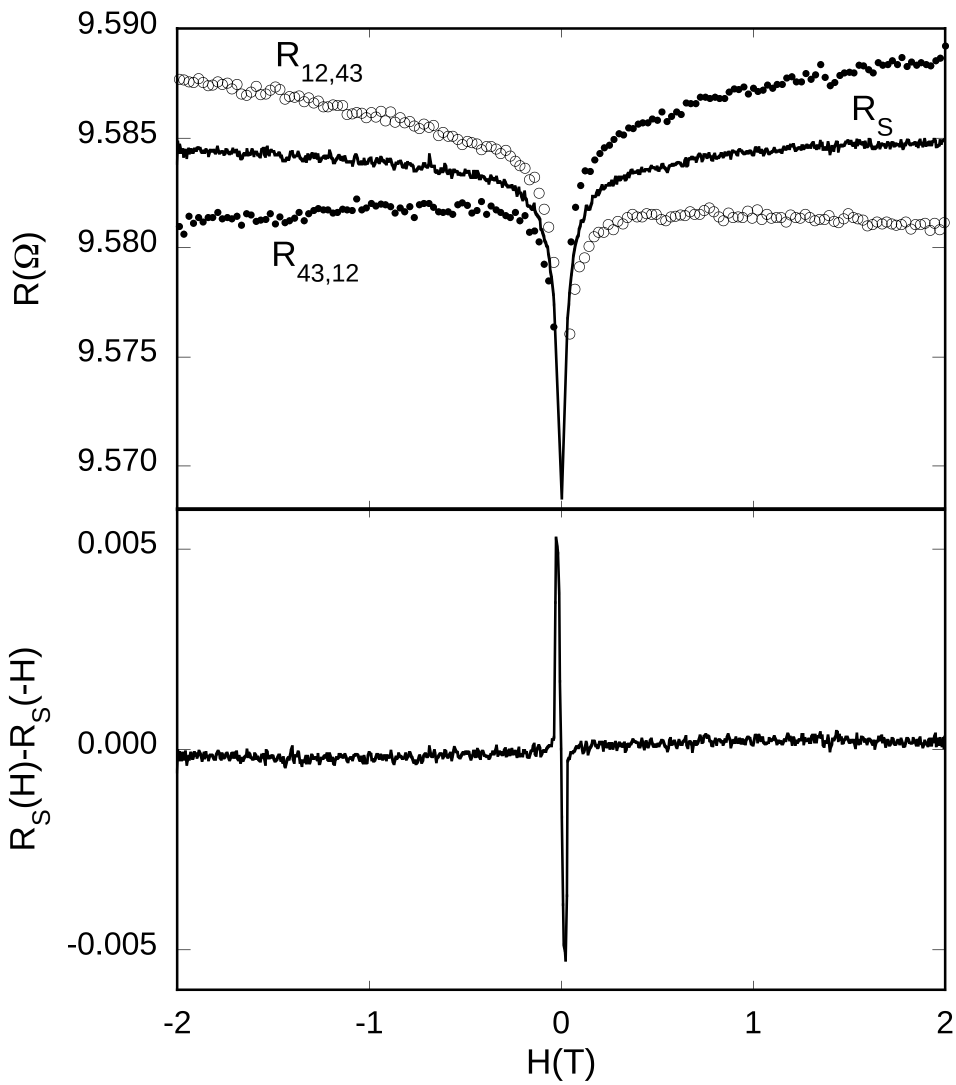

Figure 5.8: Symmetry of the magnetoresistance under switching of the current and voltage probes. (a) MRs of switched lead configurations as described in the text, including the extracted symmetric component R_S. (b) Residual antisymmetric component of extracted R_S, $R_{res} = (R_S(H) - R_S(-H))/2$, showing invalidity of probe-switching symmetry for $R_{ij,kl}(\pm H, \mp M)$ in ferromagnets.

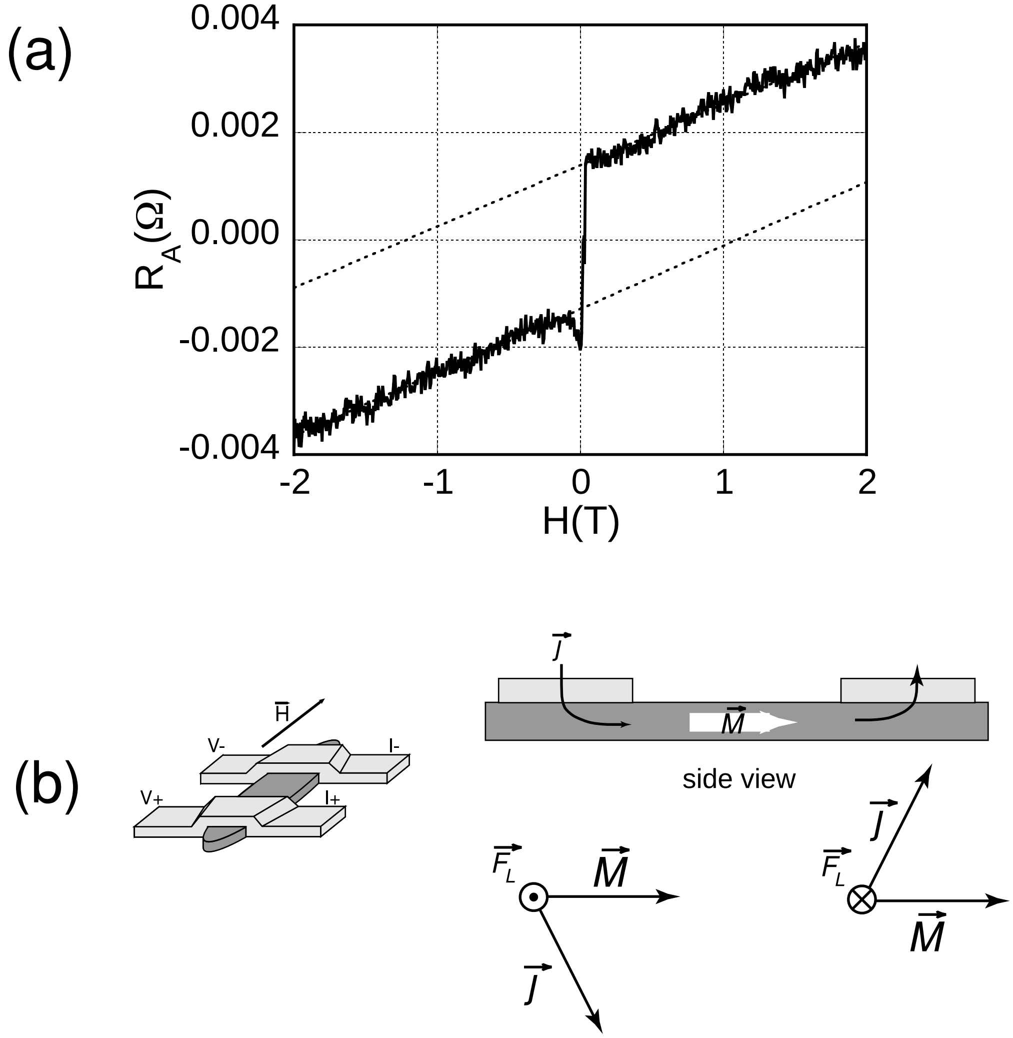

Figure 5.9: (a) Antisymmetric resistance extracted from the switched probe configurations of Fig. 5.8. Dashed lines are extrapolations to $R_A = 0$, giving the change in magnetic field when the magnetization reverses. (b) Side view of Au/Ni contact geometry. Current may enter the particle at an angle to the magnetization, subjecting charge carriers to Lorentz forces pointing in opposite directions at opposite ends of the particle.

Hall effect (AHE).[6] We can now write down the change in resistance,

$$\Delta R_A \propto (\rho_M + \rho_H(1 - D))8\pi M. \tag{5.6}$$

Of the parameters in this equation, we only know the slope $\propto \rho_H$ and the magnetization. In this example, the ρ_H term can only account for a change of 1.47 Ω out of a total of 2.66 Ω, with the remainder due to the AHE contribution. Although we did not do this, in principle ρ_H and ρ_M may be determined in a codeposited control sample with known demagnetization factors, yielding all the parameters necessary to determine the internal field if necessary.

5.4 Conductance fluctuations

When the particle from Fig. 5.7 is cooled even further, to $T = 1.5$ K, fluctuations in the resistance are observed which are reproducible as long as the temperature is kept low (see Figure 5.10(a), solid trace). After heating the sample to 10 K and cooling again to 1.5 K, the fluctuations change into a completely different pattern. These fluctuations are observed in all field directions, but we concentrate here on the parallel field MR.

In order to analyze these fluctuations it is necessary to subtract out the AMR background in a consistent way. It is possible to fit the background to some smooth function and extract the fluctuations, but a much simpler method is to subtract an MR taken at a higher temperature where the fluctuation phenomenon is smeared out. This is valid because the temperature range over which the AMR signal will change considerably is much larger [19] than the range over which the fluctuations die out and the AMR contribution should essentially be constant below $T \sim 10$ K. The results of this subtraction procedure are shown in Fig. 5.10(b), where we have first converted the resistances into conductances, and plotted the difference in units of e^2/h. The two traces shown were taken immediately after each other, illustrating the level of reproducibility of the fluctuations.[7] We find the rms value of the fluctuations to be $\sim$0.1 e^2/h, which is in agreement with theoretical estimates

[6] The most widely accepted theory for the AHE postulates a "side-jump" mechanism which shifts the position of an electron as it scatters in a ferromagnet. A review of the Hall effect in ferromagnets may be found in Ref. [100]

[7] Although the two traces are not exactly reproducible, the direct cross-correlation between them are reasonable considering that the temperature is relatively high (1.5 K) for this sort of experiment.

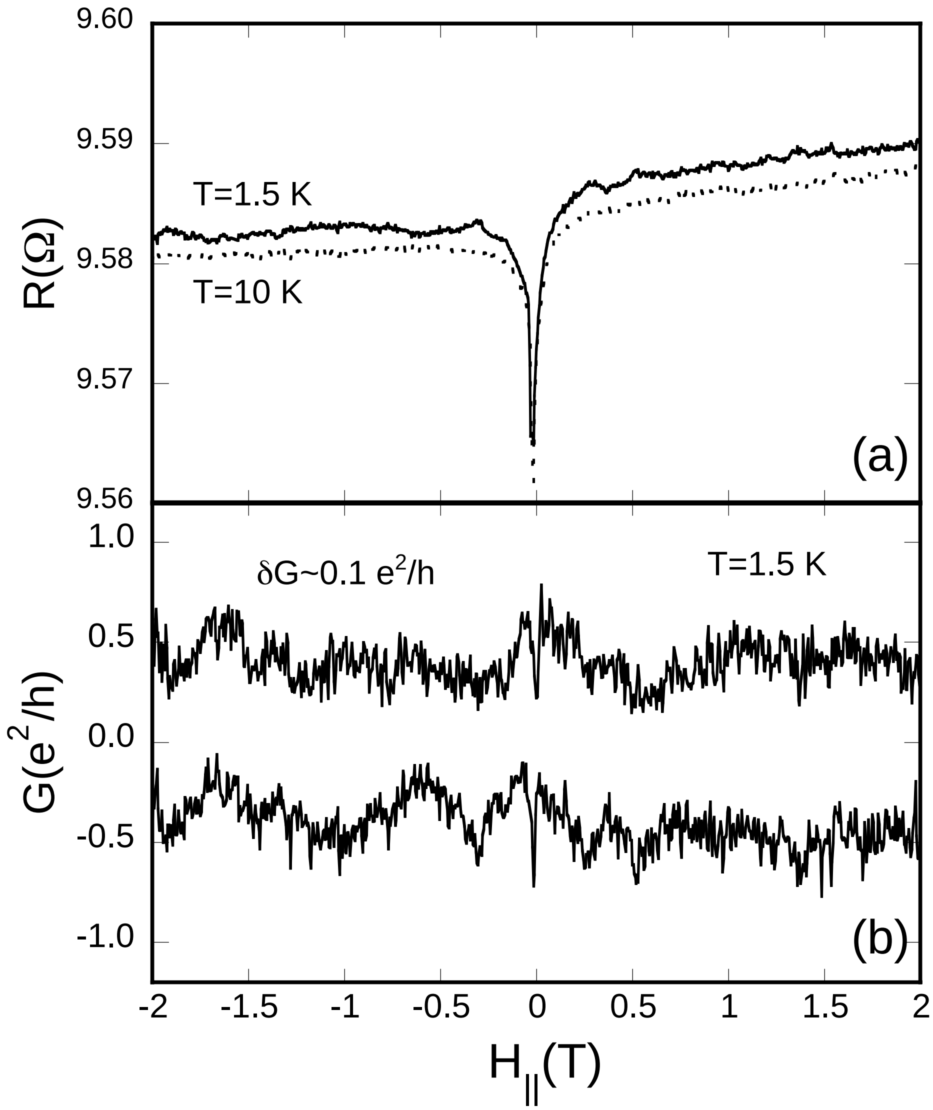

Figure 5.10: (a) Magnetoresistance fluctuations occur at $T = 1.5$ K (solid trace) and disappear at $T = 10$ K (dotted trace). (b) Subsequent magnetotransport traces plotted as the conductance after subtracting out the $T = 10$ K AMR background to show reproducibility.

of ~0.25 e^2/h for ferromagnetic metals (independent of field application direction) [101].

As encouraging as this result seems, we must be cautious in claiming that the fluctuations are entirely due to the Ni itself. Chandrasekhar *et al.* [53] pointed out the need to consider the electrical probes when analyzing weak localization (WL) and CF phenomena in samples with probe separations less than the coherence length l_φ. Intuitively, this is because conduction electrons can diffuse into the leads then back into the sample, accumulating phase shifts along these trajectories. Ultimately this means that what one measures in an quantum transport measurement includes segments of the leads extending l_φ from the sample. We performed WL measurements in long quasi-1D Au wires (which were codeposited with the Au probes used for measuring the Ni particles), and determined $l_\varphi \sim 1$ μm at 1.5 K. In the parallel field configuration, the phase coherent area of the Au probes would then be $A_\phi \sim 0.06$ μm^2, which would yield a correlation field for the fluctuations on the order of 0.05–0.10 T. If we estimate l_φ in our Ni to be larger than the Ni cross-sectional dimensions, w and t, then the relevant area in the correlation field would be the cross-sectional area itself, yielding an estimate of 0.5–0.6 T, a much larger scale for the fluctuations. One could directly compare those estimates with the data, but a more accurate method, which is also valid in homogeneous samples, is to take the difference in autocorrelation functions of the symmetric and antisymmetric components of the conductance [53]. This function, $F^{SA} = F^S - F^A$, should then yield the contribution of the sample alone. The results of this analysis for the fluctuations in Fig. 5.10 appear in Fig. 5.11(a)–(c).

It is apparent from Fig. 5.11 that the autocorrelation analysis is inconclusive. Although the function F^{SA} seems to be neglible near $\Delta B = 0$, it fluctuates considerably at higher values, as do the functions F^S and F^A. The reason for this is most likely the large scale of the fluctuations, since it is difficult to autocorrelate a function which varies on a scale comparable with its range. In our case, this would be a function of the maximum field range. If the Ni fluctuations are on the order of 0.5 T as estimated above, then a field range of ± 2 T is inadequate. At the moment, more measurements will need to be performed at higher fields to show that this is truly phase coherent transport within the Ni. In this case it may be suitable to fabricate the entire sample (including probes) in Ni since the magnetization will be saturated in the field regimes necessary to study the effect.

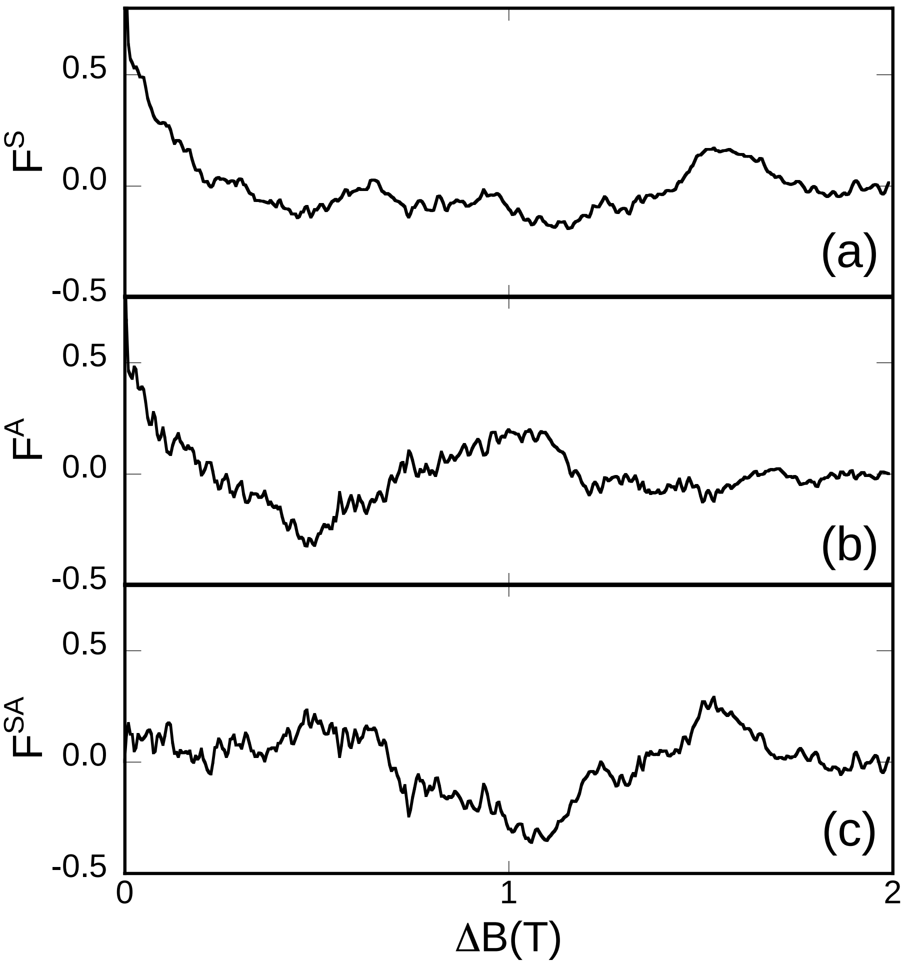

Figure 5.11: Normalized autocorrelation functions of the fluctuations in Fig. 5.10. (a) F^S, the autocorrelation function for the symmetric component. (b) F^A, the autocorrelation function for the antisymmetric component. (c) $F^{SA} = F^S - F^A$.

5.5 Summary

The single particle measurements presented above have not only demonstrated the feasibility of analyzing the magnetization using the electrical transport, but also the possibility of realistically subtracting out AMR contributions from the magnetoresistance so that we can study other aspects of transport in the MR. Lastly, we have utilized these methods to examine fluctuations in the magnetoresistance, providing early tentative evidence for quantum transport in a ferromagnet.

Chapter 6

EXPERIMENT: FERROMAGNET/SUPERCONDUCTOR HETEROSTRUCTURES

Recent theoretical interest concerning the possibility of observing the superconducting proximity effect in a ferromagnetic metal [10, 11, 102, 103] has been generated by a series of puzzling experiments [6–9] which all seem to indicate an influence of the superconductor on the transport properties of the ferromagnet. Specifically, the most dramatic effects were reported in mesoscale ferromagnet/superconductor (FS) structures studied by Petrashov *et al.* [6]. In that work, a large drop in resistance below the critical temperature T_c was found in clean contacts, while a rise in resistance occurred in higher interface resistance samples. In addition, the structure of the differential resistance vs. magnetic field phase diagram suggested an influence of the ferromagnetic element on the superconductor emphasizing the importance of magnetic field penetration due to the ferromagnet's field. The large drop in resistance was believed to be an indication of a "giant" proximity effect which extended an estimated 0.6–1.0 μm into the Ni. As mentioned previously (see Chapter 3), this value is orders of magnitude larger than the estimated length of superconducting correlations in the ferromagnet due to the strong exchange field (see Chapter 3). This length, $l_{ex} = \sqrt{\hbar D/k_B\Theta_C}$ (where Θ_C is the Curie temperature[1]), is estimated to be on the order of 2–20 nm, and any superconducting proximity effect should therefore manifest itself in a somewhat less dramatic effect than that seen in comparable NS heterostructures. At least one publication [103] has suggested a mechanism which extends l_{ex}, yet even those estimates fall very short from the value estimated by Petrashov *et al.* in their experiments [6]. Additionally, lack of evidence for such a long length scale has not been seen in high quality multilayer thin film studies [105, 106], casting a dubious light on the possibility of a true long range effect in relatively disordered ferromagnets.

In this chapter, we explore this issue experimentally, focusing on the effect of

[1] $\Theta_C = 631$ K in Ni [104]. In practice, it is often useful to convert this to an equivalent energy, $k_B\Theta_C = 54.4$ meV.

the FS interface in creating conditions similar to those studied in the Petrashov experiment. In addition to duplicating similar temperature dependent behavior in our devices (with an emphasis on probe placement), we also demonstrate evidence for spin dependent transport from F to S in the form of antisymmetries in the dV/dI measurements. Although we see little evidence for a proximity effect in our Al/Ni devices, the remaining problem of transport across the FS interface is interesting in itself and spawns a number of interesting questions for future experiments.

6.1 Experimental setup

6.1.1 Device design

One of our primary goals in beginning this experiment was to measure the response of a ferromagnet in contact with a superconductor without inclusion of the FS interface in series or in parallel. If we are to probe an effect estimated at a little over half of a micron, then this necessitates very narrow probes very close to the interface. In addition, we want a controllable magnetic state, preferably monodomain at remanence which can be monitored independently of the interface.

In Figure 6.1 we show our realization of such a device, utilizing our past experience in micromagnetic transport (see Chapters 2 and 5). The Ni particle is a 30 nm thick, 200 nm×500 nm ellipse fabricated using the methods outlined in Chapter 4. The ellipse is contacted on the top by four separate 50–60 nm thick Au probes (in contrast to the connected $I_{\pm}/V_{\pm}$ Au probes used in the single ferromagnetic particle measurements of Chapter 5) which can be configured in a true four probe measurement of the Ni ellipse alone. The Ni is then overlapped on one end by a four lead 50-60 nm thick Al wire which crosses the ellipse along its minor axis and is connected to Au probes less than two microns away.

Note that we have incorporated the elliptical shape of the experiments in Chapter 5, taking advantage of the two-state magnetization properties for the purposes of simplifying the magnetic field distribution in the vicinity of the interface. Correspondingly, all of the measurements shown which incorporate a magnetic field are performed with the field axis applied along the major/easy axis of the ellipses. This parallel field configuration has the added advantage that it couples the least flux into our thin Al films, raising the critical field considerably over the perpendicular critical field value.

(a)

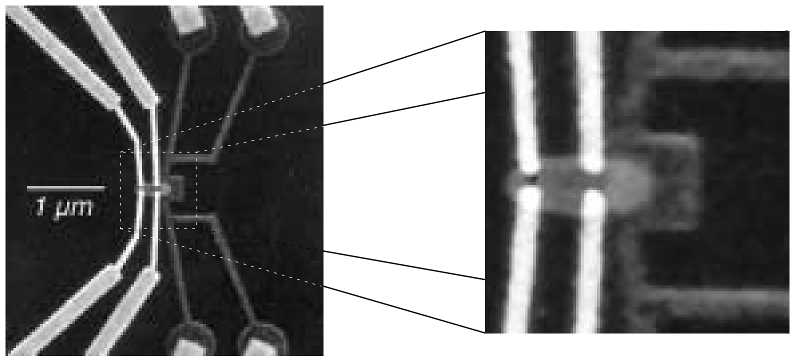

(b)

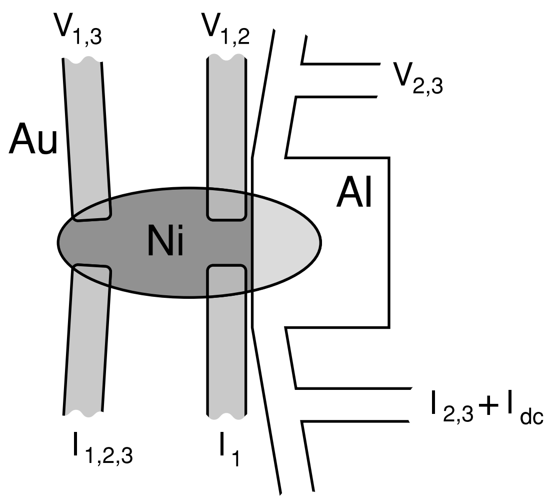

Figure 6.1: (a) Scanning electron micrograph of elliptical FS structure and (b) probe schematic for electrical measurements.

6.1.2 Probe configurations

The separation between the Au and Al probes near the Al/Ni (FS) interface is always verified in our scanning electron microscope prior to loading into the cryostat. This gap is usually between 20–50 nm in distance, such that any long-range proximity effect will be measurable in our probe configuration.

For the measurements presented here, we use three different probe configurations,[2] labeled “1” to “3” (see Fig. 6.1(b)):

- *Configuration 1* measures the four probe resistance of the Ni ellipse between Au probes along the major axis. Note that this is independent of the Al/Ni interface and can essentially measure any proximity effect that extends into the vicinity of the voltage probes V_1.

- *Configuration 2* measures the four probe Al/Ni interface resistance (which includes the short Ni gap between the Au and Al probes V_2.) This is independent of the behavior of the rest of Ni particle and allows a measurement of the interface transport directly.

- *Configuration 3* measures the four probe resistance of the Al/Ni interface in series with the Ni particle. This is essentially the same measurement as that performed in the Petrashov experiment [6].

In addition to these probe configurations we also can measure the resistance of the overlapping Au wire independently with four probes, labeling this quantity R_{Al}. Similarly, all other resistances measured will hereafter be indexed by their corresponding probe configuration, *i.e.*, R_1 will denote the resistance measured in configuration 1, *etc.*.

6.1.3 Additional geometries

In addition to the geometry presented in Fig. 6.1, we also measured other slightly different configurations as shown in Fig. 6.2(b) and (c). These variations were designed with the idea that by avoiding overlap with the ends of the Ni element, one could eliminate flux penetration into the Al that would otherwise occur. We

[2] Since there is no probe-switching symmetry applied in these experiments (as in Chapter 5), we forego the usual mesoscopic transport notation for four probe measurements ($R_{ij,kl}$) in favor of this simplified version which assumes the ± probe designations by context.

will return to this point in the discussion of our dV/dI measurements of the Al/Ni interface.

6.1.4 Measurement techniques

Here we utilize ac lock-in/bridge measurement techniques which have already been outlined in detail in Chapter 4. It important to note, however, that caution has been applied in choosing our excitation currents to avoid excessive self-heating. Accordingly, measurements which include the interface in the current path are performed with an excitation current of 10–50 nA, while the Ni particle measurements are taken with 100–500 nA.

6.1.5 Material parameters

In addition to the FS samples themselves, control samples of Ni wires, Al wires and Ni/Al interface samples are also fabricated simultaneously in order to characterize the material parameters of the films and interfaces. From low temperature measurements on these control samples, the resistivity of the Ni film was estimated to be ρ_{Ni} ~6.6 $\mu\Omega$·cm and that of the Al film ρ_{Al} ~8.4 $\mu\Omega$·cm, corresponding to electronic diffusion constants $D = (1/3)v_F l$ (where v_F is the Fermi velocity and l the elastic mean free path) of D_{Ni} ~104 cm^2/s and D_{Al} ~26 cm^2/s respectively (see Section 4.3.1).

The interface resistances were not always consistent due to contamination of the Al deposition sources from the TiB_2-BN crucible liners used. This resulted in comparatively low diffusion constants D_{Al} and various Al/Ni interface resistances (from ~19 Ω to 1.2 MΩ, all with similar interface areas). With these facts in mind we believe that the variation in Al/Ni interfaces resistances is probably due to diffusion of impurities to the interface and, consequently, the barriers are probably in the diffuse or "dirty" regime.

6.2 Temperature dependences

The various probe configurations listed above allow us to monitor many different elements of the system individually, and since the Ni particle is shorter than the estimated proximity length estimated by Petrashov *et al.* [6], the temperature dependence of the Ni particle resistance R_1 should be dramatic. However, as shown in Figure 6.3, the situation is quite different.

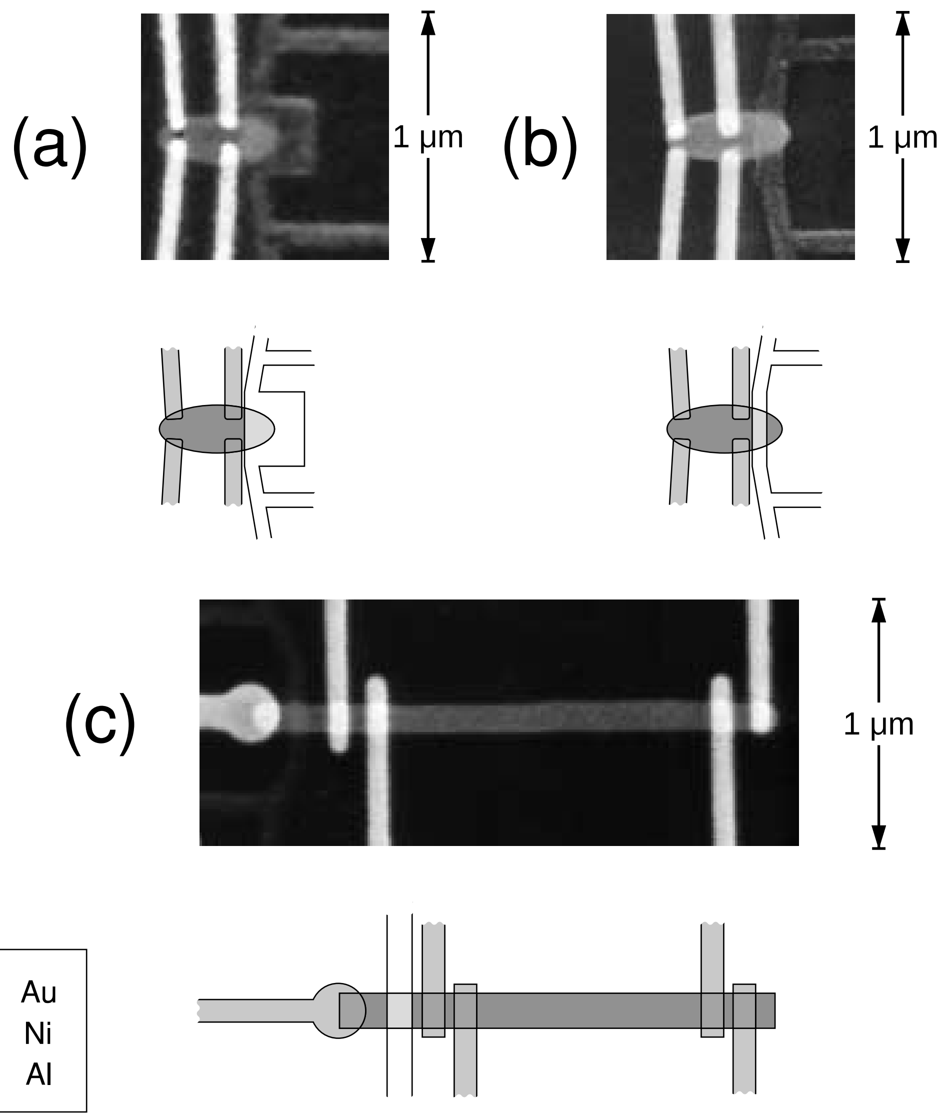

Figure 6.2: Variations on sample geometry. (a) Geometry A. Original geometry shown in previous figure. (b) Geometry B. Modified version of A, although Al does not overhang end of Ni. (c) Geometry C. Crossed wire geometry.

Figure 6.3 shows the temperature dependences of the three configurations listed above, as well as the resistance of the Al wire in contact with the Ni, all in zero applied magnetic field. In this case, we observe a normal state interface resistance $R_{2,n} = 23.8\ \Omega$ while the normal state Petrashov-type resistance R_3 yields a value approximately 2 Ω higher, corresponding to the addition of the Ni particle resistance to the interface resistance. In Fig. 6.3(a) it is apparent that these two resistances R_2 and R_3 have essentially the same temperature dependence, both showing a peak at the superconducting transition ($T_c \sim$1.4 K), decreasing as the temperature is lowered further, then beginning to rise again between 0.8 and 0.9 K, until they have almost reached their normal state values at our lowest temperature of $\sim$0.28 K. Already, in these measurements, we can notice that the lack of difference in the two temperature dependences $R_2(T)$ and $R_3(T)$ is a significant indication that there is no change in the Ni by itself. If we measure the Ni resistance R_1 simultaneously we can confirm this and the result is shown in Fig. 6.3(b). Essentially there is no temperature dependence in the Ni to within our measurement noise, implying that *there is no superconducting proximity effect within the Ni.* This same result was confirmed in all of our other devices over a large range of interface resistances.

Having established the absence of a proximity effect in the Ni, we can now discuss the physical sources for the temperature dependence of the interface resistance R_2.

The peak $R_{2,3}$ in Fig. 6.3(a) is characteristic of many mesoscopic NS devices in which the voltage probes lie within a charge imbalance length of the interface (see for example Ref. [86, 107]) and the potentials being probed are a mix of quasiparticle and Cooper pair potentials. Although the temperature dependence measurement occurs with zero voltage/current bias, the excitation current provides enough energy bias to exceed the negligible superconducting gap energy at T_c and inject quasiparticles into the Al. Since there can be a large difference in the quasiparticle potential (measured by normal probes) and Cooper pair potential (as measured by the superconducting probes), a large potential difference may be produced between normal and superconducting probes [108] resulting in the peak shown. This peak was seen in other similar devices of comparable interface resistances, but disappeared with slightly higher values of this parameter.

Figure 6.4 illustrates the temperature dependence for various resistance values. Except for the very highest resistance (1.23 MΩ), all of our temperature dependences showed a reentrant behavior similar to the reentrant proximity effect seen in many mesoscopic NS devices (see for example Ref. [63]). However, since we know

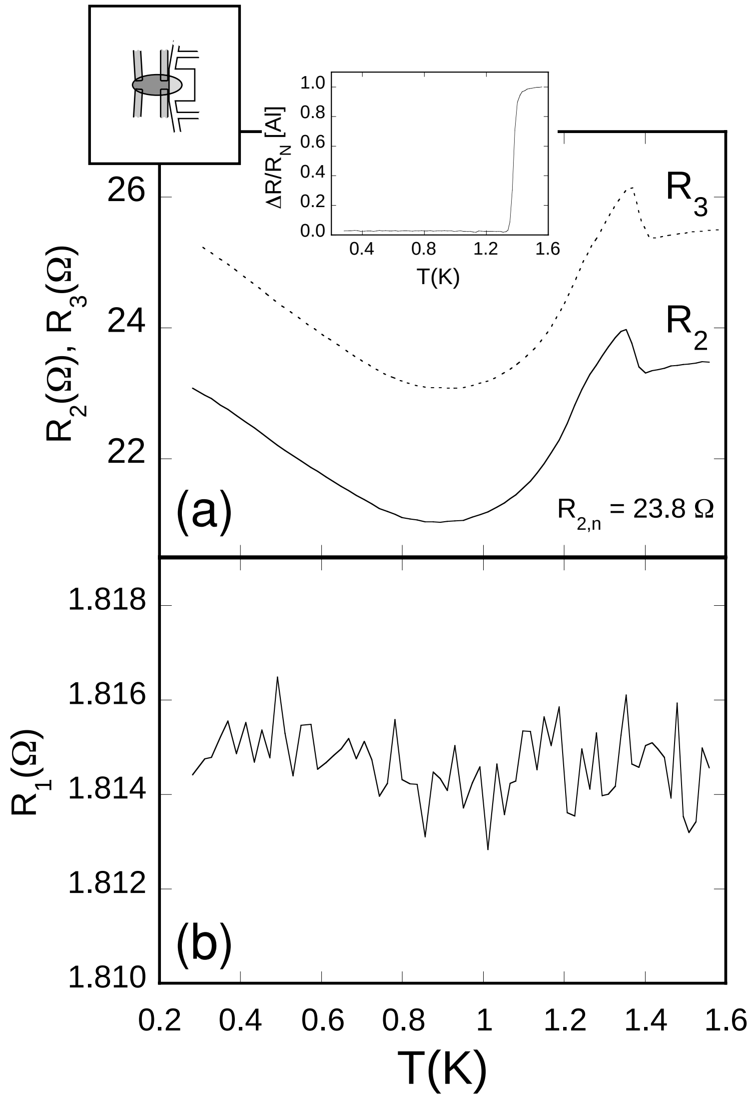

Figure 6.3: Al/Ni, Al and Ni temperature dependences. (a) The Al/Ni interface resistance, $R_2 = 23.8\ \Omega$, and the interface resistance and Ni ellipse in series, R_3. (a, inset) The resistance of the overlapping Al wire, R_{Al}. (b) the resistance of the Ni ellipse, R_1.

that such an effect is negligible in the Ni, we can attribute the entire dependence to sub-gap transmission processes, *i.e.*, Andreev reflection at the interface. In doing so, we return to the BTK picture of transport [69] outlined in Chapter 3. In the 1.23 MΩ sample for example, we see a resistance that increases very rapidly below T_c, indicating the vanishing probability of FS transmission as Andreev reflection is suppressed in the high barrier limit.

6.2.1 Multiple states

In many instances the interface resistance temperature dependences $R_2(T)$ showed multiple distinct states which could be seen in both temperature and magnetic field cycling (see Figure 6.5). The reasons for this are unknown currently, but we believe that a possible source could be the existence of either flux trapping in the Al probes or multiple screening states in the Al near the interface. Either phenomenon could alter the quasiparticle density of states close to the interface which could considerably alter the barrier transmission properties. In any case, the source seems to be metastable in the presence of small amounts of background noise, although this observation is only a qualitative observation and the overlapping Al wire was confirmed to remain in the superconducting state. For the discussion which follows we call the high resistance state, "state 1," and the low resistance state, "state 2."

6.2.2 BTK numerical fits to the temperature dependence

If the transport can be at least qualitatively described by a BTK-type model, can it be fit as such? To answer this, we fit the temperature dependence using a set of programs written by the author to originally calculate dV/dI curves following the BTK description. After modifying the BTK coefficients to account for the polarization (see Chapter 3), we attempted to fit the data. In doing so, however, we ran into a number of problems. First, the magnetic field near the interface is likely to be inhomogeneous on the scale of the coherence length (estimated to be 50–60 nm by a separate T_c vs. H measurement) due to the close proximity to the Ni. Second, it is unclear what this field should be in zero-applied field. Therefore, to fit the data at least three free parameters (the magnetic field H, the polarization P and the barrier height Z) were needed in most cases. To compound these problems, the critical field H_c was experimentally determined to be between 3000 and 4000 G, however this number should already include the field generated by the Ni itself, so in practice, it was necessary to have a fourth free parameter,

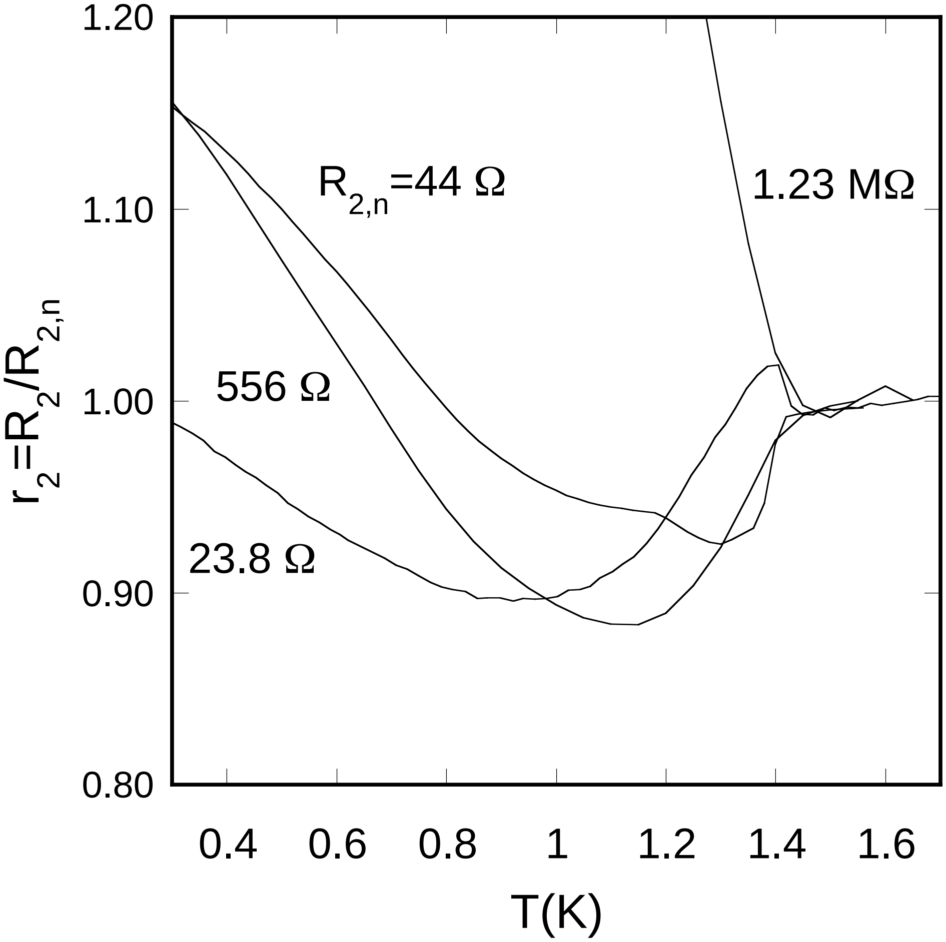

Figure 6.4: Normalized resistance vs. temperature for various interface resistances, R_2 =23.8 Ω to 1.23 MΩ. Measurements are performed in zero applied field.

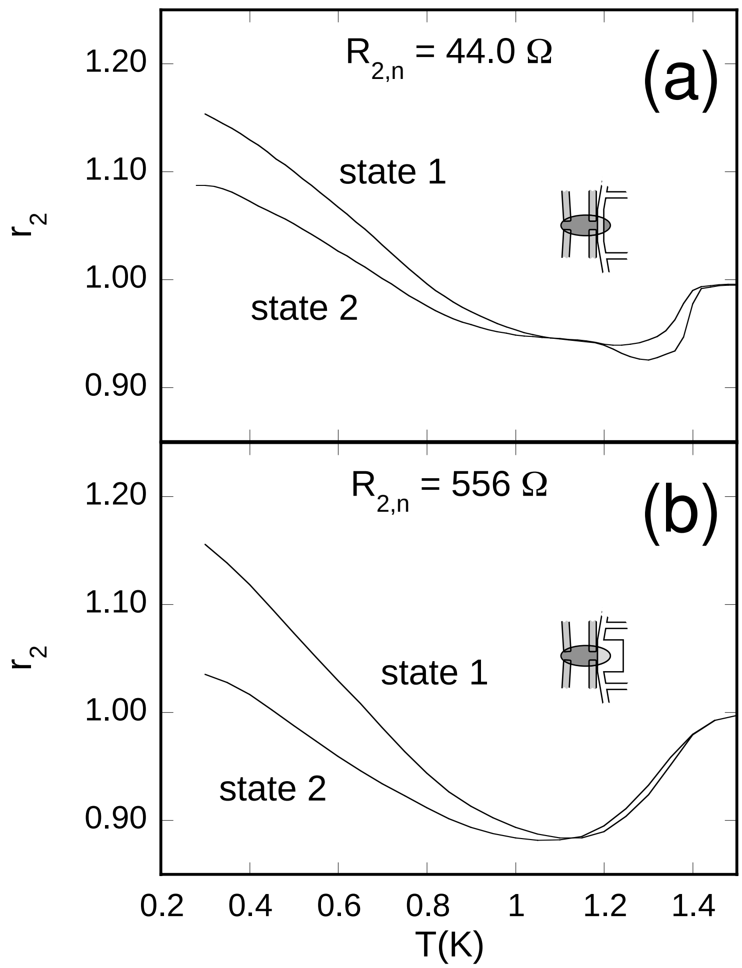

Figure 6.5: Multiple states in the temperature dependence $R(T)$. (insets) Schematics show device geometry.

sample parameters		free parameters			
Geometry	$R_{2,n}(\Omega)$	H(kG)	H_c(kG)	P%	Z
A	23.8	4.41	6.30*	29.9	0.38
B	44.0				
	(State 1)	3.13	8.48	31.5	0.45
	(State 2)	4.52	11.5	34.8	0.38
A	556				
	(State 1)	6.75	21.8	0.00	0.66
	(State 2)	4.71	15.5	21.1	0.47
C	1.23×10^6	0.26	20.6	28.3	2.07

Table 6.1: BTK fitting parameters for FS interface resistance temperature dependences shown in Fig. 6.6. *Fixed parameter in fit.

the field, in order to get anything that resembled a decent fit. For reference, in Table 6.1 we give the fitting parameters for the temperature dependences for four different samples. The results of these fits are shown in Figure 6.6.

Although many of the fits look reasonable, an examination of the table of parameters (Table 6.1) reveals a number of odd things. For the most part, the fitted fields H are all in the vicinity of 5 kG which seems to correspond reasonably well with the internal field from the magnetization of Ni, $4\pi M$ ~6.3 kG. The exception to this was the 1.23 MΩ sample, which was a crossed Al/Ni configuration (geometry C), yielding a field H ~260 G. However, anisotropic magnetoresistance (AMR) measurements (not shown) of the Ni in this geometry, demonstrated multidomain behavior at zero applied magnetic field. In this sense, the local magnetic field profile near the interface could be considerably attenuated in magnititude from the single domain particle case and a lower value of H would therefore be reasonable. When examining the critical fields though, they all seem quite high, mostly between 1 and 2 T, although, in principle, this is reasonable for short superconducting coherence lengths as in our case.

Additional examination of the fitting parameters reveals a systematic increase in Z with the interface resistance, although one would intuitively expect larger values for $R_{2,n}$ =556 Ω and 1.23 MΩ. However, the polarizations, with the exception of the 556 Ω interface (state 1), all yield values P = 20–35%, agreeing loosely with the accepted value for Ni of 23% from tunneling measurements [78]. What is also

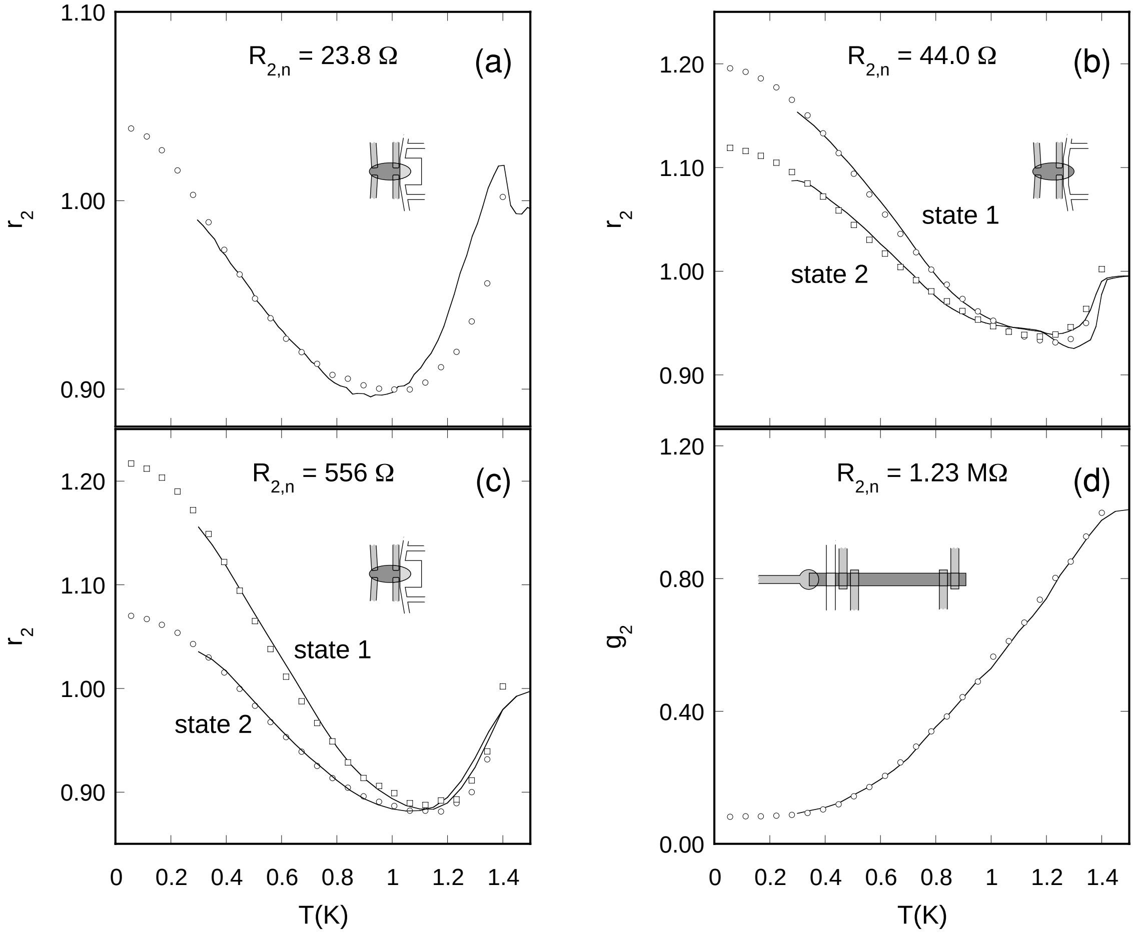

Figure 6.6: BTK fits to the temperature dependence of Fig. 6.4. Note that the 1.23 MΩ resistance has been presented as a normalized conductance. The fitting parameters can be found in Table 6.1. (insets) Schematics show device geometry.

interesting is the $P = 0$ result, since this seemed to be immune to any variations in the starting parameter values in the fitting routine and deviates so much from the rest of the polarization fits. Whether this has any fundamental physics behind it is debatable, and whether the fits themselves bear any strict correspondence to reality may be a matter of interpretation as well.

The BTK theory was developed assuming that the momenta served as good quantum numbers describing the quasiparticle states, but, as stated in the original paper [69], this may not be the case in dirty metals, and a rigorous correspondence with our system may be out of line. In this case, a more generalized and heavily abstracted approach based in a quasiclassical Green's function formalism[3] may be required. While the agreement of the polarization values with a standard (tunneling result) value is tantalizing, for now, we simply interpret the BTK fits as a qualitative tool in understanding the transport and nothing more.

6.3 Magnetic field dependence of the resistance

Figure 6.7 shows parallel field magnetoresistance traces for the Al wire, Ni particle and Al/Ni interface. In the Al/Ni interface resistance R_2, we observe sharp jumps at $\sim +350$ and -300 G (Fig. 6.7(a)), corresponding with the coercive (switching) fields of the Ni ellipse (Fig. 6.7(b)). This correspondence can only be explained by a strong dependence of R_2 on the local magnetic field, specifically, that generated by the Ni ellipse. This sensitivity of the FS transport to local magnetic field will be seen repeatedly in the discussion which follows.

6.4 The differential resistance dV_2/dI of the FS interface

Figure 6.8 shows the results of dV_2/dI measurements performed in the $R_{2,n}$=23.8 Ω sample in a series of magnetic fields applied along the major axis of the Ni ellipse. Upon first examination, one notices very sharp peaks at $\sim \pm 5.8$ μA. As mentioned earlier, similar peaks are seen in NS structures and are believed to be associated with charge imbalance effects [86, 107]. The rest of the structure is similar to what one would expect from the BTK model we examined earlier, displaying a reentrant behavior with increasing current bias, and perhaps this is not surprising given prior knowledge of the temperature dependence. What is curious, however, is the appearance of an antisymmetry in the dc current bias. This is most obvious in

[3]For a review of the basic techniques see Belzig *et al.* [109].

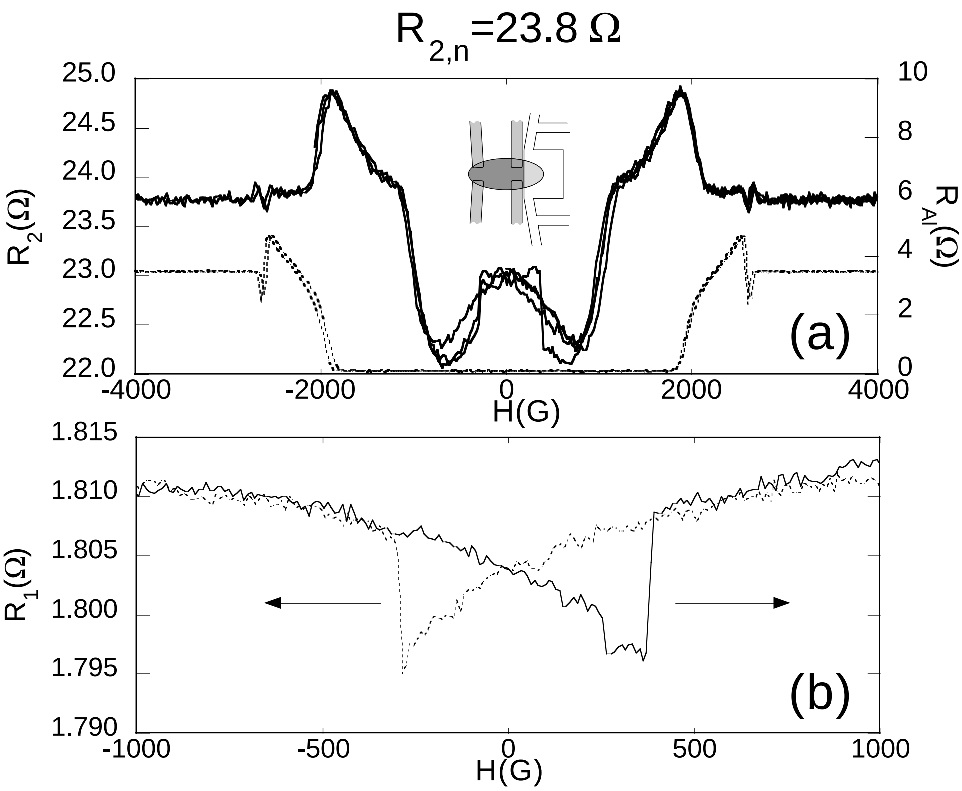

Figure 6.7: Al/Ni, Al and Ni magnetoresistance traces at $T = 0.3$ K. (a) The FS interface magnetoresistance (left axis, solid trace) and the corresponding Al magnetoresistance (right axis, dotted trace). (b) Ni AMR signal displaying usual single domain behavior. Arrows indicate sweep direction. (inset) Schematic shows device geometry.

the sharp $H = 0$ G trace in Fig. 6.8, but this antisymmetry is present at fields up the critical field, in traces where the charge imbalance peaks are not as sharp. In Fig. 6.9, we illustrate the antisymmetric component directly, for a dV_2/dI trace taken in an applied field of 600 G.

6.4.1 Possible sources for antisymmetry in dV_2/dI

One may point out that the presence of an antisymmetric component can be due to many factors, not the least of which is measurement error. It is possible, for instance, to get an antisymmetric component from fine structure, such as sharp peaks, from a poor choice of bin size in the averaging when taking the data. Such mistakes would be evident in correlated peak structure in the antisymmetric component and are usually noticed in the original trace as an obvious hysteresis or non-reproducibility in subsequent traces. Alternatively, one may have a maladjusted zero-point calibration in the voltage-to-current converter for the dc current bias, or even a bad zero-point in the preamp which monitors the current. A misalignment of this zero-point would then result in broad undulations in the antisymmetric component on the scale of the features in the original trace. We can see that such behavior is absent in the antisymmetric component in the example in Fig. 6.9 as there are large flat regions, with nonzero values clustered locally near the peak locations in the original dV_2/dI. The zero-points were also checked by shifting the traces a small amount in the positive and negative directions and repeating the antisymmetrization procedure.

Another source for antisymmetry in a dV/dI measurement is a possible thermopower contribution which has already been seen in experiments by Eom *et al.* in NS devices [80] and AuFe spin-glass wires [110]. In the NS experiments, it was found that the thermopower contributed an antisymmetric component to the dV/dI which had a characteristic sharp finite slope at the zero-crossing, with most of the structure confined to this region. We can see from Fig. 6.9(b) that a similar structure is clearly absent from our measurements.

After eliminating the sources outlined above, we conclude that the antisymmetric components are indeed real and that they may correspond to an actual transport mechanism.

Spin-polarized transport?

As shown in Chapter 3, even the application of a 1 kG field can be seen to Zeeman split the quasiparticle density of states, giving an antisymmetric contribution to

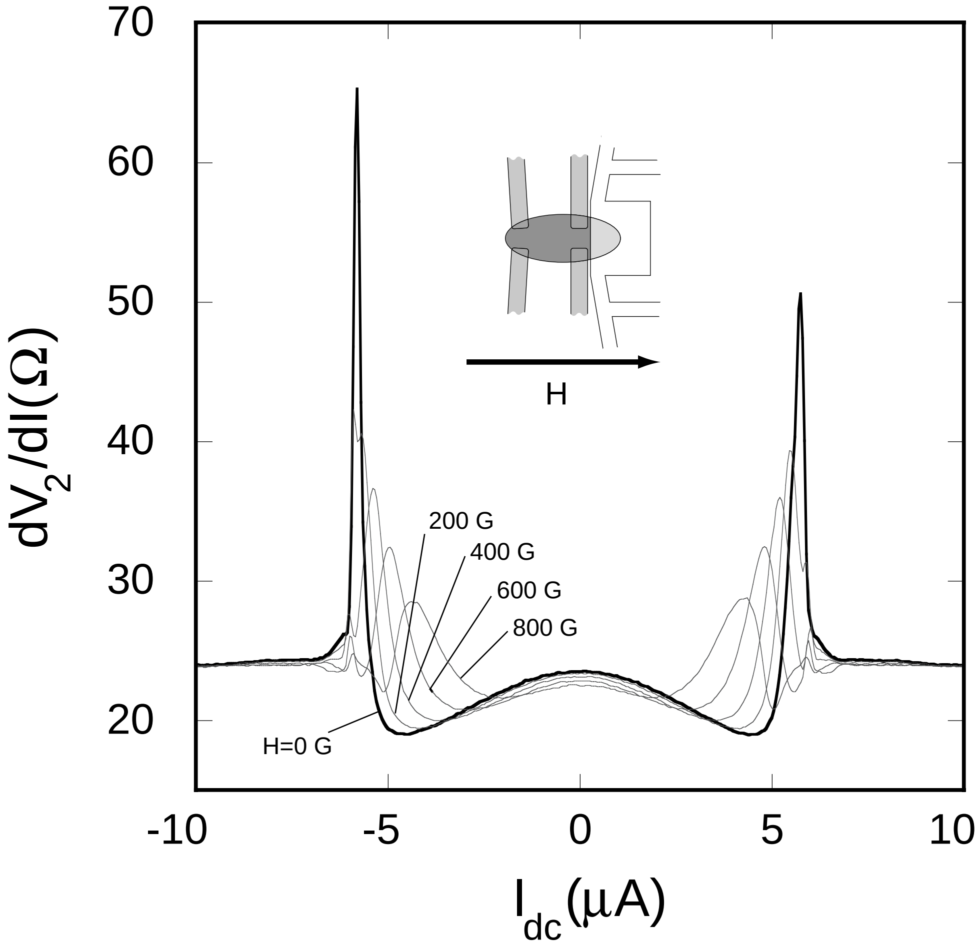

Figure 6.8: dV_2/dI measurements of the Al/Ni interface at $T = 0.3$ K in various applied fields applied along the major axis of the Ni ellipse. Antisymmetries are discernible in the peak structure at various magnetic fields (noted in figure). (inset) Schematic shows device geometry and field application direction.

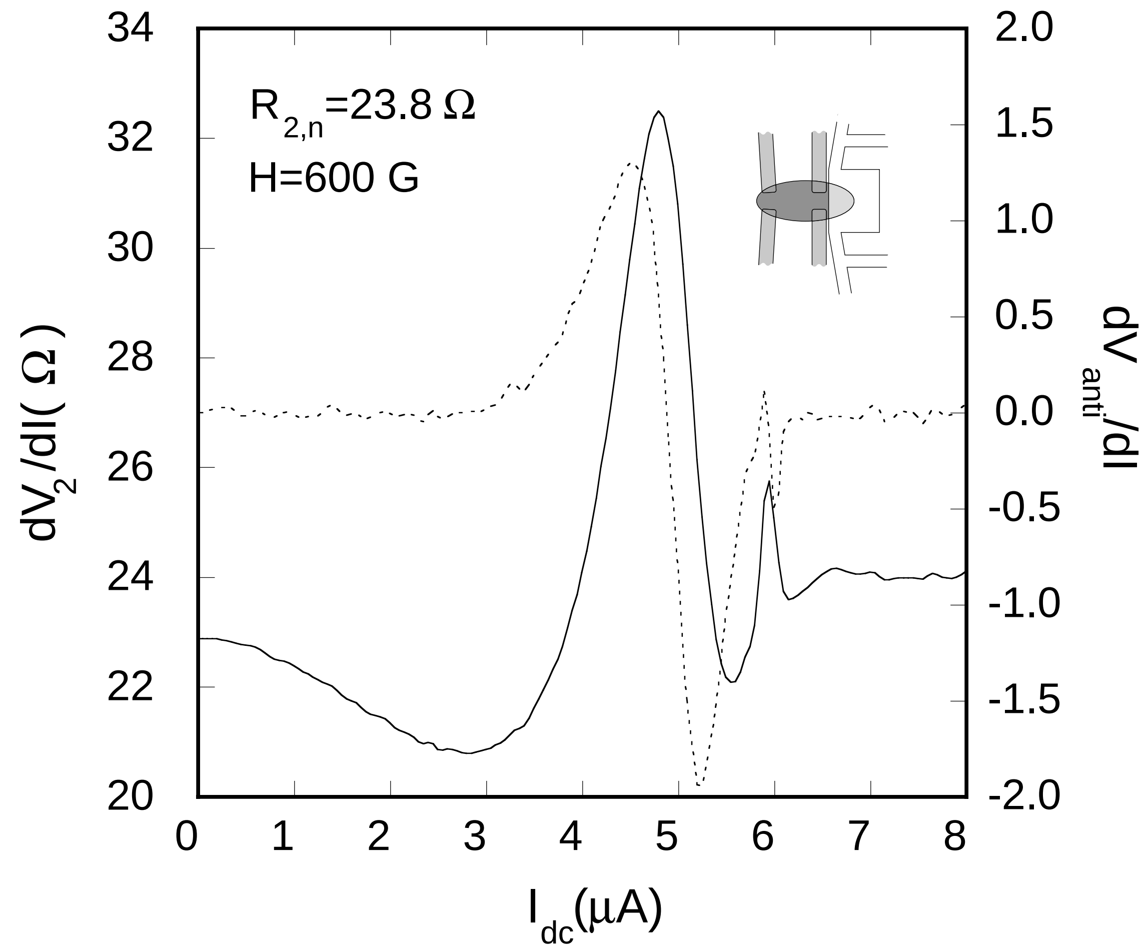

Figure 6.9: Comparison of Al/Ni dV_2/dI with its antisymmetric component ($R_{2,n} = 23.8\ \Omega$) at $T = 0.3$ K in an applied field of 600 G. (inset) Schematic shows device geometry.

the differential tunnel conductance between a ferromagnet and a superconductor (see Fig. 3.8). As suggested by Mélin [12], this effect may also be seen in the differential conductance of FS devices with arbitrarily strong barriers. To examine this possibility, we reversed the direction of the Ni ellipse magnetization with respect to the applied magnetic field and compared the results from this antiparallel state to its parallel counterpart. The results, shown in Figure 6.10, are intriguing.

In this example, we have ramped the magnetic field to a large negative field, saturating the magnetization of the Ni ellipse in this direction, and then ramped the field down to $H = +200$ G and persisted the field such that the magnetization remained negative. In this state the magnetization and the applied magnetic field are antiparallel ($m < 0$, $H > 0$). At this point we took the dV_2/dI trace shown in Fig. 6.10(a) (dashed trace). We then immediately ramped the field to +450 G, switching the magnetization to point along the applied field axis, then relaxed the field once more to +200 G. In this state both the magnetization and applied field are positive ($m > 0$, $H > 0$). In this configuration, we took the second trace shown in Fig. 6.10(a) (solid trace). Immediately, one can observe a difference in the peak locations, presumably because the local magnetic field profile has changed considerably. In the antiparallel configuration the local field is reduced from the value of the parallel configuration, suppressing the superconducting gap even less, thus bringing the peaks to higher values. What is more interesting in this example is that the behavior of the antisymmetric components (Fig. 6.10(b)). Along with the shift in peak structure, we also observe an apparent inversion of the peak/dip structure between the two configurations. Such an observation might be considered significant evidence that the antisymmetries observed are due to polarization of the electrons transmitted across the barrier. However, it should pointed out that the BTK fits shown earlier seemed to mostly yield magnetic fields of a few kG. But, if not taken literally, this may be not really much of an objection. Afterall, the peak structure in the dV_2/dI curves still suggests a reduced local field in the antiparallel configuration as pointed out above. While not completely clear evidence, it is suggestive and further experimental confirmation of this behavior would necessitate a better understanding of the local field profile either through a novel device design or a much weaker ferromagnet. We do know that some magnetic field must be present at the interface in zero applied field since the antisymmetric component exists there as well.

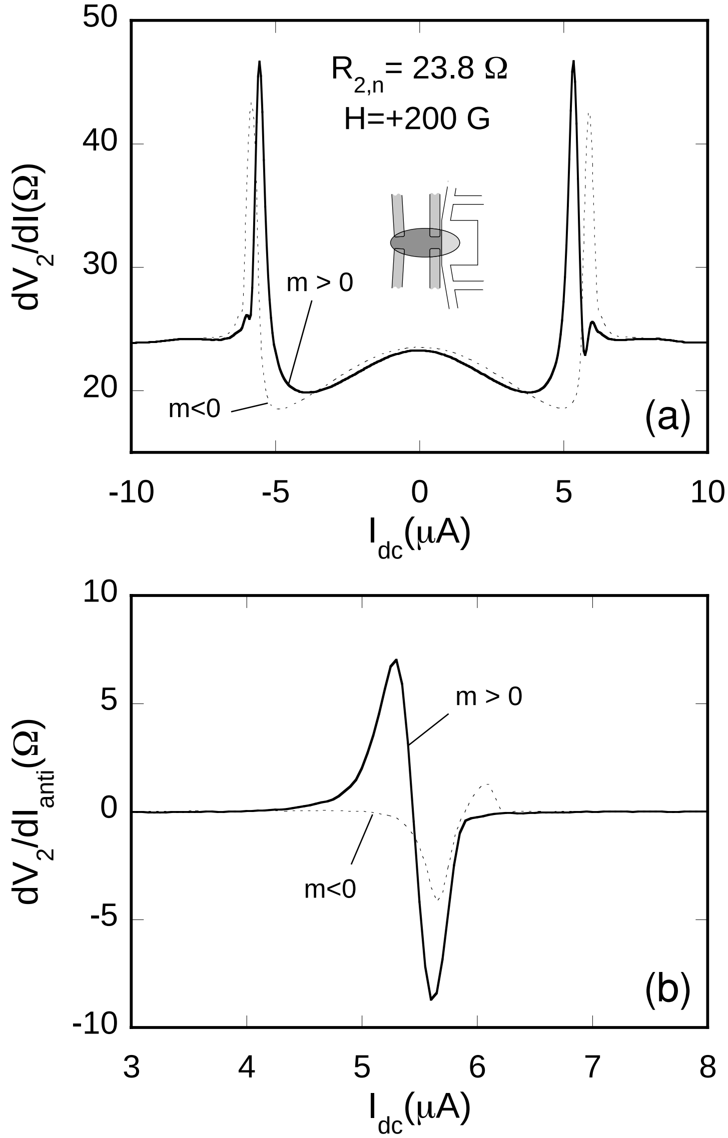

Figure 6.10: dV_2/dI antisymmetry switching with respect to relative magnetization and magnetic field direction at $T = 0.3$ K and $H = +200$ G. (a) dV_2/dI for m and H parallel (solid trace) and antiparallel (dashed trace). (b) Corresponding antisymmetric components for the traces in (a). (inset) Schematic shows device geometry.

6.5 The differential conductance dI/dV_2

As tentative as the evidence presented above may be, a more rigorous confirmation of spin-polarized transport may be performed in our highest resistance sample ($R_{2,n}$ = 1.24 MΩ). Although the resistance would indicate that this should be in the tunnel junction regime, both the temperature dependence (Fig. 6.6(d)) and the differential conductance dI/dV_2 indicate that it is not. Figure 6.11(a) shows such a measurement, performed in an applied field of 1 kG.

Upon first observation, it appears that there may be a small offset in the bias voltage, with the minimum of the central dip positioned slightly lower than zero. After a thorough search for any systematic errors in the bias voltage readout circuit, we determined that this shift in the minimum is real. This is more apparent if one performs a simulation under similar parameters as shown in Fig. 6.11(filled circles). [The numerical simulation shown is generated from our modified BTK model assuming the following parameters: P = 0.28, Z = 2.07, H = 5 kG, H_c = 20 kG (note that we have taken the magnetic field to be larger than the applied magnetic field).] While the experimental and simulated data are quite similar, with the exception of peak height, their antisymmetric components are almost identical. This calculated antisymmetry is a direct result of spin-polarized transport as outlined previously in Chapter 3, and is qualitatively similar in shape and magnitude to the results of our numerical calculations for FS tunnel junctions (see, for instance, Figs. 3.7 and 3.8). As for the shift in the central minimum, this can now be understood as a direct result of the weighted spin subchannel transmission into the quasiparticle density of states in the superconductor, which subsequently gets "smeared" unevenly into the center at finite temperatures.

In light of the above considerations, we conclude that this high resistance data, in combination with our numerical simulations, provides the first explicit strong evidence for spin injection into a superconductor in mesoscopic heterostructure device.

6.6 dV_2/dI vs. magnetic field

In addition to antisymmetry studies of the differential resistance dV_2/dI we also investigated the magnetic field dependence. Figure 6.12 shows some low-field normalized traces for our $R_{2,n}$ =23.8 Ω and $R_{2,n}$ =44.0 Ω samples. Although the conventional method of displaying this data is to offset the curves in the dV_2/dI axis, it is helpful to map the data in a 2D plot due to the number of fields mea-

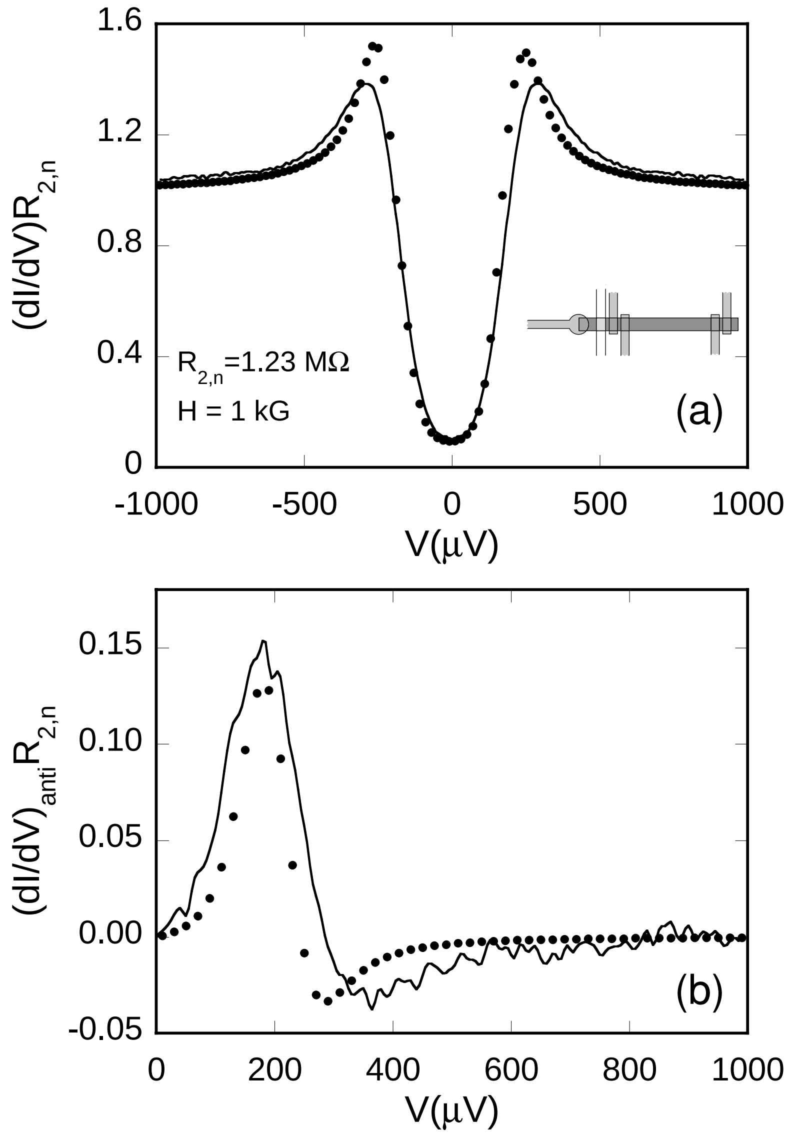

Figure 6.11: High FS interface differential conductance measurement, dI/dV_2. (a) Original dI/dV_2 trace (solid trace) at $T = 0.3$ K in an applied field of 1 kG (along the wire axis). The filled circles represent a BTK numerical calculation assuming $P = 0.28$, $Z = 2.07$, $H = 5$ kG, $H_c = 20$ kG. (b) Antisymmetric components of the traces in (a). (inset) Schematic shows device geometry.

sured. This alternative representation is shown in Figure 6.13 and gives us a little more insight into the phase diagram of these two systems.

In Fig. 6.13(a) we notice that peaks in the differential resistance draw steadily inward as the magnetic field increases, in a $(1-(H/H_c)^2)^{\frac{1}{2}}$ behavior characteristic of the parallel field dependence of the superconducting gap [111, 112]. The phase diagram of Fig. 6.13(b) shows a similar behavior beyond 2000 G, yet below this threshold there is a considerable deviation as the gap appears to close at smaller fields. This behavior was also seen in the Petrashov FS experiment [6] and it was believed to be a consequence of the magnetic field distribution near the interface. In that geometry, the field was applied out-of-plane, tipping the magnetization away from its in-plane easy axis resulting in deviations in the phase diagram at low-fields where the magnetization was not saturated. In our case, however, the magnetization of the ellipse is in a partially relaxed single domain state (as evidenced by AMR measurements similar to Fig. 6.7(b)), and there are no drastic changes to this state as the field is increased. However, a clue to this behavior may lie in the device geometry itself. The device measured in Figs. 6.12(b) and 6.13(b) is slightly different in that the Al wire overlaps the end of the Ni particle without covering the end entirely (geometry "B" in Fig.6.2), at the point where most of the magnetic flux should exit the sample. In this sense, the magnetic profile may be very different than the original geometry ("A" in Fig. 6.2) in that it may couple the exiting flux as it winds back to the other end of the particle, counter to the direction of the particle magnetization. This would offset the effective field in the superconductor (near the interface) negatively with respect to the magnetization. This offset would then appear as an offset phase boundary as the applied field is increased in the direction of the magnetization, in this case corresponding to -2000 G. While this explanation is still speculative at the moment, we believe that these phase diagrams underscore the effect of the ferromagnetic particle's contribution to FS transport through the magnetic field generated by its intrinsic magnetization distribution. Consequently, phase diagram measurements such as this will be useful in future experiments in determining the homogeneity and level of magnetic field penetration at the FS interface.

6.7 Summary

Although the initial question of a ferromagnetic proximity effect was the initial motivation for this series of experiments, it was also the simplest to answer. As we have shown in our devices, FS interface resistances can masquerade as a proximity

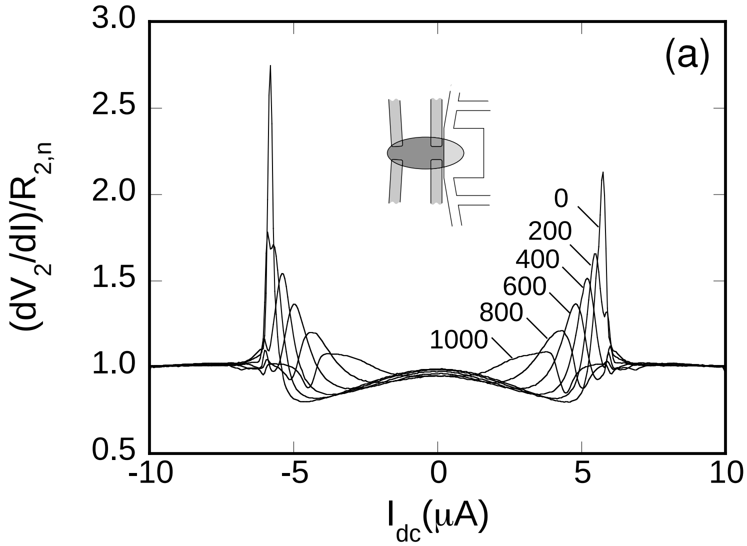

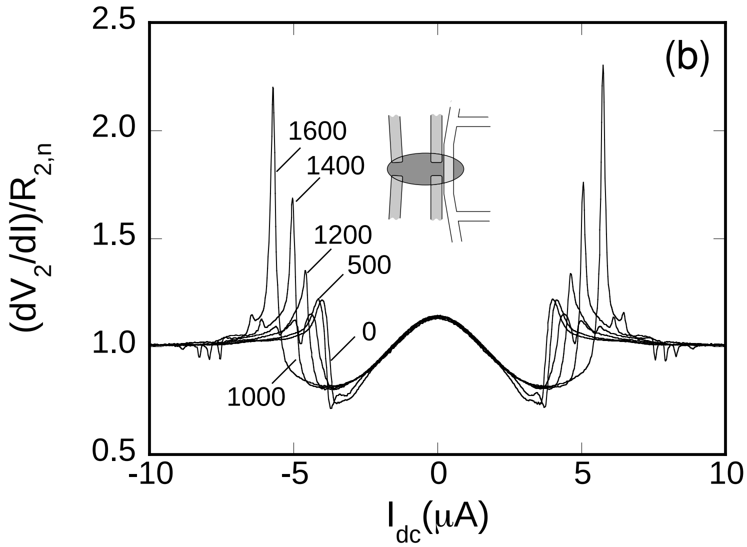

Figure 6.12: dV_2/dI as a function of magnetic field at T =0.3 K. (a) dV_2/dI for $R_{2,n}$ =23.8 Ω in H =0–1000 G. (b) dV_2/dI for $R_{2,n}$ =44.0 Ω in H =0–1600 G. (insets) Schematics show device geometry.

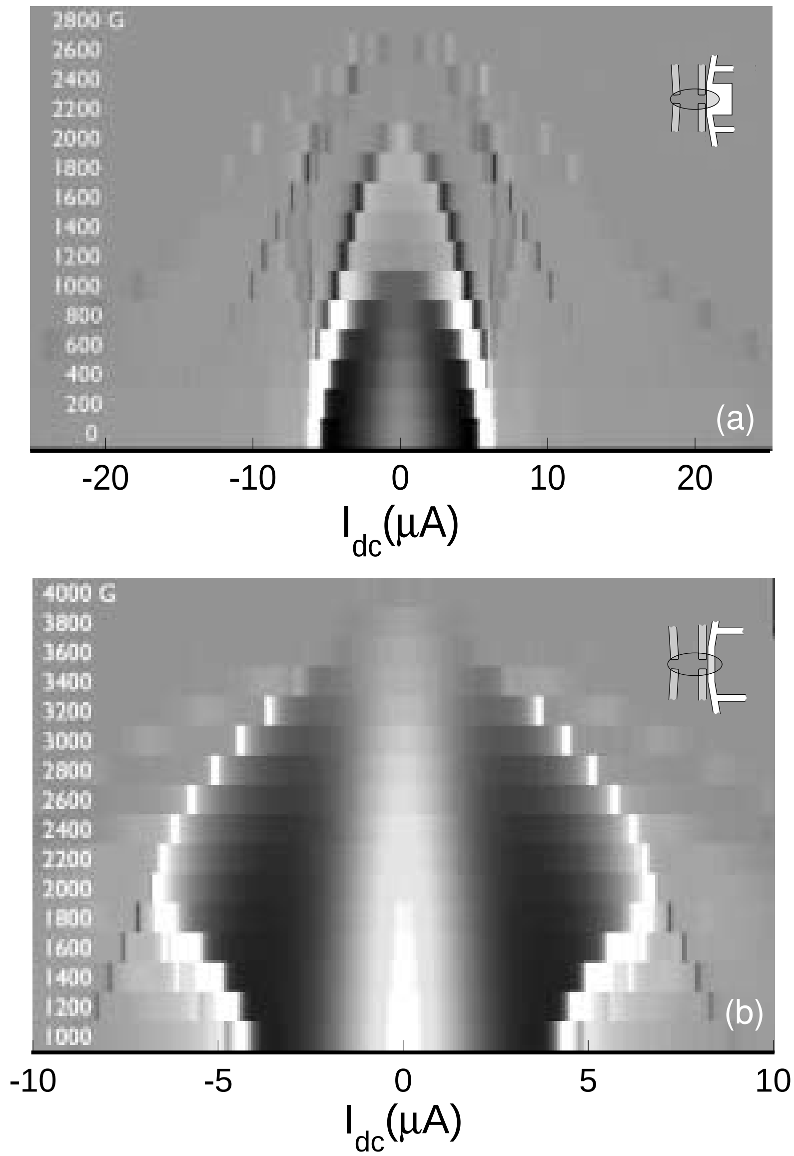

Figure 6.13: 2D plot of dV_2/dI vs. I and H. Alternative phase plot of the differential conductance vs. magnetic field. (a) dV/dI for $R_{2,n}$ =23.8 Ω in H =0–2800 G. (b)dV/dI for $R_{2,n}$ =44.0 Ω in H =1000–4000 G. Brightness indicates magnitude of dV/dI. (insets) Schematics show device geometry.

effect if they are not accounted for with a suitable probe geometry. Meanwhile, the remaining measurements presented in this chapter have illustrated the possibility of spin-polarized transport into a superconductor with the specific hallmark being an antisymmetric component. Although early FS tunneling measurements [78] had to utilize very high fields to distinguish the splitting in the quasiparticle density of states, our antisymmetrization methods give at least a qualitative indication that a spin-polarized current is being transported in much smaller fields where the Zeeman splitting is also relatively small. However, in such low-field measurements, the local magnetic field distribution can play an integral role in determining FS barrier resistance and, consequently, experimentalists and theorists alike should exercise caution in dismissing such an effect in an analysis or calculation.

Chapter 7

SUMMARY AND CONCLUSIONS

As a topic of study, ferromagnetic metals seem, in many ways a last frontier for mesoscopic metallic device physics, with many of the classic quantum transport effects already established in nonmagnetic systems. There are, of course, exceptions to this rule as the Coulomb blockade effect and mesoscopic NS heterostructures are fairly recent additions to this roster. However, since the birth of the modern era of mesoscopics, there has been surprisingly little done in the area of mesoscopic magnetic devices. It is difficult to say for certain why this has been so, but part of the reason may lie in the historical significance magnetic impurities have played in reducing the phase coherence length. In a more practical sense, however, mesoscale magnetic devices have been avoided because of the nontrivial domain structure which can exist even in submicron magnetic elements. In this sense, it is hoped that what is outlined in this thesis can serve as a partial roadmap of hazards to avoid and methods for identifying these hazards unambiguously in a language relevant to the mesoscopic physicist. It is in this spirit that we summarize the contributions of this thesis to the future study of mesoscale ferromagnetic transport.

7.1 *Submicron ferromagnetic transport, quantum and otherwise*

In Chapters 2 and 5, we outlined the general methods for interpreting the magnetotransport of submicron single-domain ferromagnets. It was found that the magnetization could be correlated to the magnetoresistive response through the anisotropic magnetoresistance (AMR) effect [19] and that this effect could, in turn, be easily differentiated from quantum interference effects such as weak localization and conductance fluctuations. Furthermore, it has been demonstrated that magnetotransport could be utilized as a robust tool for studying micromagnetic elements over a wide temperature range, exploiting the ubiquity of AMR rather than deriding it as a nuisance.

Additionally, a solid understanding of the AMR contribution (as well as its counterpart, the Lorentz magnetoresistance) is useful in assessing the conclusions of a number of domain wall experiments [25–28, 55–59], one of which [58] we analyze in Appendix A. Similarly, theorists have postulated possible contributions to the intrinsic domain wall resistivity through weak localization-type corrections at low temperatures [97, 113] and it will be incredibly important to understand the less exotic contributions to the magnetoresistance prior to making a quantitative analysis of such a mechanism.

Other future prospects for ferromagnetic device studies include the possibility of an unambiguous determination of the phase coherence length in a ferromagnetic metal (which is still a bit of a Holy Grail to some experimentalists) following the precautions outlined in Chapter 2. This may be done either through a weak localization type of measurement or through an autocorrelation analysis of the conductance fluctuation data. However, on a more practical level, it is hoped that submicron single domain elements will be incorporated into more complicated heterostructures as they can provide convenient sources for spin-injection and detection in micron scale "spintronic" circuits.

7.2 Ferromagnetic/Superconductor transport

In Chapter 2 we discussed possible ways of understanding the temperature and energy bias dependence between ferromagnets and superconductors with arbitrarily strong interface barriers using a modified Blonder-Tinkham-Klapwijk [69] description of electronic transport. In doing so, we demonstrated that spin-polarized transport into quasiparticle states in the superconductor should naturally manifest itself in an antisymmetric component in the differential conductance or resistance. Furthermore, it was shown that this component could be distinguished in relatively modest fields where the Zeeman splitting is less than the thermal energy k_BT, whereas earlier FS tunneling experiments relied on Tesla scale fields [78]. This antisymmetrization procedure can already be applied to zero applied field measurements in FS point contacts [83–85] to detect possible field penetration into the superconductor. In addition, it should be feasible to perform low-field point contact measurements as another eperimental probe of the polarization, rather than measuring the zero-field conductance alone as is done currently.

In Chapter 6, we demonstrated the lack of an appreciable proximity effect in our Al/Ni devices. Instead, we showed that the strong temperature dependences seen in previous work [6] could be accounted for in our samples as contributions due solely to the FS interface resistance. To verify this picture, we engaged in a series of temperature and bias dependence measurements in FS devices with various barrier resistances, ultimately showing that the spin-polarization of the ferromagnetic charge carriers may play an important role in interpreting FS transport phenomena. Additionally, it was found that magnetic flux generated by the ferromagnetic elements could penetrate the superconductor with dramatic results in the FS transport. Although this is seldom discussed in theoretical treatments of the FS problem, our experiments show that it can be difficult to dismiss this contribution outright and should always be considered in an FS experimental analysis.

Currently, the possibilities for these devices are too numerous to list here. However, as this thesis has treated both quantum interference and FS transport, it is interesting to ask whether the two could not be coupled in a manner similar to the NS case, where the macroscopic phase of a superconductor can be coupled to the phase of normal state electrons. Even if the phase coherence length is of the order of one hundred nanometers, it should still be possible to lithographically define a hybrid FS interferometer such as a superconducting ring bridged by a very short ferromagnet. In principle, it would then be possible to study phase decoherence effects (such as those postulated in domain walls [113]) using the amplitude of the interference as a gauge. This relies only on a coupling between the superconducting and normal electron phases and not on any extensive proximity effect. Such an experiment would also demonstrate electronic phase coherence in the ferromagnet on some finite mesoscopic length scale. In any case, it clear that hybrid FS structures offer a number of experimental opportunities that can exploited for purposes of enhancing our knowledge of ferromagnetic quantum transport as well as spin-polarized quasiparticle transport in superconductors.

BIBLIOGRAPHY

[1] C. W. J. Beenakker and H. van Houten, in *Quantum Transport in Semiconductor Nanostructures*, Vol. 44 of *Solid State Physics*, edited by H. Ehrenreich and D. Turnbull (Academic Press, San Diego, 1991).

[2] S. Washburn and R. A. Webb, Adv. Phys **35**, 375 (1986).

[3] P. A. Lee and T. V. Ramakrishnan, Rev. Mod. Phys. **57**, 287 (1985).

[4] P. A. Lee and A. D. Stone, Phys. Rev. Lett. **55**, 1622 (1985).

[5] V. T. Petrashov, V. N. Antonov, S. V. Maksimov, and R. S. Shaĭkhaĭdarov, JETP Lett. **59**, 552 (1994).

[6] V. Petrashov *et al.*, Phys. Rev. Lett. **83**, 3281 (1999).

[7] V. Petrashov *et al.*, J. Low Temp. Phys. **118**, 689 (1999).

[8] M. D. Lawrence and N. Giordano, J.Phys.:Condens. Matter **8**, L563 (1996).

[9] M. Giroud *et al.*, Phys. Rev. B **58**, R11872 (1998).

[10] V. I. Fal'ko, A. F. Volkov, and C. Lambert, Phys. Rev. B **60**, 15394 (1999).

[11] W. Belzig *et al.*, cond-mat/0005188. *to be published in Phys. Rev. B. (2000).*

[12] R. Mélin, Europhys. Lett. **51**, 202 (2000).

[13] A. A. Golubov, Physica C **327**, 46 (1999).

[14] W. Belzig, *private communication.*

[15] S. Washburn, IBM J. Res. Develop. **32**, 335 (1988).

[16] B. L. Altshuler and A. G. Aronov, in *Electron-Electron Interaction in Disordered Systems, edited by A. L. Efros and M. Pollak* (Elsevier Science Publishers B. V., Amsterdam, 1985).

[17] N. W. Ashcroft and N. D. Mermin, *Solid State Physics* (Saunders College Publishing, Orlando, FL, 1976).

[18] I. A. Campbell and A. Fert, in *Transport Properties of Ferromagnets*, Vol. 3 of *Ferromagnetic Materials*, edited by E. P. Wohlfarth (North-Holland Publishing, Amsterdam, 1982).

[19] T. R. McGuire and R. I. Potter, IEEE Trans. Mag. **MAG-11**, 1018 (1975).

[20] W. Thomson, Proc. Roy. Soc. **8**, 546 (1857).

[21] J. Smit, Physica **XVI**, 612 (1951).

[22] R. R. Birss, *Symmetry and magnetism* (North-Holland, Amsterdam, 1964).

[23] C. M. Hurd, Adv. Phys. **23**, 315 (1974).

[24] A. Aharoni, *Introduction to the Theory of Ferromagnetism* (Oxford University Press, New York, 1996).

[25] U. Ruediger *et al.*, Phys. Rev. Lett. **80**, 5639 (1998).

[26] U. Rüdiger, J. Yu, A. D. Kent, and S. S. P. Parkin, Appl. Phys. Lett. **73**, 1298 (1998).

[27] J. Yu *et al.*, Phys. Rev. B **60**, 7352 (1999).

[28] U. Rüdiger *et al.*, Phys. Rev. B **59**, 11914 (1999).

[29] N. F. Mott and H. H. Wills, Proc. Roy. Soc. **A 156**, 368 (1936).

[30] K. Fuchs, Proc. Cambridge Philos. Soc. **34**, 100 (1938).

[31] E. H. Sondheimer, Adv. Phys. **1**, 1 (1952).

[32] T. G. S. M. Rijks, R. Coehoorn, M. J. M. de Jong, and W. J. M. de Jonge, Phys. Rev. B **51**, 283 (1995).

[33] T. G. S. M. Rijks, S. K. J. Lenczowski, R. Coehoorn, and W. J. M. de Jonge, Phys. Rev. B **56**, 362 (1997).

[34] J. M. Ziman, *Electrons and Phonons* (Oxford University Press, Oxford, 1960).

[35] J. Aumentado and V. Chandrasekhar, Physica B **284**, 1742 (2000).

[36] J. Rammer, *Quantum Transport Theory* (Perseus Books, Reading, 1998).

[37] P. Mohanty, private communication.

[38] V. Chandrasekhar, Ph.D. thesis, Yale University, 1989.

[39] P. W. Anderson, E. Abrahams, and T. V. Ramakrishnan, Phys. Rev. Lett. **43**, 718 (1979).

[40] L. P. Gorkov, A. I. Larkin, and D. E. Khmel'nitskii, JETP Lett. **30**, 228 (1979).

[41] A. A. Abrikosov, L. P. Gorkov, and I. E. Dzyaloshinski, *Methods of Quantum Field Theory in Statistical Physics* (Dover, New York, 1975).

[42] G. Bergmann, Phys. Rep. **107**, 1 (1984).

[43] S. Chakravarty and A. Schmid, Phys. Rep. **140**, 193 (1986).

[44] K. Hong and N. Giordano, J. Magn. Magn. Mater. **151**, 396 (1995).

[45] M. Aprili, J. Lesueur, L. Dumoulin, and P. Nédellec, Solid State Commun. **102**, 41 (1997).

[46] S. Kobayashi, Y. Ootuka, F. Komori, and W. Sasaki, J. Phys. Soc. Jpn. **51**, 689 (1982).

[47] A. O. Adeyeye *et al.*, J. Appl. Phys. **79**, 6120 (1996).

[48] A. O. Adeyeye *et al.*, Appl. Phys. Lett. **70**, 1046 (1997).

[49] C. Shearwood *et al.*, J. Appl. Phys. **75**, 5249 (1994).

[50] J. E. Wegrowe *et al.*, Phys. Rev. Lett. **82**, 3681 (1999).

[51] Y. Jaccard *et al.*, Phys. Rev. B **62**, 1141 (2000).

[52] A. D. Benoit *et al.*, Phys. Rev. Lett. **57**, 1765 (1986).

[53] V. Chandrasekhar, P. Santhanam, and D. E. Prober, Phys. Rev. B **44**, 11203 (1991).

[54] M. Büttiker, Phys. Rev. Lett. **57**, 1761 (1986).

[55] J. F. Gregg *et al.*, Phys. Rev. Lett. **77**, 1580 (1996).

[56] M. Viret *et al.*, Phys. Rev. B **53**, 8464 (1996).

[57] K. Hong and N. Giordano, J. Phys.: Condens. Matter **10**, L401 (1998).

[58] T. Taniyama, I. Nakatani, T. Namikawa, and Y. Yamazaki, Phys. Rev. Lett. **82**, 2780 (1999).

[59] U. Ebels *et al.*, Phys. Rev. Lett. **84**, 983 (2000).

[60] V. L. Ginzburg and L. D. Landau, JETP **20**, 1064 (1950).

[61] P. G. de Gennes, *Superconductivity of Metals and Alloys* (W. A. Benjamin, New York, 1966).

[62] A. F. Andreev, Sov. Phys. JETP **19**, 1228 (1964).

[63] P. Charlat *et al.*, Phys. Rev. Lett. **77**, 4950 (1996).

[64] H. Courtois, P. Gandit, D. Mailly, and G. Pannetier, Phys. Rev. lett. **76**, 130 (1996).

[65] P. G. N. de Vegvar, Phys. Rev. Lett. **73**, 73 (1994).

[66] H. Pothier, S. Gueron, D. Esteve, and M. H. Devoret, Phys. Rev. Lett. **73**, 2488 (1994).

[67] V. T. Petrashov, V. N. Antonov, P. Delsing, and T. Claeson, Phys. Rev. Lett. **74**, 5268 (1995).

[68] E. A. Demler, G. B. Arnold, and M. R. Beasley, Phys. Rev. B **55**, 15174 (1997).

[69] G. E. Blonder, M. Tinkham, and T. M. Klapwijk, Phys. Rev. B **25**, 4515 (1982).

[70] M. Tinkham, *Introduction to Superconductivity, 2d ed.* (McGraw-Hill, New York, 1996).

[71] I. Giaver, Phys. Rev. Lett. **5**, 147 (1960).

[72] T. M. Klapwijk, G. E. Blonder, and M. Tinkham, Physica B **109 & 110**, 1657 (1982).

[73] T. M. Klapwijk, Physica B **197**, 481 (1994).

[74] C. Nguyen, H. Kroemer, and E. L. Hu, Phys. Rev. Lett. **69**, 2847 (1992).

[75] P. Xiong and G. Xiao, Phys. Rev. Lett. **69**, 1907 (1993).

[76] P. M. Tedrow and R. Meservey, Phys. Rev. Lett. **26**, 192 (1971).

[77] P. M. Tedrow and R. Meservey, Phys. Rev. B **7**, 318 (1973).

[78] R. Meservey and P. M. Tedrow, Phys. Rep. **238**, 173 (1994).

[79] R. Meservey, P. M. Tedrow, and P. Fulde, Phys. Rev. Lett. **25**, 1270 (1970).

[80] J. Eom, C. J. Chien, and V. Chandrasekhar, Phys. Rev. Lett. **81**, 437 (1998).

[81] J. Eom, Ph.D. thesis, Nortwestern University, 1998.

[82] M. J. M. de Jong and C. W. J. Beenakker, Phys. Rev. Lett. **74**, 1657 (1995).

[83] R. J. Soulen, Jr. *et al.*, Science **282**, 85 (1998).

[84] R. J. Soulen, Jr. *et al.*, J. Appl. Phys. **85**, 4589 (1999).

[85] S. K. Upadhyay, A. Palanisami, R. N. Louie, and R. A. Buhrman, Phys. Rev. Lett. **81**, 3247 (1998).

[86] C. J. Chien, Ph.D. thesis, Northwestern University, 1998.

[87] M. J. Rooks, Ph.D. thesis, Yale University, 1987.

[88] W. M. Moreau, *Semiconductor Lithography: Principles, Practices, and Materials* (Plenum Press, New York, 1988).

[89] F. Pobell, *Matter and methods at low temperatures* (Springer-Verlag, Berlin, 1996).

[90] J. G. Adler and J. E. Jackson, Rev. Sci. Instrum. **37**, 1049 (1966).

[91] J. Aumentado *et al.*, Appl. Phys. Lett. **75**, 3554 (1999).

[92] C. Fierz *et al.*, J. Phys.: Condens. Matter **2**, 9701 (1990).

[93] N. F. Mott and H. Jones, *The Theory of the Properties of Metals and Alloys* (Dover, New York, 1936).

[94] P. Santhanam and D. E. Prober, Phys. Rev. B **29**, 3733 (1984).

[95] K. Hong and N. Giordano, Phys. Rev. B **51**, 9855 (1995).

[96] P. M. Levy and S. Zhang, Phys. Rev. Lett. **79**, 5110 (1997).

[97] G. Tatara and H. Fukuyama, Phys. Rev. Lett. **78**, 3773 (1997).

[98] Y. Q. Jia, S. Y. Chou, and J.-G. Zhu, J. Appl. Phys. **81**, 5461 (1997).

[99] W. Wernsdorfer *et al.*, J. Magn. Magn. Mater. **145**, 133 (1995).

[100] L. Berger and G. Bergmann, in *The Hall Effect and Its Applications*, edited by C. L. Chien and C. R. Westgate (Plenum Publishing, New York, 1980).

[101] Y. Lyanda-Geller, private communication.

[102] R. Seviour, C. J. Lambert, and A. F. Volkov, Phys. Rev. B **59**, 6031 (1999).

[103] F. Zhou and B. Spivak, cond-mat/9906177.

[104] D. Craik, *Magnetism* (John Wiley & Sons, New York, 1995).

[105] K. Kawaguchi and M. Sohma, Phys. Rev. B **46**, 14722 (1992).

[106] J. S. Jiang, D. Davidović, D. H. Reich, and C. L. Chien, Phys. Rev. Lett. **74**, 314 (1995).

[107] C. J. Chien and V. Chandrasekhar, Phys. Rev. B **60**, 3655 (1999).

[108] G. J. Dolan and L. D. Jackel, Phys. Rev. Lett. **39**, 1628 (1977).

[109] W. Belzig *et al.*, Superlattic Microst. **25**, 1251 (1999).

[110] J. Eom *et al.*, Phys. Rev. Lett. **77**, 2276 (1996).

[111] D. E. Morris and M. Tinkham, Phys. Rev. Lett. **6**, 600 (1961).

[112] D. H. Douglass, Jr., Phys. Rev. Lett. **7**, 14 (1961).

[113] Y. Lyanda-Geller, I. L. Aleiner, and P. M. Goldbart, Phys. Rev. Lett. **81**, 3215 (1998).

[114] R. P. van Gorkom, A. Brataas, and G. E. W. Bauer, Phys. Rev. Lett. **83**, 4401 (1999).

[115] A. Brataas, G. Tatara, and G. E. W. Bauer, Phys. Rev. B **60**, 3406 (1999).

Appendix A

DOMAIN WALL RESISTIVITY EXPERIMENTS AND ANISOTROPIC MAGNETORESISTANCE

Although we do not specifically address the issue of DW resistivity experimentally in this work, it is a worthwhile momentary digression due to great theoretical [96, 97, 113–115] and experimental [25–28, 55–59] interest in recent years. The experimental challenge in measuring the resistivity of a DW is chiefly in characterizing the AMR contribution due to the nonuniform magnetization distribution in the wall. For this reason, it is preferable to fabricate wires or films with dimensions comparable to the bulk domain size in an effort to reduce or simplify the magnetization distribution. However, in such small samples, minor deviations in the magnetization may have a much greater effect through the AMR than in larger devices and it is a nontrivial task to isolate the contribution due solely to the DW resistivity. Here we will concentrate on the experiment of Taniyama *et al.* [58] as representative of the subtle problems that arise in attempting to subtract out the AMR contribution from the intrinsic DW contribution in mesoscale devices.

In the Taniyama experiment, the resistance of a thirty segment Co zig-zag wire was measured as a function of field. This novel zig-zag geometry allowed the preparation of an aligned monodomain remanent state (Fig. A.1 (a)) as well as an anti-aligned multidomain remanent state (Fig. A.1 (b)) by saturating the magnetic field longitudinally or perpendicularly to the general axis of the wire. Due to the strong shape anisotropy, the domains preferred to align along the zig-zag arms, and it was assumed by the authors that the current distribution is completely collinear with the arms, only sampling the longitudinal resistivity $\rho_{\parallel}$. In this way, it was believed that the resistance in the multidomain state was entirely due to the intrinsic DW resistivity.

It should be immediately obvious (by Maxwell's equations and by symmetry) that equipotentials should bisect the corners and the current should cross these equipotentials at normal incidence, *i.e.*, the current cannot be completely collinear with the arms at the corners. This is not too much of a problem since the magnetization must also "turn" with a finite radius at the corners as well and this probably does not provide much of a correction to the total resistance (Fig. A.1(c)). How-

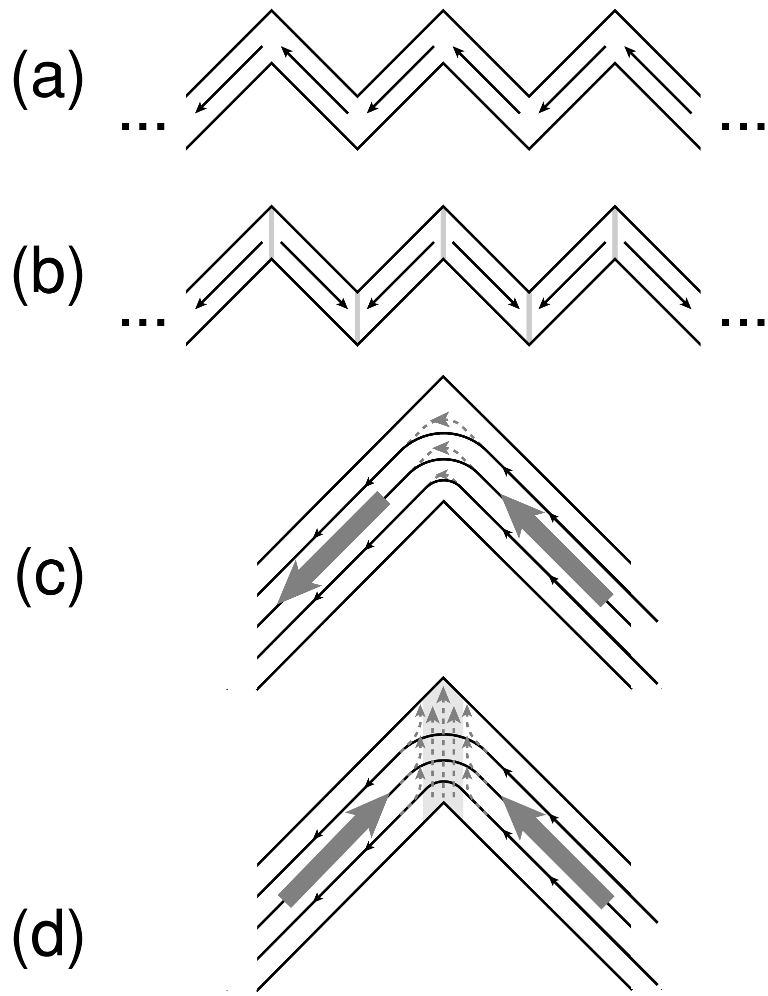

Figure A.1: Zig-zag geometry from Taniyama *et al.* [58] for measuring the DW resistivity. (a) monodomain state, (b) multidomain state with DWs localized at the corners, (c) enlarged view of monodomain magnetization (grey arrows) and the general alignment with the current paths (solid arrows), (d) enlarged view of the multidomain state with DWs (light grey).

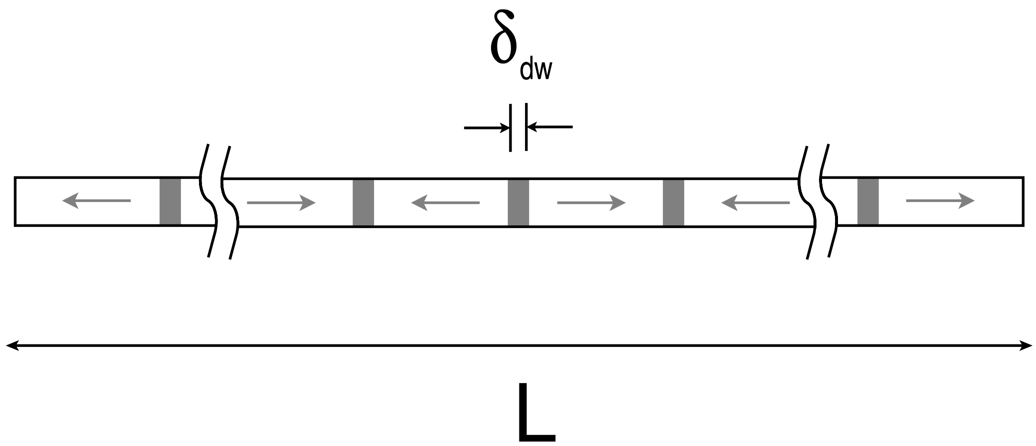

Figure A.2: Approximation of the zig-zag in Fig. A.1 as a straight wire with perpendicular DWs of width δ_{dw}

ever, this assumption is not true for the multidomain state (Fig. A.1(d)) where the DWs are comprised of magnetic moments pointing towards the corners at a 45° angle to the arms, or ∼90° to the current paths. If we take the radius of curvature of the current paths at the corners to be larger than the DW width δ_{dw} then we can simplify the multidomain picture and "stretch out" the zig-zag into a straight wire with N_{dw} DWs and further assume that the majority of the magnetization lies along the axis, with the domain wall magnetizations lying perpendicular to the wire axis[1] (see Figure A.2).

At this point we can ask what is measured by the total resistance of such a wire if we have N_{dw} DWs of width δ_{dw} *and* include the intrinsic DW resistivity ρ_{dw} along with the AMR. The total resistance is then

$$R_{tot,w/walls} = \frac{\rho_{\|}(L - N_{dw}\delta_{dw})}{A} + \frac{(\rho_{\perp} + \rho_{dw})N_{dw}\delta_{dw}}{A}, \tag{A.1}$$

where A is the cross-sectional area. The first r.h.s. term is the resistance of the

[1]This is the assumption made in drawing Fig. A.1, however, even if the current path radius of curvature is much smaller than δ_{dw}, then the angle between the current and the magnetization at the corners is 45° rather than 90°, and this straight wire approximation will still have some validity if the DW magnetization is adjusted accordingly.

arms where the magnetization is parallel to the current path, while the second term is DW resistance assuming that the magnetization is perpendicular to the current path there. The resistance difference between the multidomain and the monodomain state should then yield the resistivity contribution from the DWs with the following relation,

$$\begin{aligned} \Delta R_{tot} &= R_{tot,w/walls} - R_{tot,w/o\ walls} \\ &= (\rho_{dw} - \Delta\rho_{AMR})\frac{N_{dw}\delta_{dw}}{A}. \end{aligned} \tag{A.2}$$

Since Taniyama *et al.* prefer to deal with the change in the average resistivity[2] we also write the equivalent equation,

$$\Delta\overline{\rho}_{tot} = (\rho_{dw} - \Delta\rho_{AMR})\frac{N_{dw}\delta_{dw}}{L}. \tag{A.3}$$

From the form of Eqn. A.3 it is easy to see that the change in resistance contains contributions from both ρ_{dw} and $\Delta\rho_{AMR}$. However, this form is specific to our starting assumptions, namely, that the current distribution deviates from the magnetization direction in the DWs. Taniyama *et al.* assume that the zig-zag geometry eliminates this (without any magnetic imaging to confirm this). According to that assumption, the resistivity factor in the second term of Eqn. A.1 would be $\rho_\parallel + \rho_{dw}$ which would alter the change in the average resistivity to read

$$\Delta\overline{\rho}_{tot} = \rho_{dw}\frac{N_{dw}\delta_{dw}}{L}. \tag{A.4}$$

In their actual experiment Taniyama *et al.* found $\Delta\overline{\rho}_{tot} \sim -0.01$ $\mu\Omega$·cm. With twenty-nine DWs, an assumed $\delta_{dw} \sim 0.015$ μm[3] and a total length of 61.5 μm this gives a DW contribution $\rho_{dw} \sim -1.4$ $\mu\Omega$·cm by Eqn. A.4.[4] If we revert to the other

[2] In principle the average resistivity and the resistance are interchangeable, although in this thesis the use of the resistivity implies a spatial dependence, $\rho(\boldsymbol{x})$— an intrinsic anisotropic quantity that varies with the local magnetization direction. This is not the case in the Taniyama experiment [58] where $\rho = AR_{tot}/L$, which is really only the spatial average over the length L.

[3] This width is taken from room temperature magnetoforce microscope measurements of a Co thin film of similar thickness [55]. Micromagnetic shape anisotropies may alter this width considerably [24] and it is far more preferable to have a direct measurement of this quantity in the actual zig-zag wire.

[4] Alert readers may notice that $\rho_{dw} \sim -1.4$ $\mu\Omega$·cm is actually estimated at -1.8 $\mu\Omega$·cm in Ref. [58], which is probably due to errors in estimating $\Delta\overline{\rho}_{tot}$ from the figures in that work.

extreme and assume that ρ_{dw} is neglible, then by Eqn. A.3, the entire change in resistance is due to AMR. This would yield a $\delta_{dw} \sim 0.099$ μm. Since there was no direct confirmation of δ_{dw} in their wires, such a wide width cannot be dismissed outright. In either case, assumptions about the magnetization distribution or the DW resistivity are made which are difficult to assert without more experimental evidence.

In general, this lack of knowledge about the true nature of the magnetization distribution $\boldsymbol{M}(\boldsymbol{x})$ and/or the current path $\boldsymbol{j}(\boldsymbol{x})$ is what makes most of the recent experiments difficult to interpret. Many of these experiments make strong assumptions about $\boldsymbol{M}(\boldsymbol{x})$ which can be of questionable validity, especially in mesoscale devices where the shape anisotropy plays a much bigger role in the magnetization as a whole. The problem is compounded by the fact that common methods of characterizing micromagnetic distributions (*e.g.*, magnetoforce microscopy (MFM) and Lorentz microscopy) can only image a 2D projection with a resolution that is generally insufficient for observing small deviations in the magnetization.

Despite this grim view of the analysis prospects of these experiments, a recent experiment by Ebels *et al.* [59] seems to show concrete evidence for the existence of ρ_{dw}. In that experiment, the magnetization of long, narrow (35 nm) electrodeposited Co wires was aligned preferentially along the wire axis due to shape anisotropy. With a field applied along the wire axis and opposite to the magnetization direction, they nucleated DWs which *raised* the resistance of the wire. Since the DWs must consist of moments aligned perpendicular to the wire axis and the current, there should be a contribution from $\rho_{\perp}$ which lowers the total resistance. This reduction in the resistance was clearly seen in slightly wider (50 nm) wires, yet in the 35 nm wires the change was positive suggesting that $\rho_{\perp} > \Delta\rho_{AMR}$. Although it was impossible to image the wire being measured in that work, the unambiguous positive sign is suggestive of scattering mechanisms beyond AMR and provide a good starting point for future DW investigations.